Understanding the disease mechanisms and developing new therapies for *RDH12*-related retinopathies

Hajrah Sarkar

A thesis submitted to University College London for the degree of Doctor of Philosophy

Institute of Ophthalmology, University College London

Supervisor: Professor Mariya Moosajee

October 2021

Declaration

I, Hajrah Sarkar, confirm that the work presented in this thesis is my own. Where information has been derived from other sources, I confirm that this has been indicated in the thesis.

Abstract

Retinol dehydrogenase 12 (RDH12) is expressed in photoreceptor inner segments and catalyses the reduction of all-trans retinal (atRAL) to all-trans retinol as part of the visual cycle. Mutations in *RDH12* are primarily associated with Leber congenital amaurosis (LCA), a severe early-onset retinal dystrophy causing childhood blindness, and in rare cases autosomal dominant retinitis pigmentosa (RP), causing a late onset milder phenotype. There are currently no treatments for *RDH12*-related retinopathies.

In this thesis, several models were generated to study the disease mechanisms and test new therapeutics. Recombinant expression and purification of RDH12 was attempted to study protein structure, however difficulties in purification were encountered, with protein aggregation and low yields. CRISPR/Cas9 gene editing was used to generate a *rdh12* zebrafish mutant model. *rdh12* fish displayed a late onset rod-predominant degeneration, with defects in rhodopsin trafficking. Early indicators of stress were detected in the adult retina, with reduced expression of autophagy and oxidative stress markers and increased phagosome size. HEK-293 stable cell lines expressing wildtype (WT) and mutant RDH12 were generated. WT RDH12 protected cells from atRAL-induced toxicity. Mutant *RDH12* cells displayed reduced protein expression and activity, with an inability to protect cells from atRAL toxicity, inducing oxidative and endoplasmic reticulum (ER) stress.

Zebrafish and cell line models revealed a number of disrupted pathways, representing potential therapeutic targets. A number of drugs were screened and pregabalin, a retinal scavenger, was found to reduce

atRAL induced ER stress in *RDH12* mutant cells, representing a new class of potential drugs that can be targeted for *RDH12*-retinopathies. Induced pluripotent stem cell lines were generated from two patients, to be used for differentiation to retinal organoids facilitating further investigation of disease mechanisms and drug screening. The models created in this project provide a valuable resource for further study of *RDH12*-retinopathies and development of novel therapeutics.

Impact Statement

Inherited retinal dystrophies (IRD) are a group of clinically and genetically heterogeneous disorders caused by mutations in over 300 genes affecting approximately 1 in 2000 individuals worldwide. Mutations in the retinol dehydrogenase 12 (*RDH12*) gene are primarily associated with autosomal recessive Leber congenital amaurosis, the most severe type of IRD. Patients present with early onset visual loss, leading to complete blindness in adulthood. Autosomal dominant mutations in *RDH12* are associated with late onset mild retinitis pigmentosa. There are currently no treatments for *RDH12*-related retinopathies. *Rdh12* knockout mouse models do not recapitulate the severe phenotype observed in patients, resulting in a limited understanding of the disease mechanisms and development of new therapeutics.

In this thesis, I have generated a number of *RDH12* models that were used to investigate disease mechanisms, identify potential therapeutic targets and test new drugs. I generated HEK-293 stable cell lines expressing wildtype and mutant RDH12, and a *rdh12* mutant zebrafish model, which both revealed several disrupted pathways, representing key targets for therapeutics. These results have recently been published and can be used to make informed decisions on the types of drugs to test, with ER stress lowering drugs, antioxidants and retinal scavengers representing a new class of potential drugs for *RDH12*-retinopathies. The *RDH12* cell lines generated here are an extremely valuable resource for drug screening and can be used by other researchers and pharmaceutical companies for further drug screening.

I also generated two patient derived induced pluripotent stem cell lines, which can be used for differentiation to retinal organoids. Retinal organoids have been shown to recapitulate human development and disease phenotypes, providing a useful model of human disease, derived from a patient's own cells, thereby opening up the avenue for personalised medicine. Differentiation of *RDH12* lines is already underway in our lab. These lines have been published as a lab resource article, and are therefore available to other researchers, further extending the impact of this work.

Finally, as cellular stress and disrupted pathways identified in this project, are common to a number of IRDs, caused by mutations in other visual cycle genes, pathways identified here can inform research on other IRDs, and drugs identified through screening in *RDH12* models may be applicable to other diseases.

Acknowledgements

Firstly, I would like to thank my supervisor Professor Mariya Moosajee for her continuous support and mentorship, for her encouragement and guidance throughout my PhD. I also thank my secondary supervisor Professor Tim Levine for his helpful advice.

I am extremely grateful to my fellow lab members past and present for their support in and out of the lab: Dr Maria Toms for all her guidance and assistance with zebrafish work, Dr Dulce Lima Cunha, Dr Cécile Méjécase and Dr Nick Owen with cell culture work; my fellow PhD students Philippa Harding, Jonathan Eintracht and Lyes Toualbi for their company during all the hours spent in tissue culture and looking after my cells when I was away. I thank all the team for their continuous training, motivation and encouragement.

I gratefully acknowledge Dr Charlotte Dodson for allowing me to come back to her lab for the protein expression and purification work and providing me with excellent training. I acknowledge the support of the Peptide Chemistry and Electron Microscopy facilities at the Francis Crick Institute, in particular Christelle Soudy for her assistance with HPLC experiments, and Marie-Charlotte Domart for electron microscopy work.

And finally, most importantly I would like to thank my parents for their constant love and support throughout my life and many years of study.

Publications

Sarkar H, Toms M, Moosajee M. Involvement of Oxidative and Endoplasmic Reticulum Stress in *RDH12*-Related Retinopathies. (2021). *International Journal of Molecular Sciences*, 22(16), 8863.

Sarkar H, Méjécase C, Harding P, Eintracht J, Toualbi L, Cunha DL, Moosajee M. Generation of two human iPSC lines from patients with autosomal dominant retinitis pigmentosa (UCLi014-A) and autosomal recessive Leber congenital amaurosis (UCLi015-A), associated with RDH12 variants (2021). *Stem Cell Research*, 54, 102449.

Sarkar H, Dubis AM, Downes S, Moosajee M. Novel Heterozygous Deletion in Retinol Dehydrogenase 12 (*RDH12*) Causes Familial Autosomal Dominant Retinitis Pigmentosa. (2020) *Frontiers in Genetics*, 11, 335.

Sarkar H, Moosajee M. Retinol dehydrogenase 12 (RDH12): Role in vision, retinal disease and future perspectives. (2019) *Experimental Eye Research*, 188, 107793.

Méjécase C, Harding P, **Sarkar H**, Eintracht J, Lima Cunha D, Toualbi L, Moosajee M. Generation of two human control iPS cell lines (UCLi016-A and UCLi017-A) from healthy donors with no known ocular conditions. (2020) *Stem Cell Research*, 49, 102113.

Table of Contents

List of figures

List of tables

Abbreviations

µl	microliters
µl	micrometre
4-HNE	4-hydroxynonenal
A2E	N-retinylidene-N-retinylethanolamine
aa	amino acid
ABCA4	ATP-binding cassette, sub family A, member 4
AMD	age related macular degenerations
ARRP	autosomal recessive RP
ATF	activating transcription factor
atRAL	all-trans retinal
atROL	all-trans retinol
BiP	binding immunoglobulin protein
BM	Bruchs membrane
bp	base pair
Cas9	CRISPR associated protein 9
CAT	catalase
CC	connecting cilium
cDNA	complementary DNA
cGMP	cyclic guanosine monophosphate
chm	choroideremia
CHOP	C/EBP homologous protein
CORD	cone-rod dystrophy
CRALBP1	cellular retinaldehyde binding protein
CRBP1	cellular retinol binding protein 1
CRISPR	clustered regularly interspaced short palindromic repeat
crRNA	CRISPR RNA
DAPI	4′,6-diamidino-2-phenylindole
DHPC	1,2-diheptanoyl-sn-glycero-3-phosphocholine
DHT	dihydotestosterone
DMEM	Dulbeccos modified Eagles medium
DMSO	dimethylsuphoxide
DNA	deoxyribonucleic acid
dpf	days most fertilisation
DSB	double stranded break
dsDNA	double stranded DNA
EB	embryoid body
EBNA	Epstein-Barr nuclear antigen-1
ELM	external limiting membrane
EOSRD	early onset severe retinal dystrophy
ER	endoplasmic reticulum
ERG	electroretinogram
ESC	embryonic stem cells
EZ	ellipsoid zone
FAF	fundus autofluorescence
FBS	foetal bovine serum
GCL	ganglion cell layer
GFP	green fluorescent protein

GPX	glutathione peroxidase
GSH	glutathione
HDR	homology directed repair
HEK-293	human embryonic kidney 293
HO-1	heme oxygenase 1
Hpf	hours post fertilisation
HPLC	high performance liquid chromatography
IMAC	immobilised metal affinity chromatography
INL	inner nuclear layer
IPL	inner plexiform layer
iPSC	induced pluripotent stem cells
IPTG	isopropyl β-D-1-thiogalactopyranoside
IRBP	interphotoreceptor binding protein
IRD	inherited retinal dystrophies
IRE1	inositol requiring enzyme 1
IS	inner segment
IZ	interdigitation zone
LAP	LC3-associated phagocytosis
LB	lysogeny Broth
LC3	microtubule-associated protein 1 light chain 3
LCA	Leber congenital amaurosis
LRAT	lecithin retinol acyltransferase
ml	millilitres
mm	millimetre
mpf	months post fertilisation
mRNA	messenger RNA
MTT	3-[4,5-dimethylthiazole-2-yl]-2,5-diphenyltetrazolium bromide
NAC	N-acetylcysteine
NACA	N-acetyl cysteine amide
NAD+/NADH	nicotinamide adenine dinucleotide
NADP+/ NADPH	nicotinamide adenine dinucleotide phosphate
ng	nanograms
NGS	normal goat serum
NHEJ	non-homologous end joining
nm	nanometer
N-ret-PE	N-retinylidene-phosphatidylethanolamine
Nrf2	nuclear factor erythroid 2-relate factor 2
ONL	outer nuclear layer
OPL	outer plexiform layer
ORF	open reading frame
OS	outer segment
PAM	protospacer adjacent motif
PBMC	peripheral blood mononuclear cells
PBS	phosphate buffered saline
PCR	polymerase chain reaction
PDE	phosphodiesterase
PDH	photoreceptor retinol dehydrogenase
PE	phosphatidylethanolamine
PERK	protein kinase R-like ER kinase

PFA	paraformaldehyde
PGB	pregabalin
RDH	retinol dehydrogenase
RLBP1	retinaldehyde binding protein-1
RNA	ribonucleic acid
ROS	reactive oxygen species
RP	retinitis pigmentosa
RPE	retinal pigment epithelium
RPE65	retinoid isomerohydrolase
rpm	revolutions per minute
RT-qPCR	reverse transcription quantitative PCR
SD-OCT	spectral domain optical coherence tomography
SDR	short chain dehydrogenases/reductases
SDS	sodium dodecyl sulphate
SDS-PAGE	SDS-polyacrylamide gel electrophoresis
SEM	standard error of mean
sgRNA	single guide RNA
SOD	superoxide dismutase
TCEP	tris(2-carboxyethyl) phosphine
TEM	transmission electron microscopy
tracrRNA	trans-activating crRNA
TUDCA	tauroursodeoxycholic acid
TUNEL	terminal deoxynucleotidyl transferase dUTP nick end labeling
UPR	unfolded protein response
UV	ultraviolet
V	volts
WT	wildtype
XBP1	X-box binding protein 1

1. Introduction

1.1. The retina

1.1.1. Anatomy of the retina

The retina is the ~200 µm thick multicellular layer at the back of the eye responsible for the conversion of light to electrical signals that are transmitted to the brain via the optic nerve, allowing the processing of an image. The vertebrate retina is highly organised and is composed of 5 types of neuronal cells: photoreceptors, bipolar cells, horizontal cells, amacrine cells and retinal ganglion cells. The retina is organised into five distinct layers of two types: the nuclear layers, containing the cell bodies, and the plexiform layers, composed of synaptic connections. The photoreceptor cell bodies form the outer nuclear layer (ONL). Photoreceptors synapse on to the bipolar and horizontal cells in the outer plexiform layer (OPL). The inner nuclear layer (INL) contains the cell bodies of the bipolar and amacrine cells, which synapse onto retinal ganglion cells in the inner plexiform layer (IPL). Finally, the ganglion cell layer (GCL) is composed of the retinal ganglion cell bodies. In addition Müller glia cells span the entire retina, providing molecular support (Hoon et al., 2014) (**Figure 1**).

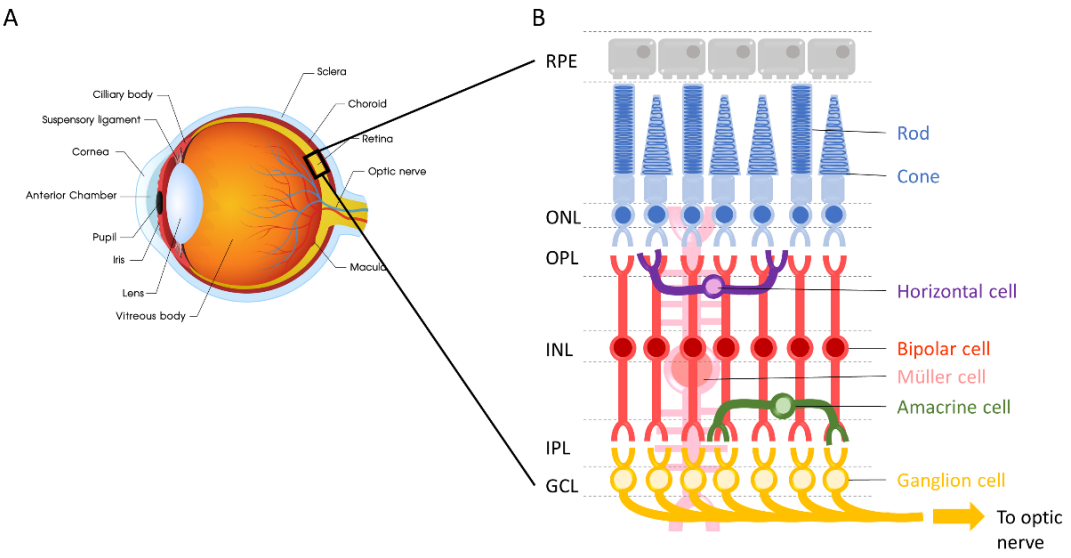

Figure 1: Anatomy of the retina
(A) Structure of the eye. **(B)** The retina is a multicellular tissue organised into distinct layers. RPE; retinal pigment epithelium, ONL; outer nuclear layer, OPL; outer plexiform layer, INL; inner nuclear layer, IPL; inner plexiform layer, GCL; ganglion cell layer.

1.1.2. The photoreceptors

There are two types of photoreceptors: rods and cones, which differ in shape, visual pigment, and spatial distribution in the retina. The rods are extremely sensitive to light and are responsible for dim light vision. Conversely, cones are responsible for high visual acuity, colour vision, and function under normal and bright light conditions. In humans, there are three types of cone photoreceptors, with sensitivities to short (S, blue), medium (M, green) or long (L, red) wavelengths of light. The rods far outnumber the cones, with approximately 120 million rods present in the human retina, compared to 6 million cones, which are highly concentrated at the fovea, facilitating high acuity vision. Photoreceptors are composed of an outer segment (OS), inner segment (IS), connecting cilium (CC), cell body and synaptic terminal (**Figure 2**). Rods have a long OS, composed of stacks of

flattened membrane discs of equal diameter, enclosed by the plasma membrane. Whereas the discs of cone OSs are formed from invaginations of the plasma membrane, creating a continuous stack of open discs of increasing diameter, forming the characteristic conical shape. The IS contains the housekeeping machinery of the cell and is where essential functions like protein synthesis take place. It contains the endoplasmic reticulum (ER), Golgi complex, mitochondria and other organelles. The CC connects the inner and outer segments and facilitates transport of proteins from the IS to the OS. The cell body is continuous with the IS and is the region where the nucleus is located. The synaptic terminal contains synaptic vesicles and synapse ribbons, which synapse onto bipolar and horizontal cells (Molday and Moritz, 2015, Baker and Kerov, 2013).

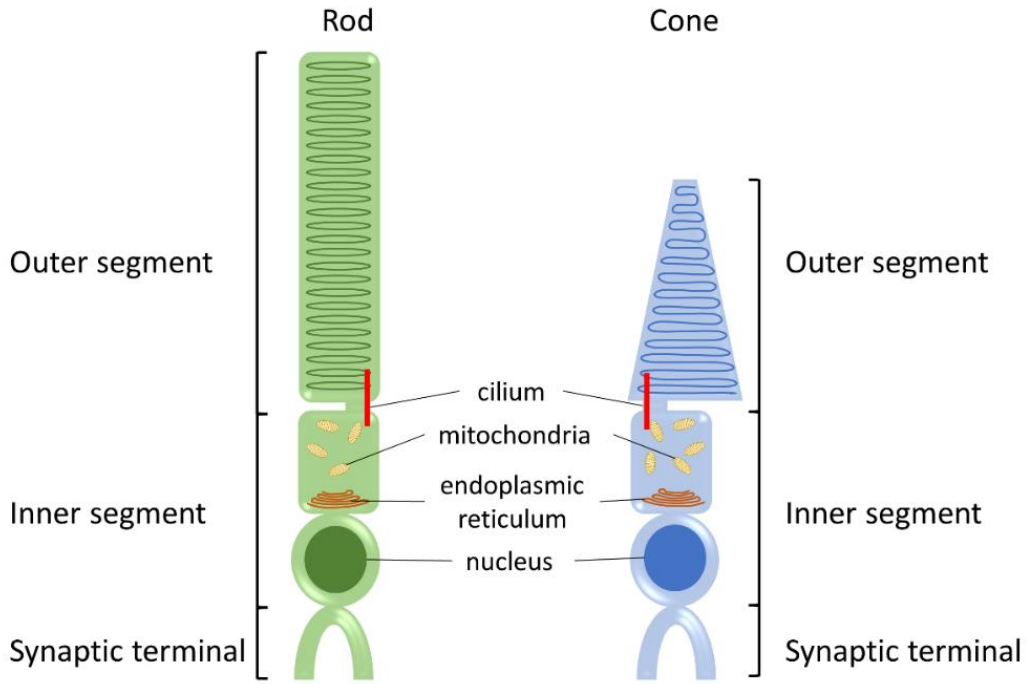

Figure 2: Structure of the photoreceptors.
The photoreceptors are composed of an outer segment, inner segment, connecting cilium, cell body and synaptic terminal. The rods have a long outer segment, whereas the cone outer segment is shorter and a characteristic conical shape.

The first step in vision is phototransduction, the capture of a photon of light and its conversion to a chemical signal in the photoreceptor OS. Light is absorbed by the visual pigments, formed by rhodopsin and opsins, of the rods and cones, respectively, covalently linked to the chromophore 11-cis retinal. Upon absorption of a photon of light, 11-cis retinal is photo-isomerised to all-trans retinal (atRAL) which is released from the opsin. This triggers a phototransduction cascade, beginning with the activation of G-protein transducin, which in turn activates phosphodiesterase (PDE). PDE hydrolyses cyclic guanosine monophosphate (cGMP), reducing its concentration in the cell, resulting in the closure of ion channels in the outer segment membranes, and hyperpolarisation of the cell. This results in reduced secretion of neurotransmitter at the photoreceptor synapses (Prasad and Galetta, 2011).

1.1.3. The retinal pigment epithelium

The retinal pigment epithelium (RPE) is a monolayer of pigmented cells directly adjacent to the photoreceptors on its apical side, and Bruch's membrane on its basolateral side. It carries out many functions, providing metabolic support to the photoreceptors, and protecting the retina from photo-oxidative damage. In order to protect the retina from light damage, pigments responsible for the absorption of light are present in the RPE, with melanin in melanosomes responsible for general light absorption. Specialised visual pigments responsible for absorbing different wavelengths of light are also present in the RPE and photoreceptors. The retina is also exposed to high levels of oxidative stress; to combat this, the RPE contains

antioxidants, including enzymatic antioxidants like superoxide dismutase (SOD) and catalase (CAT), and nonenzymatic antioxidants like carotenoids, ascorbate, α-tocopherol, β-carotene and melanin, which itself is an antioxidant. In addition, the RPE also has the ability to repair damaged DNA, protein and lipids. The RPE is also an essential part of the blood-retina barrier, transporting ions, water and metabolites from the subretinal space to the blood, and transporting glucose, retinol and fatty acids from the blood to the photoreceptors. The RPE also secretes growth factors that support the function of the photoreceptors. Finally, the RPE plays an extremely important role in the regeneration of the visual chromophore, 11-cis retinal, through a series of reactions known as the visual cycle (Strauss, 2005).

1.1.4. The visual cycle

For photoreceptors to function under constant light, following phototransduction (Section 1.1.2), atRAL must be converted back to 11-cis retinal. Photoreceptors are unable to isomerise atRAL to 11-cis retinal, therefore this is achieved via the RPE, in a series of reactions collectively termed the visual cycle. atRAL is first reduced to all-trans retinol (atROL) in the OS by retinol dehydrogenase 8 (RDH8). atROL is then transported to the RPE bound to interphotoreceptor binding protein (IRBP). In the RPE, atRAL is converted to its retinyl ester by lecithin retinol acyltransferase (LRAT), then isomerised to 11-cis retinol by retinoid isomerohydrolase (RPE65), and finally oxidised back to 11-cis retinal by RDH5. 11-cis retinal is transported back to the photoreceptors bound to IRBP, where it combines with opsin again and is ready to be activated by a photon (Sahu and Maeda, 2016) (**Figure 3**). A

second cone specific visual cycle also exists, where atRAL is reduced to atROL. atROL is transported to the Müller cells, where it is isomerised to 11-cis retinol, this is then transported to the cone photoreceptors, where it is oxidised back to 11-cis retinal (Wang and Kefalov, 2011). However, this pathway has not been studied extensively and little is known about the proteins involved.

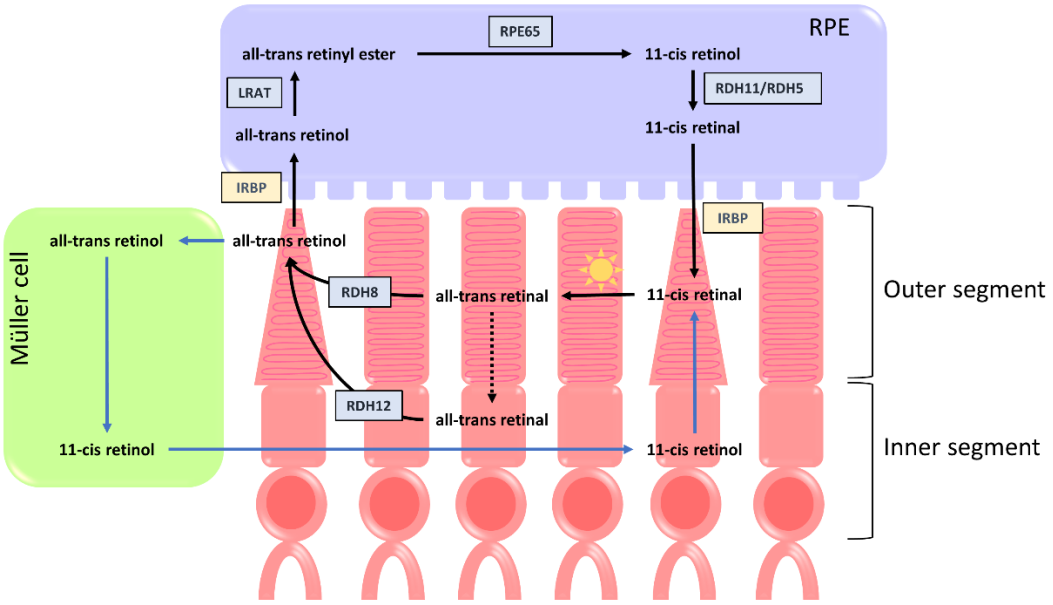

Figure 3: Regeneration of the visual chromophore via the visual cycle. 11-cis retinal is regenerated via a series of reactions in the photoreceptors and RPE, known as the canonical visual cycle, indicated by the black arrows. A second cone specific visual cycle takes place via the Müller cells and is shown with the blue arrows. RPE; Retinal pigment epithelium, IPBP; Interphotoreceptor binding protein, LRAT; Lecithin retinol acyltransferase, RPE65; Retinoid isomerohydrolase, RDH; Retinol dehydrogenase

Not all the atRAL released from the opsins is reduced to its alcohol. A proportion of the atRAL reacts with phosphatidylethanolamine (PE) in disc membranes to generate N-retinylidene-phosphatidylethanolamine (N-ret-PE), which can become trapped on the luminal side of the disc membranes. ATP-binding cassette transporter (ABCA4) transports N-ret-PE from the luminal to

the cytoplasmic side where it can be reduced to atROL and re-enter the visual cycle. atRAL can also diffuse to the inner segments, where it is reduced to atROL by retinol dehydrogenase 12 (RDH12). If excess atRAL is not cleared from cells, it can lead to the irreversible formation of toxic bisretinoid condensation products, such as N-retinylidene-N-retinylethanolamine (A2E) and atRAL-dimer, which are photosensitive and cause oxidative damage to protein and lipids (Sparrow et al., 2012, Molday and Moritz, 2015).

1.1.5. RPE phagocytosis

Photoreceptors are susceptible to high levels of oxidative stress and photodamage, as a result of exposure to high light intensities and the presence of high concentrations of polyunsaturated fatty acids. To combat this, the oxidised membranes of the OSs are shed and phagocytosed by RPE cells daily, with an OS being fully replaced every 10-14 days. In order to maintain a constant length of the OS, new OS is formed from the base of the OS at the same rate that the OS is shed from the tip. RPE cells recognise, bind and engulf shed OS. Once engulfed into the RPE, the phagosome undergoes a number of fusions ultimately resulting in the degradation of its protein and lipid contents. With each step increased levels of reactive oxygen species (ROS) are produced, further contributing to high levels of oxidative stress in the RPE (Kevany and Palczewski, 2010, Sparrow et al., 2010).

atRAL and bisretinoids transferred to the RPE through phagocytosis accumulate with age as lipofuscin in the lysosomal compartment of the cells.

These bisretionoids act as photosensitisers, causing damage to proteins and lipids. The pigments in lipofuscin is the source of fundus autofluorescence (FAF) and can be imaged on confocal scanning laser ophthalmoscopy. The accumulation of lipofuscin is characteristic of normal RPE, however excess accumulation is a feature of some retinal disorders, with regions of intense autofluorescence observed in some patients, and the absence of FAF indicating RPE atrophy or cell death (Sparrow et al., 2010, Sparrow et al., 2012).

1.2. Inherited retinal dystrophies

Inherited retinal dystrophies (IRD) are a group of clinically and genetically heterogeneous disorders caused by mutations in over 300 genes (RetNet, https://sph.uth.edu/RetNet/), affecting approximately 1 in 2000 individuals worldwide (Cremers et al., 2018). They can be categorised into subgroups based on a number of factors including age of onset, disease progression and retinal cell types primarily affected. There is considerable genetic heterogeneity in IRDs, with mutations in a number of different genes causing the same clinical phenotype, but also phenotypic heterogeneity, with variants in the same gene responsible for different disease phenotypes (Cremers et al., 2018).

Mode of inheritance can be autosomal dominant, autosomal recessive or X-linked and in rare cases mitochondrial. Autosomal diseases are caused by variants in genes that are not on a sex chromosome and both males and females have an equal chance of being affected. Autosomal recessive

diseases are caused by homozygous variants, with one copy inherited from each parent, who are carriers with heterozygous variants. Children of carriers have a 25% chance of disease, and there is greater risk in consanguineous families (Gulani and Weiler, 2021). In autosomal dominant diseases, only one pathogenic allele is required to cause disease. Offspring from one affected heterozygous and one unaffected parent have a 50% chance of inheriting disease (Lewis and Simpson, 2021). In a recent study that looked at data from over 3000 IRD patients in the United Kingdom, 52.6% of families had variants in genes that displayed autosomal recessive inheritance; 8.2% of families showed variants in genes that act dominantly; 24.5% of families had variants in genes that have both dominant and recessively acting variants (Pontikos et al., 2020).

The most common IRD is retinitis pigmentosa (RP), affecting approximately 1 in 3500-4000 individuals worldwide. RP can be transmitted through different modes of inheritance, with autosomal dominant inheritance accounting for 30-40% of cases and generally a less severe phenotype. Autosomal recessive inheritance accounts for 50-60% of cases and X-linked inheritance for 5-15% of cases. RP can either be syndromic, for example Usher syndrome, which is associated with congenital sensorineural hearing loss, and Bardet-Beidl, which is associated with obesity, postaxial polydactyly, hypogonadism, renal dysfunction, and learning disabilities, or non-syndromic, which is more common with mutations in more than 80 genes implicated. RP is described as a rod-cone dystrophy, beginning with rod cell degeneration, followed by cone cell death. Although clinical

progression and age of onset varies widely, patients typically present with night blindness initially, followed by progressive loss of peripheral visual field, and finally as central cone cells die, a rapid decline in visual acuity. Clinically, three features are seen as signs of RP, bone spicule pigmentation, waxy pallor of the optic nerve and attenuation of retinal vessels (Verbakel et al., 2018).

The most severe IRD is Leber congenital amaurosis (LCA), which has considerable clinical and genetic overlap with RP and accounts for approximately 5% of IRD cases. LCA is distinguished from RP by age of onset, with symptoms present at birth or developed within the first few months of life. LCA is a group of severe autosomal recessive, early-onset rod-cone dystrophies, associated with mutations in 25 genes. The genes implicated in LCA are expressed in the retina or RPE and encode proteins with a range of functions involved in vision, including phototransduction, the visual cycle and photoreceptor ciliary transport. The most commonly mutated genes are *GUCY2D*, *CEP290*, *CRB1*, *RDH12* and *RPE65*. LCA is associated with severe visual loss early in life, together with nystagmus, poor pupillary response, eye poking and an undetectable electroretinogram (ERG) (Kumaran et al., 2017).

Other types of IRD include macular dystrophies, cone/cone-rod dystrophies and congenital stationary night blindness. In addition to inherited conditions, aging and environmental factors can also be implicated in vision loss, for example in age related macular degeneration (AMD).

The progress in genome sequencing techniques over the past decade has led to improved diagnosis and the identification of numerous genes responsible for IRDs. However, there are currently no treatments for IRDs, with the exception of *RPE65* gene therapy. The eye provides many advantages as a target organ for therapeutics, as it is easily accessible, the blood-retinal barrier provides immune privilege, preventing systemic administration. The small size of the eye enables lower amounts of therapeutics to be administered and treatment effectiveness can be monitored non-invasively with the non-treated eye serving as the perfect control (Ziccardi et al., 2019).

1.2.1. *RDH12*-retinopathies

RDH12 is located on chromosome 14q24.1, has 7 coding exons and encodes a 316 amino acid protein, with an estimated molecular weight of 35 kDa. It is expressed in the inner segments of the photoreceptors (Belyaeva et al., 2005) and according to the human protein atlas database, is also expressed in the skin, kidney and liver.

Mutations in *RDH12* are primarily associated with LCA, and account for approximately 10% of all LCA cases (Kumaran et al., 2017). Patients with autosomal recessive *RDH12* retinopathy usually present in infancy with early onset visual loss. This is a progressive disease characterised by variable pigmentary retinopathy with peripapillary sparing, RPE atrophy and pronounced central macular changes including pigmentary maculopathy, yellow macular deposits and macular excavation, leading to severe visual

impairment and blindness in adulthood (**Figure 4**) (Aleman et al., 2018, Li et al., 2017, Mackay et al., 2011, Valverde et al., 2009, Zou et al., 2018, Garg et al., 2017).

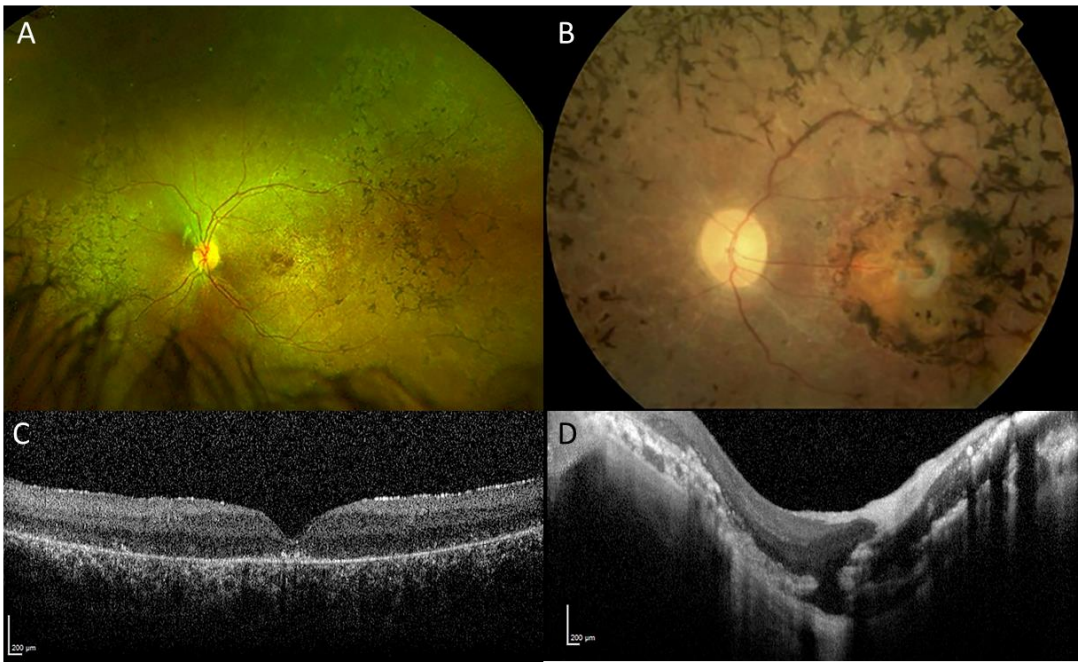

Figure 4: Clinical phenotype of autosomal recessive *RDH12* LCA. **(A)** Optos colour image of left fundus from a 4-year-old girl with compound heterozygous missense mutations showing mid-peripheral bone spicules and macular atrophy with corresponding SD-OCT **(B)** confirming loss of the outer nuclear layer (ONL), ellipsoid zone and RPE. **(C)** Left fundus photo from a 43-year-old lady with a homozygous missense mutation showing macular atrophy, extensive bone spicules and a waxy disc with retinal vessel attenuation; corresponding SD-OCT **(D)** displayed a posterior staphyloma and extensive macular atrophy and structural disorganisation.

Aleman et al. (2018) studied 21 paediatric patients from 14 families (age range 2-17 years), most children presented within the first 2 years of life with early onset visual loss of variable levels and displaying inter-ocular asymmetry. Baseline full-field ERGs were undetectable or severely reduced and fundus examination revealed waxy optic disc pallor, vascular attenuation and mid-peripheral pigmentary changes in all patients with variable

distribution from localised paravascular to bone spicule macula pigmentation. The macula was affected in all patients ranging from central depigmentation, a denser yellow hue at the foveal centre, parafoveal bullseye area of depigmentation to macular atrophy with pigmentation, and in some cases a pseudo-colobomatous configuration. Corresponding FAF revealed central hypoautofluorescence, surrounded by hyperautofluorescent lesions which co-localised with bone spicules and hyperpigmentation. There was preservation of the FAF signal in the peripapillary region as per previous observations. Spectral domain optical coherence tomography (SD-OCT) shows abnormal macular structure with an almost undetectable ONL within a thinned foveal centre. This ONL has a normal appearance in the peripapillary retina. The ellipsoid zone (EZ), interdigitation zone (IZ), and external limiting membrane (ELM) bands are not clearly visible for most of the scans. Using multimodal imaging, visual psychophysics, and dark-adapted chromatic pupillometry, severe central cone and rod dysfunction correlated with the central structural abnormalities with milder extra-macular rod dysfunction (Aleman et al., 2018).

In a recent retrospective chart review of 57 patients by Fahim and colleagues, the average age of onset was 4 years old. Atrophic changes at the macular was a universal finding from as early as age 2, and electrophysiology was markedly reduced in both scotopic and photopic responses. SD-OCT revealed severe structural disorganisation largely after 10 years of age, and 18 patients had peripapillary sparing (Fahim et al., 2019).

Autosomal recessive biallelic mutations in the *RDH12* gene were first identified in three consanguineous Austrian families, with 15 members affected with severe retinal dystrophy (Janecke et al., 2004). A genealogical link was not found between the families, but due to the geographical proximity of the families, it is thought that they were related. The homozygous missense c.677G>A; p.Y226C variant was found in all affected individuals. This variant was also found in two non-related Austrian individuals. In COS-7 cells transfected with a vector encoding the *RDH12* p.Y226C variant, no enzyme activity was found in the forward or reverse reaction, suggesting a loss of function. A number of *RDH12* autosomal recessive mutations linked to LCA have since been identified (Perrault et al., 2004, Thompson et al., 2005, Sun et al., 2007, Benayoun et al., 2009, Mackay et al., 2011, Avila-Fernandez et al., 2010, Sodi et al., 2010, Coppieters et al., 2014). According to the Human Gene Mutation Database (HGMD), 99 *RDH12* mutations have been reported, 61 of which are missense and 13 are nonsense mutations (HGMD public database accessed April 2021). As shown in **Figure 5**, mutations span the entire gene, including the conserved regions, with no specific hotspots.

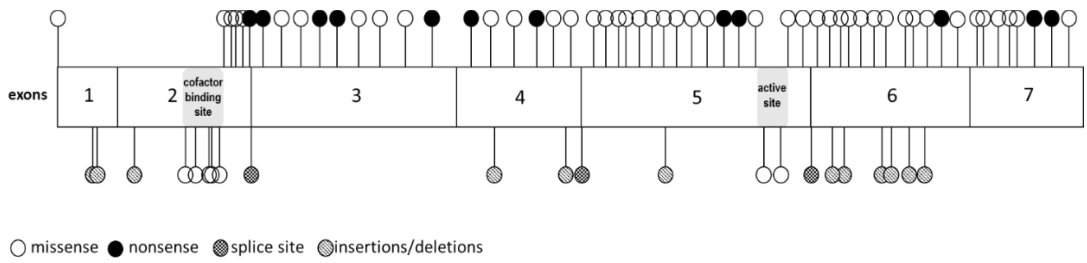

Figure 5: Reported mutations for RDH12
Data from Human Gene Mutation database (http://www.hgmd.cf.ac.uk/ac/gene.php?gene=RDH12 accessed April 2019)

A recent cross-sectional report of 38 patients from 38 unrelated families of Chinese descent, age range 3-53 years (median 20 years), with molecularly confirmed homozygous or compound heterozygous *RDH12* mutations had varying diagnoses of LCA, early onset severe retinal dystrophy (EOSRD), autosomal recessive RP, or cone-rod dystrophy (CORD) (Zou et al., 2018). The most common variant was p.V146D, followed by p.R62* and p.T49M, accounting for 50% of the cases. Visual acuity varied considerably ranging from no light perception to 6/12 (median was 6/60), but once adjusted for age, there was no difference in best corrected visual acuity between patients with EOSRD, autosomal recessive RP, and CORD, although LCA patients had significantly worse vision. Over 55% of patients reported nyctalopia. Variable pigmentation was noted ranging from no pigment with minimal scattered bone spicules to confluent pigment proliferation. They characterised the phenotype into 4 types: (1) Macular coloboma (mostly petal-like) with dense bone spicule pigmentation in the mid-peripheral retina (48.7%); (2) Macular discoloration and widespread bone spicule and/or salt–pepper pigmentation (27.6%); (3) Heavy and confluent pigment proliferation in the mid-peripheral region involving the macular region (18.4%); and (4) Retinal posterior pole atrophy with a relatively normal peripheral retina (2 patients). Overall, the clinical phenotypes were variable, and as yet the determinant factors are not fully understood.

One six-generation family with 19 affected members was found to have autosomal dominant *RDH12* retinopathy caused by a heterozygous single base pair deletion c.776delG; p.Glu260Argfs*18 resulting in a frameshift and

premature termination at codon 277, in 19 affected members of a large 6 generation family (Fingert et al., 2008). Interestingly, compared to the autosomal recessive LCA patients, these patients displayed a late onset (average age at diagnosis was 28.5 years) RP phenotype, with intraretinal bone spicule pigmentation and arteriolar attenuation. Some affected individuals maintained good central visual acuity (6/7.5) until their eighth decade of life. No further cases have been published in the literature.

1.3. Retinol dehydrogenase 12

1.3.1. RDH12 structure

Retinol dehydrogenases (RDHs) are members of the short chain dehydrogenases/reductases (SDR) family of enzymes. The SDRs are typically 250-350 amino acids in length and have a relatively low sequence similarity of about 15-30%. However, common to all SDRs is the highly conserved Rossman fold, which is composed of a central β-sheet flanked by 3-4 α-helices, forming the cofactor binding site. The SDRs have two conserved domains: the cofactor binding site (GXXXGXG) and the catalytic site (YXXXK) (Liden et al., 2003). A number of RDHs are involved in the visual cycle and vary in substrate and coenzyme specificity. RDH8 and retSDR1 are found in the photoreceptor outer segments; RDH12 and RDH11 are found in the inner segments. RDH5, RDH11 and RDH10 are expressed in the RPE (Parker and Crouch, 2010). RDH12 is most closely related to RDH11, sharing 79% sequence similarity (Haeseleer et al., 2002). In RDH12, the cofactor binding site is located at positions 46-52 and the catalytic site at positions 200-204. Due to the difficulty in expression and purification of RDHs, the crystal

structure of RDH12, or that of any other vertebrate RDH, has not yet been solved. A homology model of RDH12, built using the Phyre2 software, which models the protein based on homologs with known structure, is shown in **Figure 6** (Kelley et al., 2015). Hoffman et al., (2016) reported the crystal structure of *Drosophila melanogaster* photoreceptor retinol dehydrogenase (PDH), an orthologue of RDH12, and found it in a dimeric state, thought to be the native conformation, as monomeric PDH in solution was not active (Hofmann et al., 2016). Based on the homology of RDH12 to PDH, it is possible that RDH12 may also function as a dimer.

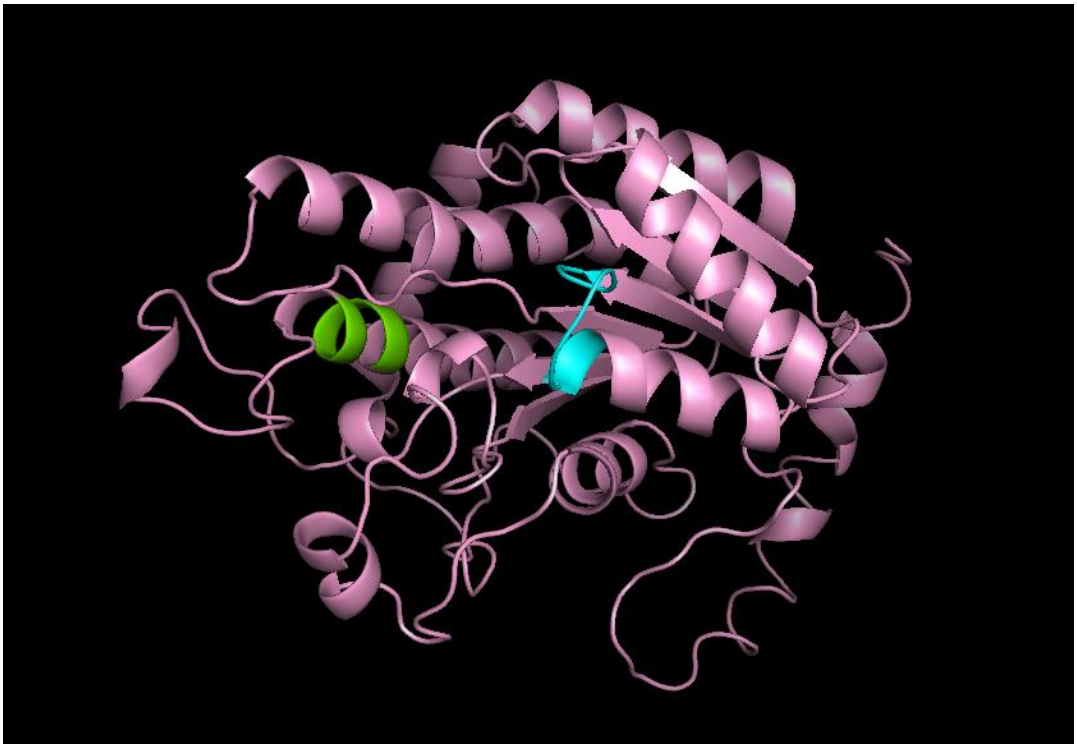

Figure 6: Homology model of RDH12
Model created using Phyre 2 software (Kelley et al., 2015). Active site shown in green, and the cofactor binding site is shown in blue.

1.3.2. Function of RDH12

Purified RDH12 displays a ~2000-fold higher affinity for NADP+ and NADPH than for NAD+ and NADH, and has a greater affinity for retinaldehydes than retinols. RDH12 functions as a retinal reductase, with highest activity towards atRAL, followed by 11-cis retinal (**Figure 7**). However, it is unlikely that 11-cis retinal is metabolised by RDH12 *in vivo*, as according to the visual cycle, 11-cis retinal that enters the photoreceptors is likely to be sequestered by opsins. Binding of CRBP1 to atROL prevents its oxidation by RDH12 (Belyaeva et al., 2005).

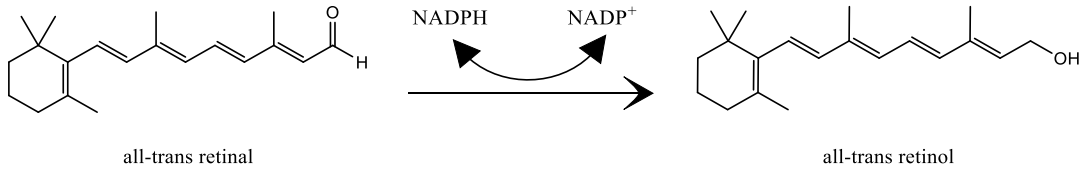

Figure 7: RDH12 catalyses the reduction of all-trans retinal to all-trans retinol.

Studies on the *Rdh8*$^{-/-}$ *Rdh12*$^{-/-}$ double knockout mice, showed that Rdh8 and Rdh12 are responsible for >98% of all-trans RDH activity, with Rdh8 accounting for 70% of atRAL clearance. The majority of atRAL is reduced by Rdh8 in the outer segments, but some atRAL can leak into the inner segments, where it is reduced by Rdh12 (Chen et al., 2012a). These studies suggest that the role of RDH12 in the visual cycle is minimal, but possibly plays a protective role in the clearance of atRAL in periods of intense illumination.

RDH12 can also act on medium chain aldehydes, produced from the oxidative attack of polyunsaturated fatty acids in lipid membranes (Belyaeva et al.,

2005). RDH12 was shown to metabolise the lipid derived medium chain aldehyde nonanal and inhibit the reduction of atRAL in *RDH12* transfected human embryonic kidney 293 (HEK-293) cells, indicating that RDH12 can protect cells from nonanal induced toxicity (Lee et al., 2008). The most abundant lipid peroxidation product is 4-hydroxynonenal (4-HNE). In the study by Lee et al. (2008), RDH12 did not protect cells against 4-HNE. However, Marchette et al. (2010) showed that HEK-293 cells stably transfected with RDH12 did protect from 4-HNE induced cell death, and a greater amount of 4-HNE protein adducts accumulated in *Rdh12*$^{-/-}$ mice retinae following exposure to intense light.

A build-up of either atRAL or lipid peroxidation products is damaging to photoreceptors. atRAL accumulation leads to the production of toxic A2E, and lipid peroxidation products are inherently toxic. RDH12 therefore protects the retina from these toxic compounds.

RDH12 was also shown to convert dihydrotestosterone (DHT) to androstanediol, suggesting a possible involvement in steroid metabolism (Keller and Adamski, 2007). DHT has been implicated in the pathogenesis of androgenic alopecia (male pattern baldness) (Marchetti and Barth, 2013). However, no reports of this phenotype have been described in *RDH12* patients.

1.4. Model systems

1.4.1. Animal models

Many genes are highly conserved across species, making animal models a valuable resource for the study of genetic diseases and testing of therapeutics. The most commonly used animal models are fruit flies, zebrafish, mice and rats. The mouse model is the most widely used animal model and provides many advantages for biomedical research, including a well characterised genome. They are small, easy and cheap to maintain, reproduce and mature quickly and are relatively easy to manipulate genetically.

1.4.1.1. *Rdh12* mouse models

The first *RDH12* animal model reported was the *Rdh12*$^{-/-}$ mouse model, a full Rdh12 knockout, which was generated by replacement of exons 1-3 of the *Rdh12* gene with a neomycin cassette (Maeda et al., 2006). *Rdh12*$^{-/-}$ mice displayed normal retinal morphology at 6 weeks of age. There was no significant difference in rhodopsin levels, indicating efficient regeneration of the chromophore. No difference in all-trans RDH activity in dissected retinae or isolated rod OSs between wildtype and *Rdh12*$^{-/-}$ mice was observed, suggesting that other enzymes may be compensating for the loss of Rdh12 activity. Knockout mice did however show a delayed dark adaptation and accumulation of atRAL after bleaching, indicating an important role of RDH12 under conditions of excess illumination (Maeda et al., 2006). The second *Rdh12*$^{-/-}$ mouse model was reported by Kurth et al., (2007), also a full knockout, was created by targeted deletion of exons 1-3. *Rdh12*$^{-/-}$ mice were

largely comparable to wildtype mice, with normal retinal histology until 10 months, and similar retinoid levels, with no signs of apparent retinal degeneration (Kurth et al., 2007). However, retinal homogenates did show decreased atRAL reduction, and increased A2E levels (Chrispell et al., 2009). Recently, a third *Rdh12* knockout mouse model was generated using CRISPR/Cas9 gene editing on mice with the Met450Leu *RPE65* variant, which are more susceptible to light damage. Under normal light conditions, no phenotype was detected, however following 48 hours of illumination, *Rdh12*$^{-/-}$ mice displayed significant reduction in ERG a- and b-waves, thinner outer nuclear layer in the central retina and yellow-white punctate retinal flecks in the fundus (Bian et al., 2021). Despite the severe phenotype observed in patients, the *Rdh12*$^{-/-}$ mouse models do not recapitulate this phenotype, displaying a relatively mild phenotype, and thus present several limitations for the study of *RDH12* disease mechanisms.

Rdh8$^{-/-}$ *Rdh12*$^{-/-}$ double knockouts also showed mild light-dependent retinal degeneration, with delayed dark adaptation and reduced all-trans RDH activity with a build-up of atRAL, and subsequent accumulation of toxic A2E was observed (Maeda et al., 2007). Double knockout mice did however regenerate the visual pigment *in vivo* and triple knockout *Rdh8*$^{-/-}$, *Rdh12*$^{-/-}$, *Rdh5*$^{-/-}$ mice also had the ability to regenerate 11-cis retinal. RDHs do not appear to be necessary for the regeneration of the visual pigment in mice but are needed for clearance of atRAL in periods of excess illumination. It is possible that mice RDHs compensate for each other. Other disease models are required to help shed light on the pathogenesis of *RDH12*-retinopathies.

1.4.1.2. Zebrafish as a model organism

Zebrafish (*Danio rerio*) have become a widely used model organism to study a range of genetic diseases and provide a number of advantages. Firstly, they develop externally, outside of the mother, in a transparent chorion, and during the early stages of development they themselves are transparent, allowing researchers to easily monitor the development of the embryo. Secondly, they develop very rapidly; by 24 hours post fertilisation (hpf), all organs have already begun to form, and by 3 days, the embryos have hatched and are swimming freely. Zebrafish reach adulthood by 3 months and can breed in large numbers, with one breeding pair able to produce approximately 200 eggs per week (Glass and Dahm, 2004). Seventy percent of human genes have at least one zebrafish orthologue, and many have two due to an extra round of whole genome duplication in teleosts (Howe et al., 2013).

Mutagenesis in zebrafish can be achieved, at relatively low cost and with high efficiency, using genome editing techniques such as clustered regularly interspaced short palindromic repeat (CRISPR)/CRISPR associated protein 9 (Cas9). The CRISPR/Cas9 system consists of two components: single-guide RNA (sgRNA) and Cas9. The sgRNA is composed of CRISPR RNA (crRNA), trans-activating crRNA (tracrRNA) and a guide sequence that recognises and binds to a 20 base pair (bp) sequence, immediately followed by a protospacer adjacent motif (PAM), which has the sequence NGG. Cas9 binds to and cleaves the target sequence, generating a double stranded break (DSB). The DSB is then repaired by non-homologous end joining

(NHEJ), resulting in random insertions or deletions, which commonly result in frameshifts and premature termination, thereby causing loss-of function, and essentially “knock-out” of the gene. Homology directed repair (HDR) can also be used to generate knock-ins and introduce specific mutations with single nucleotide precision, with the aid of a DNA repair template that consists of the insertion sequence flanked by homologous sequences (homology arms) on either side (Sertori et al., 2016).

1.4.1.2.1. Zebrafish visual system

Zebrafish are an extremely useful model to study eye diseases, with zebrafish eye development and retinal organisation mimicking that of the human eye. Retinal structure is highly conserved across vertebrate species, and zebrafish retina therefore contains all the cell types found in the human retina: ganglion, bipolar, amacrine, photoreceptor and Müller glia cells. Eye development begins with evagination of the optic lobes from a cellular mass at 14 hpf. This gives rise to the optic cup by 20 hpf, which is composed of two layers: the retinal neuroepithelium and pigmented epithelium. The ganglion cells are the first of the neuroepithelium to differentiate at 40 hpf, followed by the amacrine and horizontal cells, with lamination across most of the retina observed by 48 hpf. The photoreceptors appear shortly after at 55 hpf, finally followed by the Müller glia cells. By 3 days post fertilisation (dpf), a visual startle response and electroretinogram can be detected (Richardson et al., 2017).

Zebrafish, like humans, utilise both rod and cone photoreceptors. In addition to the three types of cone cells present in humans, zebrafish possess a fourth type, which is sensitive to ultraviolet (UV) light. The canonical visual cycle regenerates the visual pigment in the rods and cones via the RPE. A second cone specific visual cycle also exists, involving the Müller cells (described in section 1.1.4). The majority of studies looking at the visual cycle have utilised mouse models, which are a rod-dominant species, where only 3% of photoreceptors are cones. Zebrafish, however, are a cone-dominant species, and studies have shown that both visual cycle pathways exist in zebrafish. Retinaldehyde binding protein-1 (RLBP1), also known as cellular retinaldehyde binding protein (CRALBP) is expressed in both the RPE and Müller glia cells, and knockout of *Rlbp1* in mice shows delayed dark adaptation and reduced 11-cis retinal levels. Zebrafish have two orthologues of *RLBP1*: *rlbp1a*, which is expressed in the RPE and *rlpb1b*, which is expressed in the Müller glia, therefore allowing the study of both pathways independently. Morpholino aided knockout of either orthologue resulted in a 50% reduction in 11-cis retinal levels, however loss of *rlbp1b* led to a greater reduction in ERG response, suggesting that the cone-specific visual cycle plays a more prominent role in zebrafish cones (Collery et al., 2008, Fleisch et al., 2008).

RDH12 is expressed in both rod and cone inner segments, and its role in the visual cycle is not entirely understood, due to the lack of phenotype in the *Rdh12*$^{-/-}$ mouse model. The zebrafish model may enable further study into the function of RDH12.

1.4.1.3. Light induced models of retinopathy

Animal models of inherited retinal dystrophies do not always fully recapitulate the phenotype observed in patients, with a milder or later onset phenotype observed in models compared to patients. Light is therefore a useful tool that can be used to induce or accelerate cell death in animal models of retinal degeneration. Indeed, all the *Rdh12* mouse models displayed a more pronounced phenotype when exposed to intense illumination. Several other studies have highlighted the usefulness of light in assessing retinal damage, for example the *Abca4*$^{-/-}$ mouse, a model of Stargardt's disease, does not display any photoreceptor loss up to 10 months of age under normal light conditions, however when mice are exposed to bright light, photoreceptor loss is induced, indicated by reduced thickness of ONL (Taveau et al., 2020). Similarly, in *ush2a*^{b1245} zebrafish embryos, photoreceptor cell death was significantly increased in embryos exposed to 72 hours constant illumination, compared to wildtype controls (Dona et al., 2018). These studies show light to be a valuable experimental tool to induce retinal damage in animal models, allowing investigation of cellular degeneration and molecular mechanisms in IRDs.

1.4.2. Cell culture models

Animal models are extremely useful as they allow study in a whole organism, however cell culture models provide the advantage of studying molecular pathways and disease mechanisms in a human system. Cell culture models provide a useful tool for the study of disease as they are well characterised, the cellular conditions and culture environment can be controlled, and they

are easy to work with. However, limitations are also presented, especially as the cell lines routinely used in labs are immortalised or cancer cell lines. Primary cell lines, derived directly from human tissue, like a biopsy, are closer to *in vivo* conditions as they have not been transformed, however they have a shorter lifespan with a limited number of passages they can undergo before becoming senescent (Vertrees et al., 2009). Although, limitations exist for cell culture models, they are still extremely useful and a valuable resource as a preliminary model for the study of many diseases, in particular studying disease mechanisms and determining effectiveness and toxicity of drugs, and indeed many key concepts known today about protein interactions, molecular mechanisms and pathways were derived from study in cell models. In the past decade, stem cell-based models have become an extremely popular and useful tool to study genetic conditions, in particular ocular disorders, as they enable study of retinal disorders in human retinal cells, derived from patients, which would otherwise be difficult to obtain.

1.4.2.1. RDH12 cell work

A number of studies have utilised *RDH12* transfected cell lines to study the enzyme activity of disease associated mutants. In COS-7 cells transiently transfected with various *RDH12* missense mutants, 11 out of 14 variants showed significantly reduced enzyme activity, 5-18% of wild type levels. They also showed decreased expression levels, most likely as a result of protein instability (Thompson et al., 2005). Enzyme activity was reduced by ~95% for p.Ala269Glyfs*2 and p.T49M variants (Sun et al., 2007), although some discrepancy regarding the p.T49M variant is observed in the literature with

some studies reporting higher catalytic activity compared to wild type RDH12 (Janecke et al., 2004, Thompson et al., 2005, Lee et al., 2007). The p.C201R variant displayed no enzyme activity, consistent with the C201 residue being located in the highly conserved active site of RDH12 (Sun et al., 2007). Lee et al. (Lee et al., 2007) studied the effect of 6 variants that resulted in substitutions in the cofactor or substrate binding sites, in Sf9 cells. In all cases, expression yields were lower for mutant proteins, and reduced activity was observed in 4 of the 6 mutants. *RDH12* missense variants, p.T49M and p.I51N, transiently transfected in HEK-293 cells, were shown to degrade at a faster rate than the wildtype protein with significantly lower half-lives (Lee et al., 2010). Accelerated degradation of mutant protein may be a result of misfolding, resulting in the lower protein expression levels and subsequent reduced catalytic activity. Additionally, HEK-293 cells transfected with the p.T49M mutant lose their ability to protect against 4-HNE induced apoptosis (Marchette et al., 2010).

1.4.3. Induced pluripotent stem cells

Embryonic stem cells (ESC) have the ability to differentiate into any cell type. However, they are difficult to obtain, and raise ethical concerns. The ability to reprogram somatic cell types into induced pluripotent stem cells (iPSC) was first developed in 2006, where mouse fibroblasts were successfully reprogrammed to iPSCs via overexpression of the “Yamanaka” factors (OCT4, SOX2, KLF4, c-MYC) (Takahashi and Yamanaka, 2006). A year later human fibroblasts were similarly reprogrammed to iPSCs by the Yamanaka group using the same factors (Takahashi et al., 2007), and by the Thomson

group using OCT4, SOX2, NANOG and LIN28 (Yu et al., 2007). iPSCs were shown to behave in a similar manner to ESCs, with the properties of pluripotency, the ability to differentiate into any cell type, and self renewal. Cells can be obtained from a patient, most commonly as fibroblasts from a skin biopsy, or peripheral blood mononuclear cells (PBMCs) from blood, and reprogrammed to iPSCs, however methods of reprogramming from urine and hair have also been described (Raab et al., 2014). The original reprogramming methods utilised retro- and lenti-viral vectors, however this came with the disadvantage of integrating into the cells' genome, and possibility of tumour formation, therefore could not be used for clinical applications. Now, a number of non-integrating reprogramming methods have been developed, which can be divided into two types, viral and non-viral. One of the most commonly used viral transfection agents is Sendai virus, which is an RNA virus that does not enter the nucleus of the transfected cell and can produce large amounts of protein. It can be used in most cell types with a relatively high transfection efficiency, with 1% reprogramming efficiency in fibroblasts. A common method of non-viral transfection is the use of episomal plasmids, allowing transient expression of the reprogramming factors. This is achieved by using oriP/ Epstein-Barr nuclear antigen-1 (EBNA) plasmids, which are retained extrachromasomally and replicate with the cell. Episomal oriP/EBNA-based plasmids allow delivery of the reprogramming factors via a single transfection, allowing stable expression of the factors for a long enough period to induce reprogramming of the somatic cells, however efficiency is lower. Delivery of reprogramming factors is generally achieved via two methods, lipofection or

electroporation. Usually, 25 days after transfection, individual iPSC colonies appear which are isolated and expanded. Both Sendai virus and episomal DNA is lost by serial dilution through passaging, generating transgene-free iPSCs by passage 10 (Malik and Rao, 2013, Rao and Malik, 2012, Wang and Loh, 2019). Reprogramming to iPSCs is confirmed by expression of pluripotency markers, like OCT4, SOX2, NANOG, SSEA-3 and SSEA-4. Pluripotency is determined by differentiation potential to the three germ layers, through teratoma formation or random differentiation of embryoid bodies (EB) and chromosomal integrity is confirmed by G-band karyotyping.

iPSCs can be differentiated to several different cell types, including cardiomyocytes, neurons, hepatocytes and RPE. iPSC differentiation protocols have now further progressed to enable differentiation into multi-cell type three dimensional retinal organoids. Retinal tissue is difficult to obtain, therefore iPSC modelling provides an extremely valuable tool to study disease mechanisms in patients and opens the avenue for personalised medicine.

1.5. Aims

The goal of my project is to advance our understanding of the disease mechanisms of *RDH12*-related retinopathies, in order to identify therapeutic targets and aid in the development of new therapies. This will be achieved through the generation of a number of disease models. The specific aims of my project are to:

i. Express and purify recombinant RDH12, in order to study protein structure.
ii. Generate a *rdh12* zebrafish knockout model using CRISPR/Cas9 gene editing and characterise the retinal phenotype.
iii. Generate HEK-293 stable cell lines, expressing wild type and mutant RDH12, in order to study the function of RDH12, disease mechanisms and screen for potential therapeutics.
iv. Generate iPSC lines from two patients with *RDH12*-retinopathies, one with an autosomal dominant mutation and one with an autosomal recessive mutation, and wildtype controls.

2. Materials and methods

2.1. Protein expression and purification

2.1.1. Cloning

Full length human RDH12 with N-terminal BamHI and C-terminal EcoRI restriction sites was purchased from Gene Art Strings (Thermo Fisher Scientific), restriction digested with CutSmart (New England Biolabs; NEB), and cloned into two vectors: (i) pHT, which is a prSET(A) based vector with an N-terminal 6xHis-tag and thrombin cleavage site (ii) pHLT, which has an N-terminal 6xHis-tag, a dihydrolipoyl dehydrogenase domain to increase protein solubility, and a thrombin cleavage site, using T4 DNA ligase (NEB). The 6xHis-tag has a high affinity for Nickel ions (Ni^{2+}) and is used for purification of the protein. The thrombin cleavage site allows removal of the tag from the target protein. The ligation mixture was transformed into competent *E. coli* XL1-blue cells and spread onto LB agar plates, containing 100 µg/ml carbenicillin, and cultured overnight at 37 °C. Individual colonies were grown overnight at 37 ºC in LB broth supplemented with carbenicillin, and plasmid DNA was purified using QIAprep Spin Miniprep Kit (QIAGEN). Clones with the correct orientation of insert were verified by Sanger sequencing using the T7 promoter primer (5'-TAATACGACTCACTATAGGG).

To assess whether removal of the predicted signal peptide would improve expression efficiency, shorter constructs were created. DNA was amplified by polymerase chain reaction (PCR) using construct specific forward primers, containing the BamHI restriction site (**Table 1**) and the reverse

primer 5'-GATCGATCGAATTCTCATTACTACTCC, containing the EcoRI restriction site (underlined), from pHT vector containing full length RDH12. The PCR product was purified using QIAquick gel extraction kit (QIAGEN), cleaved using BamHI and EcoRI restriction enzymes and cloned into vector as before. The resulting construct encoded N-terminal truncated RDH12 fused to an N-terminal 6xHis-tag.

Full length RDH12 was also cloned into the pOPINE vector, which has a C-terminal 6xHis tag. pOPINE was a gift from Ray Owens (Addgene plasmid # 26043) (Berrow et al., 2007)

Construct	**Forward primer**
31-316aa	5'-GATCGATCGGATCCTGTAGAACAAATGTGCAGC
21-316aa	5'-GATCGATCGGATCCTCCATTCAGGAAGTTCTTTGC
39-316aa	5'-GATCGATCGGATCCGGCAAGGTAGTGGTGATC

Table 1: Forward primers used to PCR amplify shorter constructs from full length RDH12.
BamHI restriction site is underlined.

2.1.2. Small scale *E.coli* expression trials

Plasmids were transformed into *E. coli* BL21 (DE3) RIL cells and a starter culture was grown overnight at 30 °C in LB medium, containing 100 µg/ml carbenicillin and 35 µg/ml chloramphenicol. Starter culture was then added to 50 ml LB medium at a 1:100 ratio, containing carbenicillin and chloramphenicol, and cultured at 37 ºC until an OD_{600} of 0.6-0.9 was reached. Cultures were then induced with 0.5 mM isopropyl β-D-1-

thiogalactopyranoside (IPTG) and cultured for 2 hours, 4 hours and overnight at 37 °C, and overnight at 21 °C. Cells were harvested by centrifugation at 3600 revolutions per minute (rpm) at 4 ºC, and resuspended in lysis buffer (50 mM Tris-HCl (pH 7.5), 200 mM NaCl, 10 mM imidazole, 5% glycerol), sonicated and centrifuged at maximum speed for 20 minutes at 4 °C. Amintra Ni-NTA Affinity Resin (Expedeon) was used to purify His-tagged protein. Nickel resin was washed in buffer and spun at 1500 rpm for 2 minutes. Supernatant was added to the beads and incubated on rollers at 4 °C for 1 hour. The samples were spun down, and supernatant was removed, a sample was retained to run as the unbound fraction on a gel. Resin was washed 3 times in buffer at 1500 rpm for 1 minute each time. For expression testing, an equal amount of sodium dodecyl sulphate (SDS) loading buffer was added, boiled at 95 °C for 5 minutes, spun down and supernatant was loaded onto a RunBlue Bis-Tris gel (Expedeon) and run at 200 V for 40 minutes in MES running buffer. Gels were stained with Instant Blue protein stain (Expedeon) and imaged.

2.1.3. Large scale *E.coli* protein expression

For large scale expression of recombinant RDH12, plasmids were transformed into *E. coli* BL21 (DE3) RIL cells as above and 10 ml starter culture was added to 1 litre of LB medium, containing carbenicillin and chloramphenicol, and cultured at 37 ºC until an OD_{600} of 0.6-0.9 was reached. Cultures were then induced with 0.5 mM IPTG and cultured at required temperature. Cells were harvested by centrifugation at 3600 rpm at 4 ºC and stored at -80 ºC until purification.

2.1.4. Protein purification

Cell pellets were resuspended in buffer A (50 mM Tris-HCl (pH 7.5), 200 mM NaCl, 20 mM imidazole, 5 % glycerol), with the addition of a protease inhibitor tablet, sonicated and centrifuged at 17,000 rpm for 1 hour. Protein was purified using immobilised metal affinity chromatography (IMAC). Supernatant was filtered and loaded on to a 5 ml His-trap nickel column, in buffer A, washed and eluted in same buffer except 250 mM imidazole, using the AKTA purifier system (GE Healthcare), running the Unicorn 5 software. A 10 µl aliquot from each fraction was taken and run on a gel and analysed by SDS-polyacrylamide gel electrophoresis (SDS-PAGE). Fractions containing soluble protein was dialysed overnight into buffer B (50 mM Tris-HCl (pH 8), 50 mM NaCl, 5% glycerol), to remove imidazole. Sample was then loaded on to a 1 ml HiTrap Q HP anion exchange column (GE Healthcare) in buffer B and eluted in the same buffer, except with 1 M NaCl. For size exclusion chromatography, 2 ml sample was loaded onto a 120 ml Superdex 200 (S200) gel filtration column in buffer B, in the presence of 1 mM DTT.

2.1.5. Mammalian protein expression and purification

For mammalian expression, a vector encoding full length RDH12 (NM_152443) tagged to C-terminal 6xHis-tag (EX-T4186-M77) was obtained from GeneCopoeia. Plasmid was transformed into TOP10 bacteria and plated on ampicillin-resistant plates overnight at 37 °C. Colonies were picked and grown in LB broth overnight at 37 °C. Cells were pelleted at 4000 rpm for 15 minutes, and DNA extracted using the Plasmid Maxi Kit (Qiagen), following manufacturer’s instructions. Human Expi293 cells were transfected

with vector and collected after 7 days. RDH12 was purified using a similar protocol to Belyaeva et al. (2005). Pellet was resuspended in 50 mM HEPES (pH 7.5), 200 mM NaCl, 10mM $MgCl_2$, 5% glycerol, protease inhibitor, Pierce nuclease inhibitor, 1 mM tris(2-carboxyethyl) phosphine (TCEP), 15 mM imidazole (pH 7.5), sonicated and centrifuged at 12000 g for 20 minutes. The supernatant was collected and resuspended in the above buffer including 15 mM 1,2-diheptanoyl-*sn*-glycero-3-phosphocholine (DHPC) in a sonicating bath, then centrifuged at 30000 rpm for 20 minutes. A column was packed with Ni Sepharose 6 Fast Flow beads. Supernatant was loaded on to the column, washed and purified protein eluted with buffer including 300 mM imidazole.

2.2. Zebrafish husbandry

wt, AB strain (wt), and *rdh12*^{u533} zebrafish were bred and maintained according to local UCL and U.K. Home Office regulations for the care and use of laboratory animals under the Animals Scientific Procedures Act at the UCL Bloomsbury campus zebrafish facility. Zebrafish were raised at 28.5 °C on a 14 h light/10 h dark cycle. UCL Animal Welfare and Ethical Review Body approved all procedures for experimental protocols, in addition to the U.K. Home Office (License no. PPL PC916FDE7). All approved standard protocols followed the guidelines of the ARVO Statement for the Use of Animals in Ophthalmic and Vision Research Ethics. Zebrafish were terminally anaesthetised in 0.2 mg/mL Tricaine (MS−222) for sample collection

2.3. CRISPR/Cas9 gene editing

2.3.1. sgRNA synthesis

CRISPR targets were identified using Benchling's CRISPR Guide Design Software, and the following 20 base pair (bp) target sequence in *rdh12* exon 1 was chosen. PAM site is underlined:

5' – TGGCGTTCGCGGCGGGTTTA *GGG*

A gene-specific DNA oligonucleotide consisting of the T7 promoter, the 20 bp target sequence without the PAM, and a 20 bp sequence that overlapped to a generic sgRNA template (constant oligonucleotide) was designed as follows (Gagnon et al., 2014):

5'-TAATACGACTCACTATA – $GGN_{(20)}$ – GTTTTAGAGCTAGAAATAGC-3'

The sequence of the constant oligonucleotide was:

5'-AAAAGCACCGACTCGGTGCCACTTTTTCAAGTTGATAACGGACTAGC CTTATTTTAACTTGCTATTTCTAGCTCTAAAAC-3'

Oligonucleotides were ordered as standard desalted oligos from Sigma Aldrich. The gene specific and constant oligonucleotides were annealed under the following conditions: 95 °C for 5 minutes, ramping down to 85 °C at -0.1 °C/second, ramping down to 25 °C at -0.02 °C/second, then holding at 4 °C. T4 DNA polymerase (NEB) was used to fill in the ssDNA and incubated at 12 °C for 20 minutes. The double stranded DNA (dsDNA) template was cleaned up using the QIAquick PCR purification kit (QIAGEN) and run on a 2% agarose gel to verify a product of the correct size. sgRNA transcription

was carried out using the NEB T7 kit, according to manufacturer's instructions. Sample was then DNase treated with TURBO DNase for 15 mins at 37 °C, and purified using RNeasy mini kit (QIAGEN), according to manufacturer's instructions.

2.3.2. Cas9 mRNA synthesis

The Cas9 plasmid pT3Ts-nCas9n (Addgene #46757) was linearized with XbaI (Promega), cleaned up and transcribed using the T3 mMessage mMachine kit (Thermo Fisher Scientific), according to manufacturer's instructions and DNase treated with TURBO DNase. A Poly(A) tail was added using the Poly(A) tailing kit (Ambion), according to manufacturer's instructions and cleaned up using the RNeasy mini kit (QIAGEN).

2.3.3. Zebrafish injections and breeding

Injections and breeding were carried out by Dr Maria Toms.

Wildtype zebrafish embryos were co-injected with 75 ng/µl sgRNA and 150 ng/µl Cas9 mRNA at the one-cell stage using a Picospritzer III intracellular microinjector (Parker). Embryos were collected at 24 hpf, DNA was extracted and an *rdh12* DNA sequence of 485 bp was PCR amplified using MyTaq DNA polymerase (Bioline) with the *rdh12* exon 1 primers which spanned the target site. The sequences were as follows:

Forward primer 5'-GGAGGCTGCTGAACACATTC

Reverse primer 5'-CGATTTCTGGAGCAGATCATGTC

The cycle conditions used were: incubation at 95 ˚C for 1 minute for initial denaturation, followed by 35 cycles of 95 ˚C for 15 seconds (denaturation);

60 ˚C for 15 seconds (annealing) and 72 ˚C for 15 seconds (extension). Samples were analysed using Sanger sequencing.

Injected embryos were raised to adulthood to generate ‘founder fish’ (F0) and outcrossed with wildtype (wt) fish and embryos were analysed for mutations by Sanger sequencing. Founder fish that transmitted mutations were crossed with wt fish to produce the F1 generation, which carried heterozygous mutations. These fish were then outcrossed with wt fish to produce an F2 generation with fewer potential off-target mutations. Heterozygous fish from the F2 generation carrying the same mutation were then in-crossed to produce the F3 generation. F3 fish were raised to adulthood, genotyped and homozygous fish were crossed to produce the F4 generation. Homozygous fish were used for all further characterisations.

2.4. Immunohistochemistry

Adult enucleated eyes or whole embryos were fixed in 4% paraformaldehyde (PFA) in phosphate buffered saline (PBS) overnight, washed and incubated in 30% sucrose/PBS for 4 hours at room temp. Samples were embedded in Tissue-Tek OCT and frozen on dry ice. Sections were cut at a thickness of 12 µm using Leica CM1850 cryostat and collected on Superfrost PLUS (Thermo Scientific) slides. Sections were washed 3 times for 10 minutes each, then blocked in 20% goat serum, 0.5% TritonX-100 in PBS for 1 hour at room temperature. Slides were incubated with primary antibody in 2% normal goat serum (NGS) overnight at 4 ˚C (**Table 6**). Slides were washed and incubated with secondary Alexa Fluor antibodies (1:400 in 2% NGS) for

1 hour, washed and mounted with Prolong Diamond with DAPI (Thermo Fisher Scientific). Slides were imaged on Leica LSM 710 confocal microscope.

2.5. Terminal deoxynucleotidyl transferase dUTP nick end labeling (TUNEL) assay

Cryosections were prepared as described above (section 2.4). TUNEL assay was performed using the ApopTag Plus Fluorescein In Situ Apoptosis Detection Kit (Merck Millipore), according to manufacturer's instructions.

2.6. Retinal histology

Whole embryos were fixed in 4% PFA/PBS overnight at 4 ˚C, washed in PBS and water three times each, then dehydrated through an ethanol series (30%, 50%, 70%, 95%, 100% for 2 minutes each). Samples were then embedded using JB-4 embedding kit (Polysciences Inc., Warrington, PA, USA). Sections were cut at a thickness of 7 µm, stained with 1% toluidine blue and imaged on an EVOS FL microscope (Thermo Fisher Scientific). For adult fish, enucleated eyes embedded for electron microscopy, as described below (section 2.7), were sectioned at a thickness of 1 µm, stained with 1% toluidine blue and imaged in bright field on a Zeiss AxioImager M2 microscope.

2.7. Transmission electron microscopy (TEM)

TEM was carried out by the Electron Microscopy facility at the Francis Crick Institute.

For TEM analysis, enucleated zebrafish eyes were fixed in 2% PFA/2% glutaraldehyde prior to incubation with 1% osmium tetroxide. Following dehydration in an ethanol series and propylene oxide incubation, the zebrafish retinas were embedded in Epon 812 resin. The blocks were then mounted for micro-computed tomography (micro-CT) on a cylindrical specimen holder with Loctite Precision Max super glue. Tomographic imaging was conducted in an Xradia Versa 510 (Carl Zeiss). A low resolution scan was captured at 40kV/3W, with a pixel size of ~5 µm. The data were exported as tiff and the region of interest was identified in each sample, just above the optic nerve and showing the lens. Blocks were then sectioned using a UC7 ultramicrotome (Leica Microsystems) and 70 nm sections were picked up on Formvar-coated 2 millimetre (mm) slot copper grids and post-stained with Reynolds lead citrate for 5 minutes. Sections were viewed using a 120 kV Tecnai G2 Spirit transmission electron microscope (FEI Company, Eindhoven, Netherlands) and images were captured using a OneView UltraScan® 4000 camera (Gatan Inc., Pleasanton, USA) and Serial EM software (Mastronarde, 2003). For each sample, a montage of the whole section was done at 100x. Several regions of the retina were then imaged at 690x, 2900x and 6800x magnification. The images were stitched together using IMOD (Kremer et al, 1996). Visualisation was done in 3dmod. Images were analysed using ImageJ.

2.8. High performance liquid chromatography (HPLC) analysis of atRAL levels in zebrafish

Retinoids were extracted according to the protocol by Costaridis et al. (Costaridis et al., 1996). Approximately 250 embryos or adult enucleated eyes were collected and sonicated in 1 ml stabilising buffer (PBS, 0.5% ascorbic acid, 0.5% EDTA, 0.3% sodium sulphate, pH 7.3). Sample was extracted twice in 2 ml extraction solvent (8:1 ethyl acetate: methyl acetate plus 0.5% butylated hydroxytoluene), with vigorous shaking for 30 minutes. Extracts were combined and dried under nitrogen gas and redissolved in acetonitrile. HPLC analysis was performed using a Waters ACQUITY® UPLC®. Elution was monitored at 360 nm for atRAL with a Waters ACQUITY 2996 PDA. The stationary phase was Waters ACQUITY UPLC BEH C18 1.7 µm, 2.1 × 50 mm column and the mobile phase consisted of acetonitrile/water 0.1% formic acid (87.5:12.5). The analysis lasted 8 minutes, with a flow rate of 0.25 ml/minute and a 10 µl injection.

2.9. SOD and CAT Activity Assay

SOD activity was determined using the SOD assay kit (Sigma Aldrich; 19160) according to the manufacturer's instructions. CAT activity was determined using the catalase activity assay kit (Abcam; ab83464), according to the manufacturer's instructions.

2.10. Reverse transcription quantitive PCR (RT-qPCR)

Total RNA was extracted from cells using the RNeasy mini kit and from whole embryos and enucleated adult eyes using the RNeasy FFPE kit

(QIAGEN), according to manufacturer's instructions. Complementary DNA (cDNA) was synthesised from 1 µg of RNA using the Superscript II First Strand cDNA synthesis kit (Invitrogen), according to the manufacturer's instructions. Transcript levels were analysed using SYBR Green Master Mix (Thermo Fisher Scientific) on a StepOne Real-Time PCR system (Applied Biosystems), under standard cycling conditions. All samples were assayed in triplicate. Primer sequences are shown in **Table 7**.

2.11. Generation of stable cell line expressing RDH12

2.11.1. Expression plasmids

The open reading frame (ORF) expression clone was obtained from GeneCopoeia, and encoded RDH12 (NM_152443) with a C-terminal (pEZ_M98) green fluorescent protein (GFP) tag. To create stocks, plasmids were transformed into TOP10 bacteria and plated on ampicillin-resistant plates overnight at 37 °C. Colonies were picked and grown in LB broth overnight at 37 °C. Cells were pelleted at 4000 rpm for 15 minutes, and DNA extracted using the ZymoPURE II Plasmid Maxiprep Kit (Zymo Research), following manufacturer's instructions.

2.11.2. Site directed mutagenesis

Patient mutations were introduced into the plasmid using the Quickchange II Site-Directed Mutagenesis kit (Agilent). Primers were designed, according to kit instructions with approximately 10 bases of correct sequence either side of the mutation (**Table 2**). The reaction was set up with 20 ng of plasmid, 125 ng of each primer, dNTP and reaction buffer. Then 1 µl of *PfuUltra* HF DNA

polymerase was added and the reaction was run under the following cycling parameters: 95 °C for 30 seconds, then 16 cycles of 95 °C for 30 seconds, 55 °C for 1 minute, 68 °C for 7 minutes. The reaction was placed on ice to cool down and 1 µl of *Dpn1* restriction enzyme was added and incubated at 37 °C for 1 hour. Then, 1 µl of reaction mix was transformed into 50 µl of XL1-Blue Supercompetent cells and plated onto LB-ampicillin plates overnight. Individual colonies were picked and grown in LB broth with 100 µg/ml ampicillin overnight at 37 °C, then purified using QIAprep Spin Miniprep Kit (QIAGEN). Colonies with the correct mutation were verified by Sanger sequencing using the following primers:

Forward primer – 5'-GCGGTAGGCGTGTACGGT

Reverse primer – 5'-CCGGACACGCTGAACTTGT

Mutation	Protein change	Primers
c.677A>G	p.Y226C	5'-cggggtcaccacctgcgcagtgcac 5'-gtgcactgcgcaggtggtgaccccg
c.325G>C	p.A109P	5'-ctatccgagcctttcctgagggctttctgg 5'-ccagaaagccctcaggaaaggctcggatag
c.38C>A	p.S13*	5'-gctcacctccttcttctagttcctgtatatggtag 5'-ctaccatatacaggaactagaagaaggaggtgagc

Table 2: Primers used for site directed mutagenesis.
The mutated base pair is shown in red.

2.11.3. HEK-293 culture

Human embryonic kidney 293 cells (HEK-293) cells were cultured in Dulbeccos modified Eagles medium (DMEM) high glucose, 10% foetal bovine serum (FBS) and Penicillin/Streptomycin (Pen/strep; Thermo Fisher

Scientific) and medium was changed every 3-4 days. Cells were passaged at 80-90% confluency using TrypLE Express (Thermo Fisher Scientific) and plated at a split ratio of 1:20.

2.11.4. Stable cell line generation

HEK-293 cells were plated in 6 well-plates at a density of 600,000 cells per well in 2 ml medium. After 24 hours cells had reached 90% confluency and were transfected using Lipofectamine 2000 Reagent (Thermo Fisher Scientific). Lipofectamine 2000 (10 µl) and plasmid DNA (4 µg) were separately prepared in 250 µl Opti-MEM reduced serum medium and incubated for 5 minutes. Lipofectamine 2000 and DNA were then mixed and incubated for a further 20 minutes and added to cells. Cells were assessed for GFP fluorescence 24 hours later under a fluorescent microscope to confirm transfection. Twenty-four hours after transfection, cells were passaged into 96 well plates in selection media (DMEM high glucose, 10% FBS, 1 mg/ml G418) using serial dilutions to achieve low cell density. After 10 days, all non-transfected cells died off and after a further 2 weeks transfected cells formed distinct colonies. Individual colonies were picked into 24 well plates and expanded. For continued culture, G418 concentration was reduced to 0.5 mg/ml.

2.12. Western blot

Cells were lysed in RIPA buffer (Pierce), and protein concentration quantified using BCA Protein Assay kit (Peirce). Thirty micrograms of each sample was loaded on to NuPage 4-12% Bis-Tris gel (Invitrogen) and run at 90 V for 50

minutes in MES running buffer (Invitrogen). Gel was then transferred to nitrocellulose membrane at 60 mA for 60 minutes. Membrane was blocked for 1-2 hours at room temperature in 5% milk in PBSTween (0.1%) and incubated with primary antibody overnight at 4 °C. Membrane was washed and incubated with 1:10000 HRP-conjugated secondary antibodies (Sigma Aldrich) for 1 hour at room temperature, and signal detected using the ECL Prime Western Blot Detection Kit (BioRad). Blot was stripped using Restore western blot stripping buffer (Thermo Fisher Scientific) and re-probed with 1:5000 anti-β-actin (Sigma Aldrich A2228) as a loading control. Antibodies used are listed in **Table 6**.

2.13. Immunocytochemistry

Cells were fixed in chamber slides or wells in 4% PFA/PBS for 20 minutes at 4 °C. For ER staining, cells were permeabilised in 100% cold methanol for 5 minutes at room temperature. Cells were then blocked for 1 hour in 10% NGS, 0.1% TritonX-100 in PBS at room temperature and incubated overnight at 4 ˚C with primary antibodies diluted in 1% NGS at room temperature (**Table 6**). After PBS washes, Alexa Fluor secondary antibody was added at a dilution of 1:400 in 1% NGS for 1 hour and nuclei were counterstained for DAPI. Slides were washed and mounted with Prolong Diamond with DAPI and imaged on Leica LSM 710 confocal microscope. Cells in well plates were washed and imaged on an EVOS M7000 Imaging System (Thermo Fisher Scientific).

2.14. Drug compounds

atRAL was obtained from Sigma Aldrich (R2500) and prepared at a stock concentration of 10 mM in dimethylsulphoxide (DMSO). Pregabalin (Sigma Aldrich) was prepared in sterile water at a concentration of 10 mg/ml. N-acetylcysteine amide (NACA) (TOCRIS) was prepared in sterile water at a concentration of 10 mM. Taurordeoxycholic acid (TUDCA) (Cayman Chemical) was dissolved in DMSO at a stock concentration of 20 mM.

2.15. Cell viability MTT assay

Cells were plated at a density of 40,000 cells per well in a 96 well plate. Cells were incubated with various concentrations of test compound for 24 hours. Cell viability was determined using MTT (3-(4,5-dimethylthiazol-2-yl)-2,5-diphenyltetrazolium bromide) (Invitrogen; M6494). Following dosing, treatment media was replaced with 100 µl fresh media. MTT was prepared at a concentration of 5 mg/ml in PBS, and 10 µl was added to each well. Cells were incubated for 4 hours at 37 ˚C. All but 25 µl media was removed, MTT was solubilised with the addition of 50 µl DMSO and incubated at 37 ˚C with shaking for 10 minutes. Absorbance was read at 540 nm on a TECAN Safire2 plate reader.

2.16. Drug dosing

Cells were plated in 6 well plates at a density of 700,000 cells per well. After 24 hours, drugs were added to the cells in culture media. Twenty-four hours later, cells were pelleted and stored at -80 ˚C for further analysis.

2.17. RDH12 activity assay

Cell pellets were resuspended in PBS, lysed by sonication and centrifuged at 13000 rpm for 10 minutes. Supernatant was collected and protein concentration determined using BCA protein assay kit (Pierce). Reactions were carried out in 500 µl PBS, using 50 µg protein, 1 mM NADPH (Cayman Chemical) and 2.5 mM atRAL. Reaction was initiated with the addition of NADPH and incubated at 37 ˚C for 15 minutes and stopped by the addition of 500 µl cold methanol. Retinoids were extracted according to the protocol by Chetyrkin et al. (2001) on Waters Sep-Pak C18 coulmn. Column was washed with 1 ml acetonitrile, equilibrated with 2 ml acentonitrile:water (40:60). Sample was then loaded on to the column, washed with acetonitrile: water (40:60), eluted in 2 ml methanol:acetonitrile (5:95) and evaporated under nitrogen gas and reconstituted in 100 µl acentonitrile. HPLC analysis was performed using a Waters ACQUITY® UPLC®. Elution was monitored at 325 nm for atROL and 360 nm for atRAL with a Waters ACQUITY 2996 PDA, and peaks compared to standards. The stationary phase was Waters ACQUITY UPLC BEH C18 1.7 µm, 2.1 x 50 mm column and the mobile phase consisted of acetonitrile: water 0.1% formic acid (87.5:12.5). The analysis was 8 minutes, with a flow rate of 0.25 ml/minute and a 10 µl injection. Retinol was quantified by integration of the peak area.

2.18. Statistical analysis

All statistical analysis was performed using GraphPad Prism 8. All data are expressed as mean ± SEM of at least three independent experiments. For all analyses, Shapiro-Wilk normality test was initially carried to determine if data

is normally distributed, and appropriate statistical test was chosen. For comparison between two groups, data were analysed either using paired or unpaired t-test, depending on experimental design or Mann-Whitney test. For more than two groups, statistical significance was analysed using one-way ANOVA, followed by Sidak's multiple comparison test. For grouped analyses, two-way ANOVA with Dunnets multiple comparison test was used. P value of < 0.05 was considered significant.

2.19. Generation of patient derived induced pluripotent stem cell lines

2.19.1. Derivation of fibroblasts

A skin biopsy was taken from two patients with *RDH12* variants (**Table 3**). Biopsies were placed into digestion medium (DMEM high glucose, GlutaMAX Supplement, pyruvate, 20% FBS, 0.25% Collagenase I, 0.05% DNase I Pen/strep) and incubated overnight at 37 °C in 5% CO_2 humidified incubator. The biopsies were then vortexed for 10 seconds, resulting in the separation of the epidermis and disintegration of the dermis. Growth medium (DMEM high glucose, 15% FBS and Pen/Strep) was added to the biopsy and plated in a T25 flask and incubated for 3 days without touching. Fibroblasts were seen growing on day 3. Medium was changed every 3-4 days and passaged to a T75 flask at 80% confluency.

Cell line	Mutation	Gender	Age (years)	Ethnicity
RDH12 AD	c.759del p.(Phe254Leufs*24)	Male	32	Kurdistan and Tunisian
RDH12 AR	c.619A>G p.(Asn207Asp)	Female	40	Pakistani

Table 3: Summary of cell lines.

2.19.2. Fibroblast culture

Fibroblasts were cultured in growth medium (DMEM high glucose, 15% FBS, Pen/Strep) and medium was changed every 3-4 days. Cells were passaged at 80% confluency using TrypLE Express (Thermo Fisher Scientific) and plated at a split ratio of 1:4.

2.19.3. Validation of mutations

DNA was extracted from cell pellets using QIAamp DNA Micro Kit (QIAGEN). *RDH12* was amplified using MyTaq DNA polymerase (Bioline) with exon 8 primers for RDH12 AD and exon 7 primers for RDH12 AR (**Table 4**). Mutations were confirmed by Sanger sequencing.

RDH12 exon 8 forward	5'-TGGCCAGGAGTGGTACCTGC
RDH12 exon 8 reverse	5'-GCAACTCTTCCCAACACATA
RDH12 exon 7 forward	5'-GACCATTAGAGTTACTCATGGC
RDH12 exon 7 reverse	5'-CGTGCATGTTTGACAGCCTG

Table 4: Genotyping primer sequences

2.19.4. iPSC reprogramming of RDH12 AD fibroblasts

For reprograming of fibroblasts, cells below passage 5 were used. Cells were reprogrammed using integration-free episomal plasmids (**Table 5**). Reprogramming was carried out using the Neon Transfection System (Thermo Fisher Scientific) 100 µl kit. Cells were dissociated using TrypLE Express and counted using Countess II Automated cell counter (Thermo Fisher Scientific). For each transfection, $1x10^6$ cells were resuspended in 100 µl buffer R and mixed with 1.25 µg of each plasmid. Sample was loaded into the Neon pipette tip and transfected using the Neon transfection device with the following settings: 1700 V, 20 ms pulse width, 1 pulse. Cells were plated into 1 well of a six well matrigel (Corning) coated plate in fibroblast growth media. Medium was changed on days 3 and 4 with fibroblast media. On day 5, medium was changed to 3:1 fibroblast medium:mTeSR Plus (STEMCELL Technologies). On days 6 and 7, medium was changed to 1:1 fibroblast medium:mTeSR Plus, and from day 9 onwards medium was changed daily with mTESR Plus. Typically, around day 15 colonies begin to appear. From days 21-28, colonies were manually dissected and placed individually into 24 well plates in mTESR Plus. Medium was changed daily, and when confluent manually passaged into a 12 well plate, and then a 6 well plate.

Episomal Plasmid	Addgene ID	Encodes
pCXLE-Hsk	27078	SOX2 and KLF4
pCXLE-Hul	27080	L-MYC and LIN28
pCXLE-hOCT3/4-shp53-F	27077	OCT3/4 and shRNA against p53
pCXWB-EBNA1	37624	transient EBNA-1

Table 5: Episomal plasmids used for reprogramming fibroblasts to iPSCs

2.19.5. iPSC reprogramming of RDH12 AR fibroblasts

The protocol from Parfitt et al. (2016) was used for reprogramming of RDH12 AR fibroblasts. Fibroblasts were transfected as above using the following NEON settings: 1650 V, 10 ms, 3 pulses, and plated onto a gelatine coated 10 cm dish in fibroblast growth media, supplemented with 0.5 mM sodium butyrate for 7 days, and medium was changed every other day. On day 7, cells were dissociated using TrypLE Express and plated onto matrigel coated 6 well plates at a density of 250,000 cells/well in mTeSR Plus. Medium was changed daily, and colonies begin to appear approximately 14 days later. Individual colonies were manually dissected and placed individually into 24 well plates in mTESR Plus. Medium was changed daily, and when confluent manually passaged into a 12 well plate, and then a 6 well plate.

2.19.6. iPSC culture

iPSCs were cultured in matrigel coated 6 well plates in mTeSR Plus and passaged at 70-80% confluency, using ReleSR (STEMCELL Technologies)

and plated at a split ratio of 1:10 – 1:20, depending on the growth rate of the cell line.

2.20. iPSC characterisation

2.20.1. Alkaline Phosphatase expression

Undifferentiated cells express high levels of alkaline phosphatase (AP). Cells were fixed and stained using the Alkaline Phosphatase Staining Kit II (ReproCELL), according to manufacturer's instructions. Undifferentiated cells appear red after staining and differentiated cells appear colourless.

2.20.2. Random differentiation of embryoid bodies

Embryoid body (EB) formation was used to confirm differentiation potential into the 3 germ layers. iPSCs were passaged and plated in Aggrewell medium (STEMCELL), supplemented with 10 μM Y27632 (Sigma), in low adherence plates until they formed EBs (~7-10 days). EBs were plated on gelatine coated plates in DMEM/20% FBS and allowed to grow for 1-2 weeks. Immunostaining was carried out, as described in section 2.13, with markers for each of the germ layers (AFP – endoderm marker, Vimentin – mesoderm marker, PAX6 – ectoderm marker). Antibodies and dilution used are described in **Table 6**.

2.20.3. Karyotyping

iPSCs were sent to Cell Guidance Systems for karyotyping and 20 metaphases were counted.

2.20.4. Low-pass whole genome sequencing and STR analysis

DNA was extracted using QIAamp DNA Micro Kit (Qiagen). For low-pass WGS, libraries were produced using Illumina DNA Prep library prep kit and sequenced on Illumina HiSeq 4000 with paired 100 bp reads. After alignment, copy number estimation was performed using the QDNASeq package (Scheinin et al., 2014). Short Tandem Repeat (STR) profiling was obtained for each cell line with Promega PowerPlex16HS system and was compared back to any available commercial cell banks.

Antibody	Application	Product number	Experiment	Dilution used
4D2	Zebrafish rhodopsin staining	Abcam ab98887	Immunohistochemistry	1:200
1D4	Zebrafish red and green opsin staining	Abcam ab5417	Immunohistochemistry	1:200
Anti-blue opsin	Zebrafish blue opsin staining	Gifted by Prof. David Hyde (University of Notre Dame)	Immunohistochemistry	1:200
anti-Calnexin	ER marker	BD Biosciences 610524	Immunocytochemistry	1:100
anti-GFP	RDH12-GFP stable line staining	Abcam ab290	Immunocytochemistry	1:200
anti-OCT3/4	Pluripotency marker	Santa Cruz Biotechnology sc-5279	Immunocytochemistry	1:100
anti-SSEA3	Pluripotency marker	Millipore MC-631	Immunocytochemistry	1:50
anti-PAX6	Ectoderm marker	Biolegend 901302	Immunocytochemistry	1:300
anti-Vimentin	Mesoderm marker	Santa Cruz Biotechnology sc-6260	Immunocytochemistry	1:250
anti-AFP	Endoderm marker	Santa Cruz Biotechnology sc-51506	Immunocytochemistry	1:100
anti-RDH12	Detect purified RDH12	Proteintech 13289-3-AP	Western blot	
anti-RDH12	Detect RDH12 in stable cell line	Gift from Prof. Debra Thompson	Western blot	1:1000
anti-β-actin	Loading control	Sigma Aldrich A2228	Western blot	1:2000

Table 6: Antibodies used in this study.

Gene	Forward primer (5’-3’)	Reverse primer (5’-3’)	Reference
Zebrafish			
rdh12	GACTCCAGGGGTCGAATGTG	AGGTCTGAGCGCCTTCTTTC	
sod1	GGGCCAACCGATAGTGTGAG	TCATCCTCCTTCTCATGAATCACC	
sod2	CAAGGGACCACAGGTCTCATC	TGGAAACGCTCGCTGACATT	
cat	AGGGCAACTGGGATCTTACA	TTTATGGGACCAGACCTTG	(Wang et al., 2019)
gpx1	TGAGGCACAACAGTCAGGGA	CATTCTTGCAGTTCTCCTGGTGC	
hmox1a	CACAGAGACTGAGAGAGATTGGC	TGCCCACTCCTAATGCGAAC	
nrf2	ATGTCTAAAATGCAGCCAAGCC	CGGTAGCTGAAGTCGAACAC	(Nguyen et al., 2016)
atg5	CCCTACTATCTGCTCCTCCCAC	GGAGGTCGAACAACACACCA	
atg7	AGAGTCCAGTCCGATGTC	GAAGTAACAGCCGAGCG	
atg12	CCAGTTCATCTCACGCTTCCTC	TGCCGTCACTTCCGAAACAC	
p62	TTTGGCTCTTGTGAAGGATGAC	GAGGGCTAAAGTGAGGTGTAGTGA	
edem	CGTTTCGGTGCTCTTCCTGAG	GCGTAACCACACCTCACTTTG	(Park et al., 2020)
bip	CAAGAAGAAGACGGGCAAAG	CTCCTCAAACTTGGCTCTGG	(Park et al., 2020)
atf4	TGAGCACACTGAGGTTCCAG	GTCTTCACTCGGCCTTTGAG	(Park et al., 2020)
atf6	TGATGAGGCACTGTCTCCAG	ATGGGTCTTTTTGCTGGTTG	(Park et al., 2020)
chop	ATATACTGGGCTCCGACACG	GATGAGGTGTTCTCCGTGGT	(Park et al., 2020)
xbp1-s	TGTTGCGAGACAAGACGA	CCTGCACCTGCTGCGGACT	(Vacaru et al., 2014)
actin	CGAGCTGTCTTCCCATCCA	TCACCAACGTAGCTGTCTTTCTG	
Human			
ATF4	TCAAACCTCATGGGTTCTCC	GTGTCATCCAACGTGGTCAG	
CHOP	GACCTGCAAGAGGTCCTGTC	TGTGACCTCTGCTGGTTCTG	
sXBP1	CTGAGTCCGAATCAGGTGCAG	ATCCATGGGGAGATGTTCTGG	
GAPDH	ACAGTTGCCATGTAGACC	TTTTTGGTTGAGCACAGG	
NRF2	CAACTACTCCCAGGTTGCCC	AAGTGACTGAAACGTAGCCGA	
SOD2	GCTGGAAGCCATCAAACGTG	GCAGTGGAATAAGGCCTGTTG	
CAT	CTCCGGAACAACAGCCTTCT	GAATGCCCGCACCTGAGTAA	

GPX1	CCGGGACTACACCCAGATGA	TCTTGGCGTTCTCCTGATGC	
HO-1	CTCCTCTCGAGCGTCCTCAG	AAATCCTGGGGCATGCTGTC	
OCT3/4	CCCCAGGGCCCCATTTTGGTACC	ACCTCAGTTTGAATGCATGGGAGAGC	
KLF4	ACCCATCCTTCCTGCCCGATCAGA	TTGGTAATGGAGCGGCGGGACTTG	
SOX2	TTCACATGTCCCAGCACTACCAGA	TCACATGTGTGAGAGGGGCAGTGTGC	
L-MYC	GCGAACCCAAGACCCAGGCCTGCTCC	CAGGGGGTCTGCTCGCACCGTGATG	
LIN28	AGCCATATGGTAGCCTCATGCCGC	TCAATTCTGTGCCTCCGGGAGCAGGGTAGG	
OCT3/4 plasmid	CATTCAAACTGAGGTAAGGG	TAGCG AAAAGGAGCAACATAG	
KLF4 plasmid	CCACCTCGCCTTACACATGAAGA	TAGCGTAAAAGGAGCAACATAG	
SOX2 plasmid	TTCACATGTCCCAGCACTACCAGA	TTTGTTTGACAGGAGCGACAAT	
L-MYC plasmid	GGCTGAGAAGAGGATGGCTAC	TTTGTTTGACAGGAGCGACAAT	
LIN28 plasmid	AGCCATATGGTAGCCTCATGTCCGC	TAGCGTAAAAGGAGCAACATAG	
EBNA-1	ATCAGGGCCAAGACATAGAGATG	GCCAATGCAACTTGGACGTT	

Table 7: RT-qPCR primer sequences

3. RDH12 protein expression and purification

3.1. Aims

Retinol dehydrogenases belong to the short chain dehydrogenase/reductase (SDR) family of enzymes and are responsible for the interconversion between retinol and retinal. They have different stereospecificities depending on where they are expressed. RDH5, RDH10 and RDH11 are expressed in the RPE and oxidise 11-cis retinol to 11-cis retinal. RDH8 and RDH12 are expressed in the photoreceptors and reduce all-trans retinal to all-trans retinol. Mutations in *RDH12* are primarily associated with severe early onset LCA. There are currently no crystal structures available for any mammalian retinol dehydrogenase. The first aim of my project was to express and purify recombinant RDH12, and solve its structure using X-ray crystallography, in order to determine the effects of patient mutations on protein structure, and to aid drug design.

3.2. Results

3.2.1. Modelling of RDH12

As there are currently no crystal structures available for any mammalian retinol dehydrogenases, a predicted model of RDH12 was generated using the Phyre software, which builds a model based on homologs with known structures (Kelley et al., 2015). Using the “normal” mode, 236 out of 316 residues (40-290) were modelled with 100% confidence using isopiperitenone reductase from *Mentha piperita* in complex with

isopiperitenone and NADP as a template. The sequence was then resubmitted in the “intensive” mode, which creates a model based on multiple templates. Six templates were used to model RDH12, and 288 residues (91%) were modelled at >90% confidence (**Figure 8**). However, the first 28 residues did not align with any known structure, and were modelled by *ab initio*, and are therefore highly unreliable. RDH12 has two conserved regions, the catalytic site and cofactor binding site. The structure shows that the catalytic site, which has a conserved sequence of YXXXK, is part of an α-helix. The spacing of 3 residues between the catalytic residues tyrosine and lysine ensure they are facing each other. The cofactor binding site has a conserved sequence of GXXXGXG and is located between a β-strand and α-helix and the conserved glycines allow for this sharp turn.

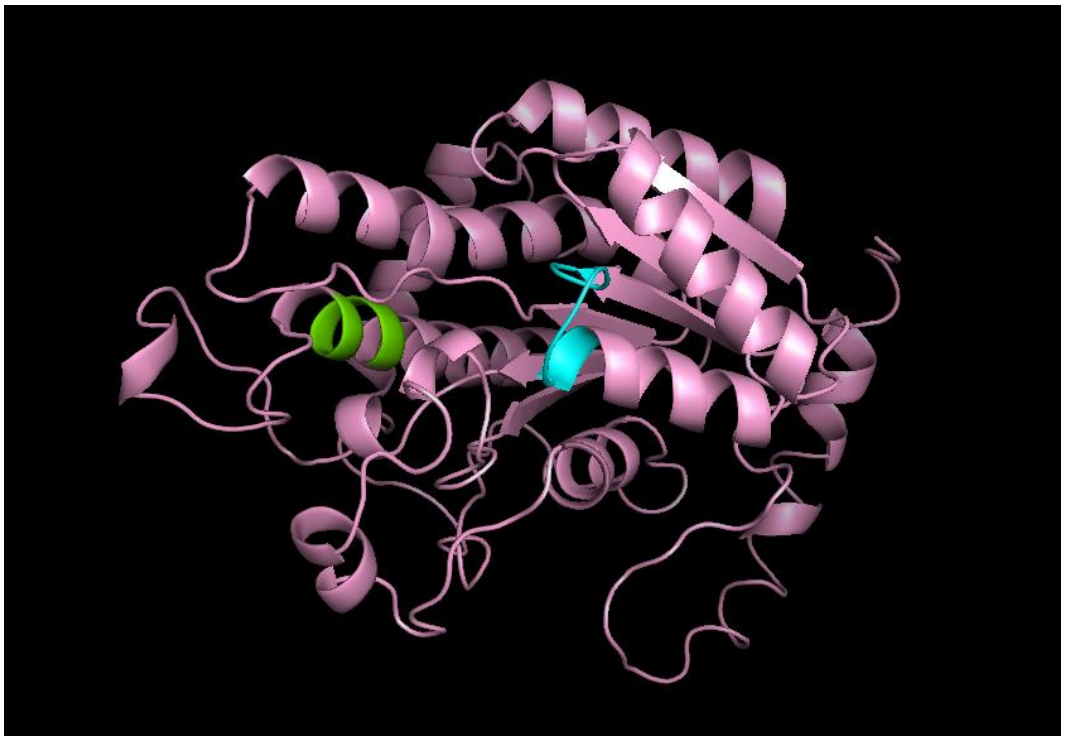

Figure 8: Predicted model of RDH12.
Model created using Phyre 2 software (Kelley et al., 2015). Active site shown in green and the cofactor binding site is shown in blue.

3.2.2. *E.coli* expression and purification

Full length RDH12 was cloned into two vectors: (i) pHT, which has an N-terminal 6xHis-tag (ii) pHLT, which has an N-terminal 6xHis-tag and a dihydrolipoyl dehydrogenase domain to increase protein solubility. According to the predicted model, the first ~30 residues do not align with any homologous proteins, so we predicted that this could act as a signal peptide, which is cleaved off following translation. Therefore, truncated RDH12 (31-316) was also cloned into the same two vectors.

In order to determine the optimum conditions for expression, small scale expression trails were carried out at various different conditions. Cultures (50 ml) were grown for 2 h, 4 h and overnight at 37 °C and overnight at 21 °C. Cells were harvested and purified using nickel resin. The 6xHis-tag has a high affinity for Ni^{2+} and binds to the nickel resin. Aliquots from the unbound and bound fractions were run on an SDS gel. Full length RDH12 was not expressed using the pHT vector. Use of the pHLT vector yielded expression of full length RDH12, although expression of the lipolyl domain alone was also observed, indicating that translation beyond the lipoly domain may not be efficient. pHT-RDH12 (31-316) yielded the highest expression at 21 °C overnight culture (**Figure 9**). A large scale expression under these conditions was carried out, and purified on a nickel column (**Figure 10**). Sample was then loaded onto an anion exchange column in low salt buffer, washed and eluted in high salt buffer. The theoretical isoelectric point (pI) of RDH12 is 9.65. At pH 8, RDH12 will carry a positive charge, and therefore will not bind to the anion column and should be present in the flow through. RDH12 was

present in the flow through, at a reasonably high level of purity (**Figure 11**). In order to determine the monomeric state of RDH12, the sample was then loaded on to an S200 gel filtration column. According to the S200 calibration, RDH12, which is 35 kDa, should elute at 85 ml. The sample however eluted in the void volume (V_0), suggesting that RDH12 is aggregated. In order to determine at what stage RDH12 is aggregating, following nickel column purification, sample was loaded directly on to the S200 column. The glycerol content of the buffer was also increased to 20%, to prevent aggregation, however, most of the sample again eluted in the void volume (**Figure 12**).

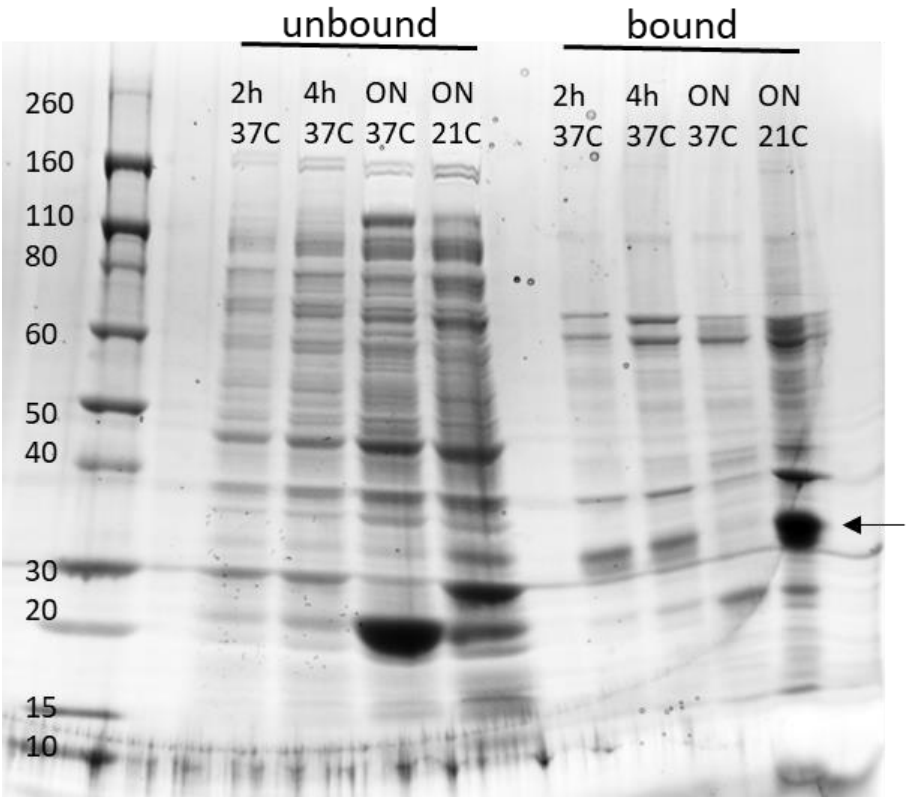

Figure 9: pHT-RDH12 (31-316) expression trials.
Cultures were grown under various conditions and purified using Nickel resin. Unbound and bound fractions were run on an SDS gel. The molecular weight of RDH12 (31-316) is 35 kDa and is indicated by the arrow. Highest expression was observed at 21 °C overnight (ON) culture.

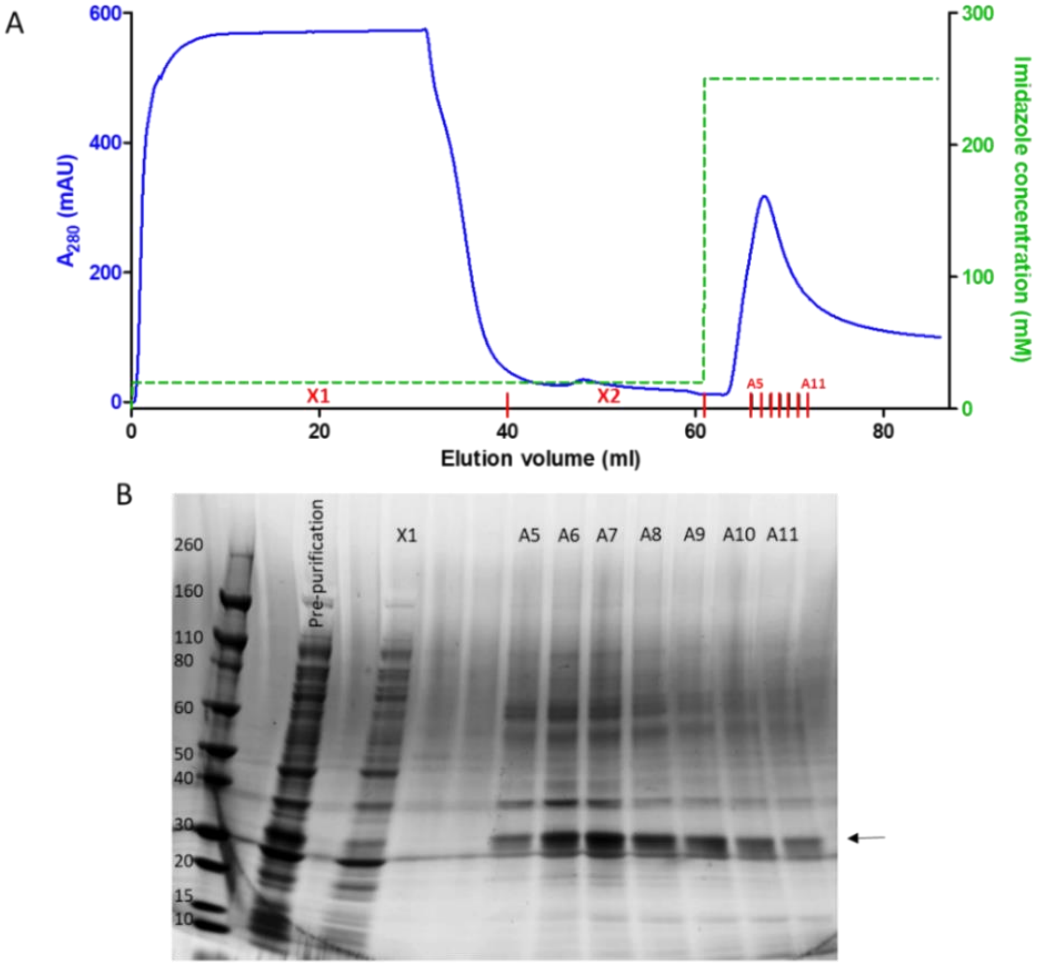

Figure 10: pHT-RDH12 (31-316) Nickel column purification.
(A) Bacterial pellet from a 1 L overnight culture at 21 °C was lysed and loaded onto a 5ml nickel column and eluted in high imidazole buffer, using the AKTA purifier system. Absorbance at 280 nm is shown in blue, imidazole concentration of the buffer is shown in green, and collected fractions are shown in red. **(B)** SDS-PAGE gel of fractions from (A), bands representing RDH12 is indicated by arrow.

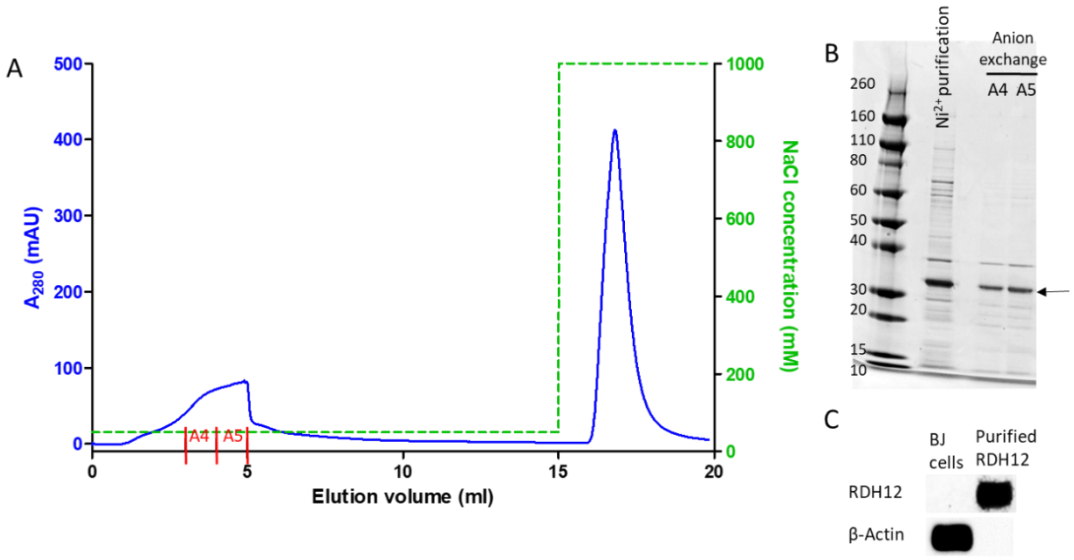

Figure 11: Anion exchange purification.
(A) Fractions containing RDH12 were loaded onto a 1 ml anion exchange column for further purification. Absorbance at 280 nm is shown in blue, NaCl concentration of the buffer is shown in green, and collected fractions are shown in red. **(B)** SDS-PAGE gel of fractions in (A). RDH12 was obtained at approximately 90% purity level. RDH12 is indicated by arrow. **(C)** Western blot using anti-RDH12 (Proteintech 1:500), confirmed expression of purified RDH12. Human fibroblast BJ cells, which do not express RDH12, were used as a negative control.

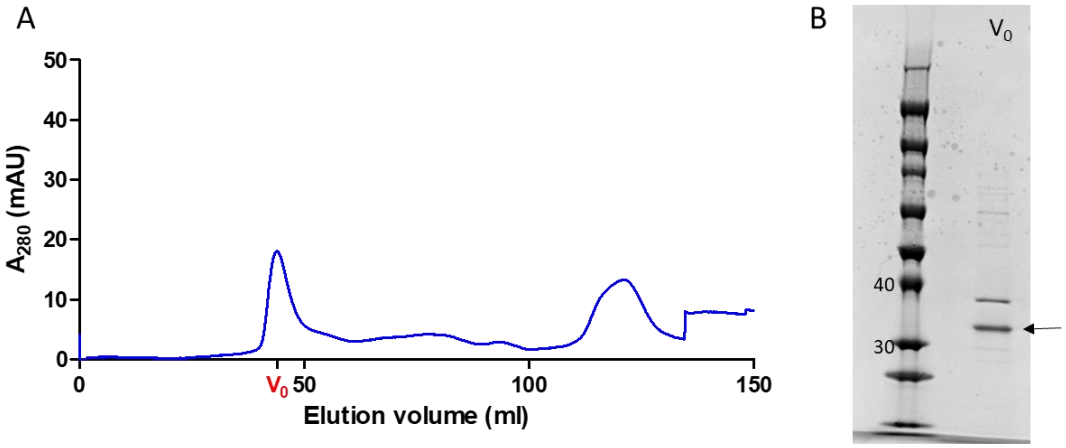

Figure 12: Size exclusion chromatography of RDH12.
(A) Following nickel column purification, sample was directly loaded onto a 120 ml S200 size exclusion column. Fraction containing the void volume (V^0) is labelled **(B)** SDS-PAGE gel of V_0 fraction. RDH12 (showed by arrow) eluted in void volume, indicating that RDH12 protein is aggregated.

As expression of the pHT-RDH12 (31-316) construct resulted in aggregation, I created two constructs with different N-terminal truncations. Running the RDH12 sequence through the signal peptide predictor, Signal P, predicted the first 20 residues to be a signal peptide, with a possible cleavage site between 20 and 21. The RDH12 predicted model shows that the N-terminus is helical followed by a short unstructured region up to residue 38. This is also the position from which the human RDH12 sequence correlates with *D.melanogaster* photoreceptor dehydrogenase (PDH), which has been crystallised. Therefore, RDH12 (21-316) and (39-316) constructs were generated.

RDH12 (21-316) has an estimated molecular weight of 33 kDa and RDH12 (39-316) has an estimated molecular weight of 31 kDa. Small scale expression trials were carried out for both constructs in both vectors. pHT-RDH12 (21-316) overnight at 21 °C gave the highest expression for this construct. pHT-RDH12 (39-316) expression for 4 h at 37 °C, and pHLT-RDH12 (39-316) for 2 h at 37 °C also gave good expression. Western blot analysis was carried out for conditions that appeared to have high expression levels. Expression of RDH12 was not detected for some conditions, but those with confirmed expression showed a single band for RDH12, confirming that the protein is not degraded (**Figure 13**). Large scale expressions of select conditions, that showed RDH12 expression, were carried out. In all conditions tested, RDH12 aggregated and eluted in the void volume.

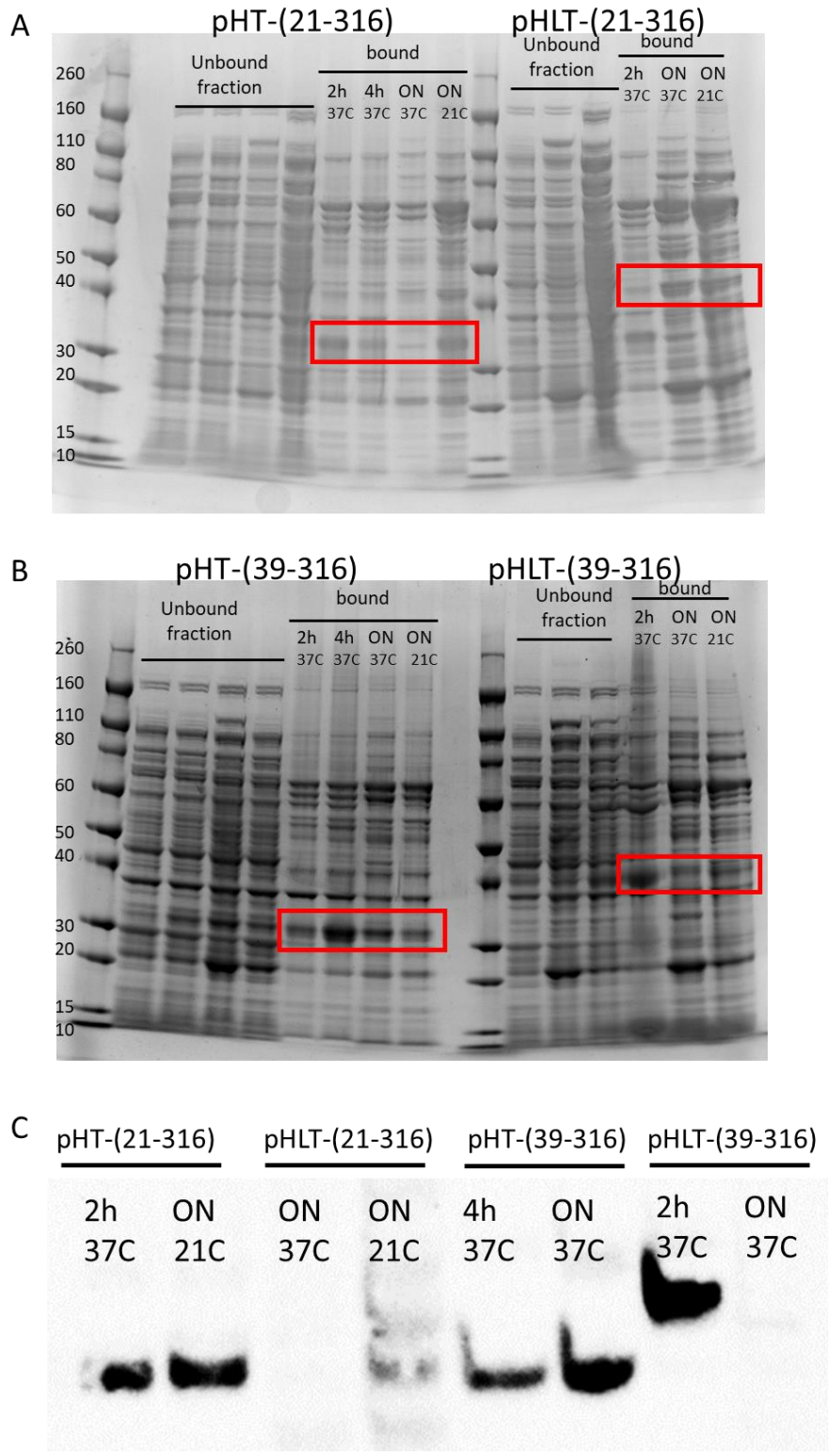

Figure 13: RDH12 (21-316) and RDH12 (39-316) expression trials.
(A) RDH12 (21-316) and **(B)** RDH12 (39-316) in pHT and pHLT vectors were expressed under various conditions and purified using nickel resin. Unbound and bound fractions were run on SDS gel. Bands of expected size of RDH12 are shown in red box. **(C)** Western blot analysis confirming RDH12 expression.

In order to determine if the N-terminal 6xHis tag is interfering with the signal peptide function, and therefore causing protein to be mislocalised and misfolded, full length RDH12 was subcloned into the pOPINE vector which has a C-terminal 6xHis tag. A small scale expression was carried out under various conditions. As shown in **Figure 14A**, there is strong expression of a protein at 20 kDa; however, this does not correspond with the molecular weight of RDH12, which is estimated to be 35 kDa. To confirm if RDH12 is being expressed, a western blot was carried out. No bands were detected for RDH12 at 2 h, 4 h or overnight expression at 37 °C. However, multiple bands were detected for RDH12 with overnight expression at 21 °C, suggesting that RDH12 is expressed but degraded (**Figure 14B**).

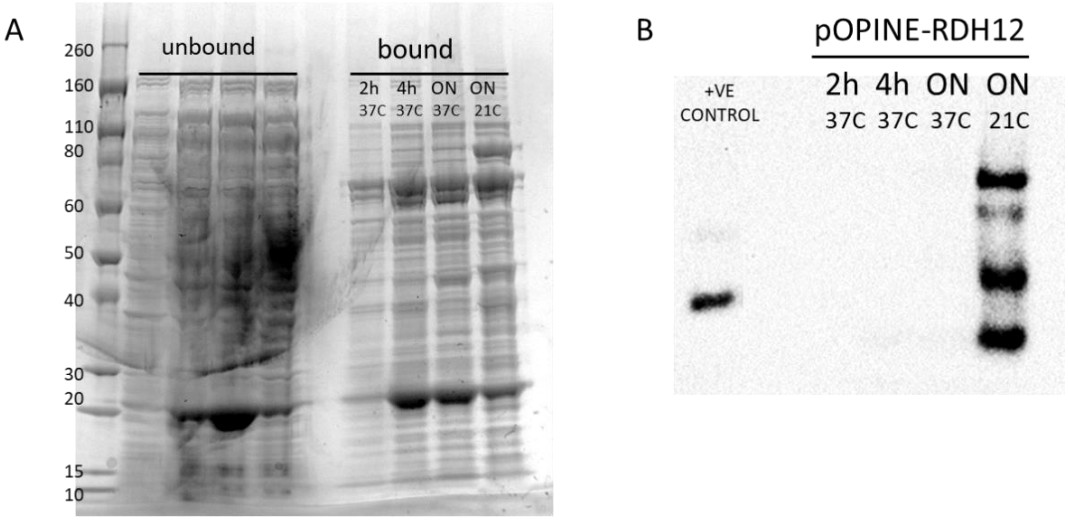

Figure 14: Small scale expression of pOPINE-RDH12.
(A) Full length RDH12 with a C-terminal 6xHis tag (pOPINE-RDH12) was expressed under various conditions and purified using nickel resin. Unbound and bound fractions were run on an SDS gel. **(B)** Western blot showed no expression for pOPINE-RDH12 expressed at 2 h, 4h or overnight at 37 °C, however multiple bands were observed with overnight expression at 21 °C, suggesting degradation of the protein (pHT-RDH12 (39-316) was used as a positive control).

With all constructs, following nickel purification, many bands are still seen on the gel, however, western blot confirms only one band for RDH12, corresponding to the correct molecular weight. Therefore, a different protein was expressed in the same vector and purified with nickel resin. As shown in **Figure 15**, purification of the B domain of protein A in the pHLT expression vector resulted in a significantly cleaner gel, with only two dominant bands, one at 15 kDa corresponding to the lipoyl domain only and one at 40 kDa for the over expressed protein bound to lipoyl domain. This suggests that RDH12 is interacting with *E.coli* proteins, possibly chaperones to aid in folding.

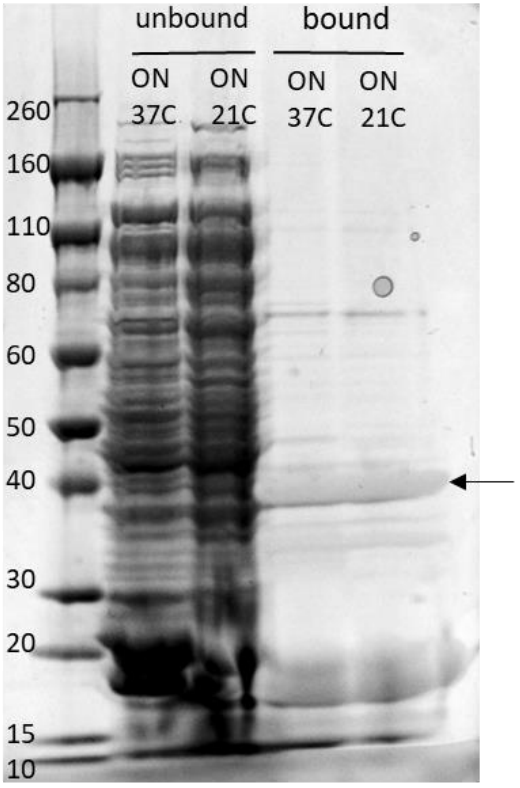

Figure 15: Purification of B domain of protein A.
SDS-PAGE gel of purification, using nickel resin, of the B domain of protein A expressed in pHLT vector. Band corresponding to the protein is shown by an arrow.

Following multiple attempts at purification of RDH12 and many optimisation steps, all attempts resulted in aggregated protein, suggesting misfolding of the protein, further attempts at purification of RDH12 in *E.coli* were therefore stopped.

3.2.3. Mammalian expression and purification

As difficulties were encountered with the *E.coli* expression system, an alternative host organism was tested. To test a mammalian expression system, human Expi293 cells were transfected with a vector encoding RDH12 with a C-terminal 6xHis-tag (p.Receiver-M77.RDH12). Following sonication and centrifugation, pellet was resuspended in buffer with 15 mM detergent, DHPC, to aid solubilisation. Sample was then purified on Nickel beads. Aliquots were sampled following each step of the purification process and western blot, probing for RDH12, was carried out to determine if the purification method was efficient. As shown in **Figure 16**, RDH12 is successfully expressed, however protein is lost at each stage of the purification process. In particular, following the second centrifugation, a large amount of RDH12 protein still remains in the pellet, indicating inefficient purification and a low final yield. Combined with the lack of improvement in purification and loss of the protein in pellets this approach was stopped.

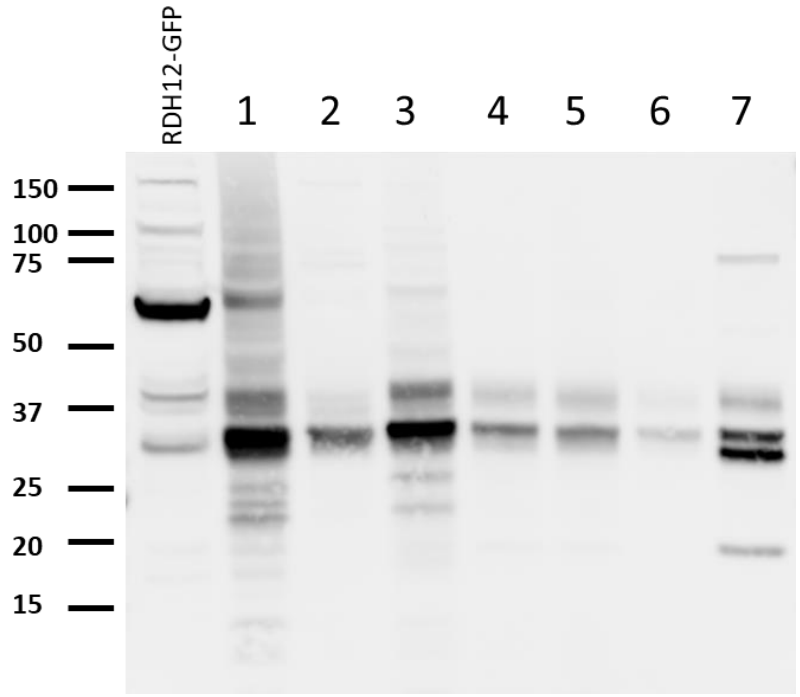

Figure 16: Purification of RDH12-His from mammalian cells.
Pellet was resuspended in buffer, sonicated (1), centrifuged, supernatant was collected (2) and centrifuged again. Pellet was resuspended in buffer containing DHPC (3) and centrifuged. Supernatant collected (4) and loaded onto nickel beads (5), washed (6) and eluted (7). Samples were collected at each stage (labelled 1 to 7) and western blot was carried out. A stable HEK293 cell line expressing RDH12 with a GFP tag was used as a positive control.

3.3. Discussion

In this chapter, I attempted expression and purification of RDH12 in two systems, *E.coli* and human cells. Following multiple optimisations steps, all attempts resulted in aggregation of the protein or low yields, insufficient for crystallography studies. Therefore, this aspect of the project was halted.

However, possible experimental avenues for proteins that are incorrectly folded, include co-expressing with chaperones to aid protein folding and expressing at a lower temperature, to slow down folding kinetics. RDH12 contains 8 cysteine residues. Proteins that are cysteine rich can form incorrect disulphide bonds, leading to misfolding and aggregation. In the reducing environment of the cytoplasm, disulphide bonds are likely to not form or form erroneously. The addition of a signal peptide directing the protein to the periplasm, which has an oxidising environment, may aid in the formation of correct disulphide bonds and folding of the protein, or special strains of *E.coli* designed for disulphide bond formations can be used. Insolubility of the protein can also cause aggregation; the protein can be fused to a fusion protein that enhances solubility, for example a GST, MBP or SUMO tag (Francis and Page, 2010). RDH12 localises to the ER and faces the cytosolic side of the ER membrane and is thought to be membrane associated (Lee et al., 2007, Keller and Adamski, 2007), with membrane proteins traditionally harder to purify and often resulting in aggregation. Detergents can be added to the buffer to extract and solubilise the protein, although detergents are not always compatible with purification methods (Abarghooi Kahaki et al., 2020).

A promising alternative to an *in vivo* system is cell free protein synthesis, which utilises cell lysates containing all the necessary components required for protein synthesis, without the constraints of a cell membrane. Cell free systems derived from eukaryotic cells, like Chinese hamster ovary cells, contain endogenous microsomes which are particularly useful for the production of membrane proteins, as they provide a native environment and necessary machinery for proper folding and post translational modifications, without the risk of cellular toxicity often caused by membrane protein production in traditional *in vivo* systems (Dondapati et al., 2020).

No mammalian retinol dehydrogenase structures have been solved to date. Additionally, in the paper by Hofmann et al. (2016), the authors state that they experienced difficulties in obtaining any vertebrate retinol dehydrogenases for structural biology approaches, hence they moved onto the invertebrate retinol dehydrogenase, *d.melanogastor* PDH. This further indicates that these proteins may be inherently difficult to express and purify.

Recently, DeepMind AlphaFold, a program that utilises artificial intelligence to predict the protein structure of almost all human proteins with high accuracy, has been released (Tunyasuvunakool et al., 2021). The structure of RDH12 has been predicted mostly with a ‘very high’ confidence level, however, similar to my model generated earlier, the first few residues are predicted with ‘low’ confidence. In addition, residues 240-253 are also predicted with low confidence. These low confidence regions may be

unstructured or represent sites of dimerization or interaction with other proteins. Nonetheless, this model provides a useful tool to study RDH12 protein structure and the effects of patient mutations.

4. Generation of *rdh12* mutant zebrafish using CRISPR/Cas9 gene editing

4.1. Aims

Two *Rdh12* knockout mouse models have been previously generated, however both displayed a relatively mild phenotype, with normal retinal histology and no apparent signs of retinal degeneration (Kurth et al., 2007, Maeda et al., 2006). As the knockout *Rdh12* mouse models do not recapitulate the severe phenotype observed in patients, study of disease mechanisms remains a challenge. Zebrafish are a useful tool for the study of genetic diseases, as they share 70% of their genome with humans and are easily manipulated by gene editing. The aim of this chapter was to generate a *rdh12* zebrafish model using CRISPR/Cas9 gene editing and characterise the retinal phenotype in order to study the disease mechanisms.

4.2. Results

Part of the work described in this chapter was carried out by Dr Maria Toms, in particular embryo injections, confirmation of mutations, raising of fish and breeding to generate mutant fish line. In addition, all maintenance, breeding, culling and dissections of fish were carried out by Dr Maria Toms.

4.2.1. Rdh12 homology in zebrafish

Many human genes have two zebrafish orthologues, due to an additional round of genome duplication, however *rdh12* is not duplicated and zebrafish

only have one *rdh12* gene. Human *RDH12* contains 7 exons and encodes a 316 amino acid protein, while zebrafish *rdh12* has 7 exons and encodes a 319 amino acid protein. Alignment of human and zebrafish rdh12 amino acid sequences using NCBI BLASTP reveal they share 64% sequence homology, including at the cofactor binding and active sites, indicating high conservation between the species. Alignment of the sequences using BoxShade is shown in **Figure 17**.

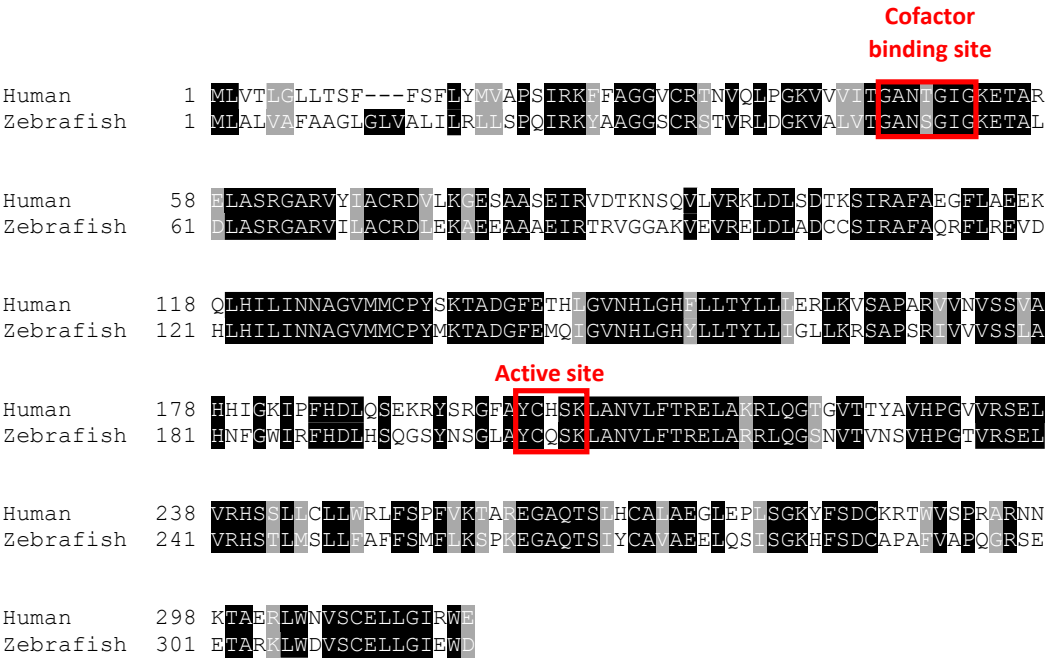

Figure 17: Alignment of human and zebrafish rdh12 protein sequences

4.2.2. Generation of *rdh12* zebrafish

CRISPR/Cas9 gene editing was used to generate *rdh12* mutant zebrafish. In order to create a null mutant, an introduction of an indel mutation early in the coding sequence is required. Therefore, a sgRNA targeting a sequence in exon 1 was designed. Single stranded gene specific and constant oligonucleotides were annealed to create a dsDNA template, which was transcribed *in vitro* to create the sgRNA (**Figure 18A**). To create Cas9 mRNA, the Cas9 plasmid was linearised, transcribed and a poly(A) tail

added. Embryos were co-injected with Cas9 mRNA and sgRNA and collected at 24 hpf. DNA was extracted and analysed by Sanger sequencing. This confirmed that the sgRNA was effective at generating mutations at the target site in exon 1 (**Figure 18B**). Embryos were raised to adulthood (F0) and crossed with wildtype fish to produce the F1 generation. DNA extracted from pooled embryos were analysed for germline mutations by Sanger sequencing. Mutations carried by F1 fish included several frameshift mutations. Fish carrying the 7 bp deletion c.17_23del; p.(Val6AlafsTer5) were chosen to raise to adulthood and establish a mutant line, because the mutation is predicted to cause a frameshift and premature termination in exon 1. This line was named *rdh12*^{u533} (**Figure 18C**).

Fish were raised to adulthood and those carrying heterozygous mutations were crossed with wildtype fish to generate the F2 generation and minimise off-target effects. F2 generation were grown to adulthood and heterozygous fish carrying the same mutation were in-crossed to create the F3 generation. Once they reached maturity, homozygous fish were then crossed to produce the F4 generation, for which 100% of the progeny were homozygous for the mutation.

Expression of *rdh12* mRNA transcript was assessed in *rdh12*^{u533} homozygous larvae and found to be significantly reduced to 45%, compared to wt (p=0.0087), suggesting nonsense mediated decay (**Figure 18D**). However, if translated, the protein would only be 10 amino acids long and lack any functional domains. Knockout of the protein could not be confirmed

due to lack of available zebrafish specific antibody, however predicted truncation would suggest a null mutant.

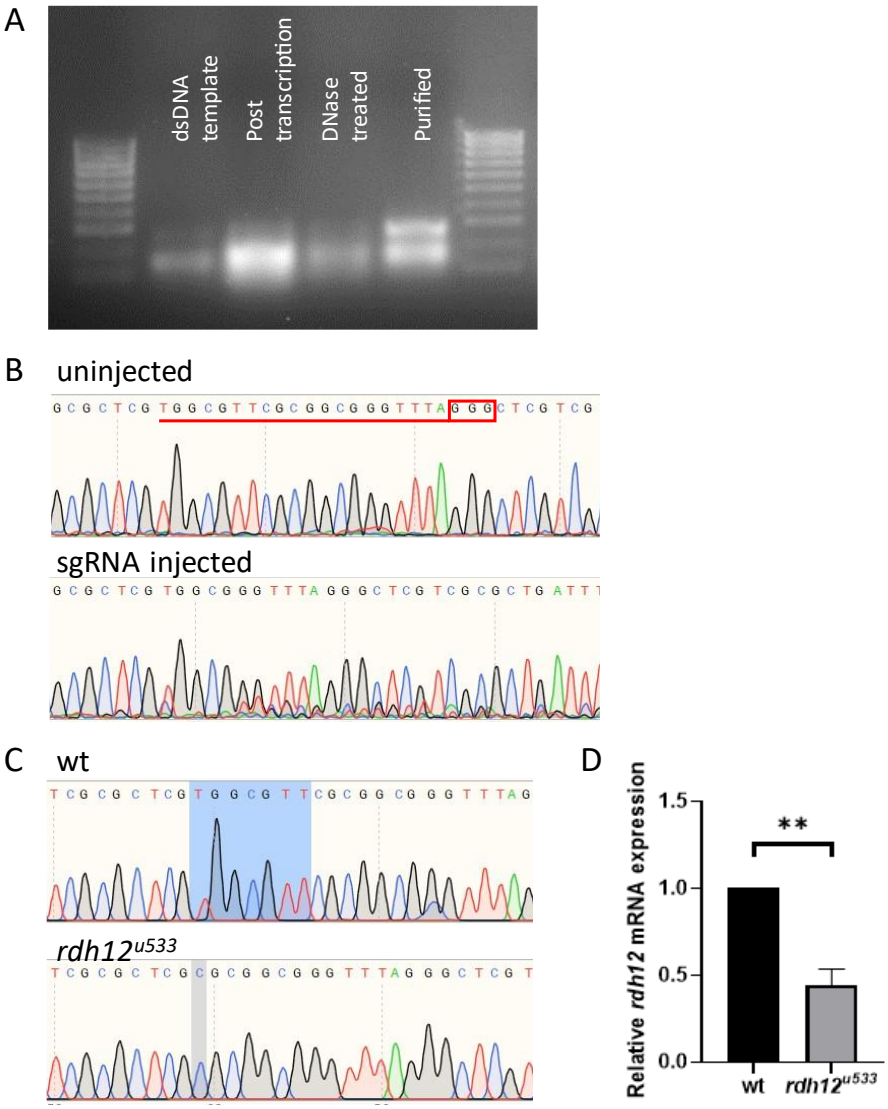

Figure 18: Generation of *rdh12*^{u533} mutant fish using CRISPR/Cas9 gene editing.
(A) *rdh12* single stranded oligonucleotide and constant oligonucleotide were annealed to create the dsDNA templates. The dsDNA template was transcribed, DNase treated and purified to create the sgRNAs. **(B)** Embryos were co-injected with Cas9 mRNA and sgRNA, collected at 24 hpf and DNA analysed by Sanger sequencing. sgRNA was effective at generating mutations at the target site (underlined in red) and PAM site (red box). **(C)** Sanger sequencing traces showed a 7 bp deletion (c.17_23del) in the *rdh12*^{u533} mutant fish. The deleted bases are highlighted in blue on the wildtype trace. **(D)** RT-qPCR showed a significant reduction of *rdh12* mRNA expression in the *rdh12*^{u533} fish at 5 dpf (**p ≤ 0.001 analysed by paired t-test).

4.2.3. Characterisation of *rdh12^{u533}* embryos

rdh12^{u533} zebrafish were comparable to wt fish at 5 dpf in morphology and size, with normal development. Eyes were of normal size and shape. Retinal histology revealed normal morphology and lamination of retinal layers (**Figure 19A**). Rhodopsin was labelled using the 4D2 antibody, which localised rhodopsin to the rod outer segments in both wt and *rdh12^{u533}* fish (**Figure 19B**). Apoptosis was analysed using TUNEL assay on retinal sections. The choroideremia (chm) zebrafish model shows a severe retinal degenerative phenotype (Moosajee et al., 2009), and was used as a positive control for apoptosis. TUNEL assay showed widespread positive staining for apoptotic nuclei in the *chm* fish at 5 dpf. No apoptotic nuclei were detected in the wt or *rdh12^{u533}* fish at 5 dpf (**Figure 20**). Retinoids were extracted from whole embryos and atRAL levels were analysed by HPLC, but there was no significant difference between wt and *rdh12^{u533}* (**Figure 21A**). Oxidative stress was investigated in embryos through analysis of antioxidant activity. SOD is the first line of defence antioxidant enzyme that dismutates superoxide anions to hydrogen peroxide. No difference in SOD activity was found between the wt and *rdh12^{u533}* embryos at 5 dpf (**Figure 21B**).

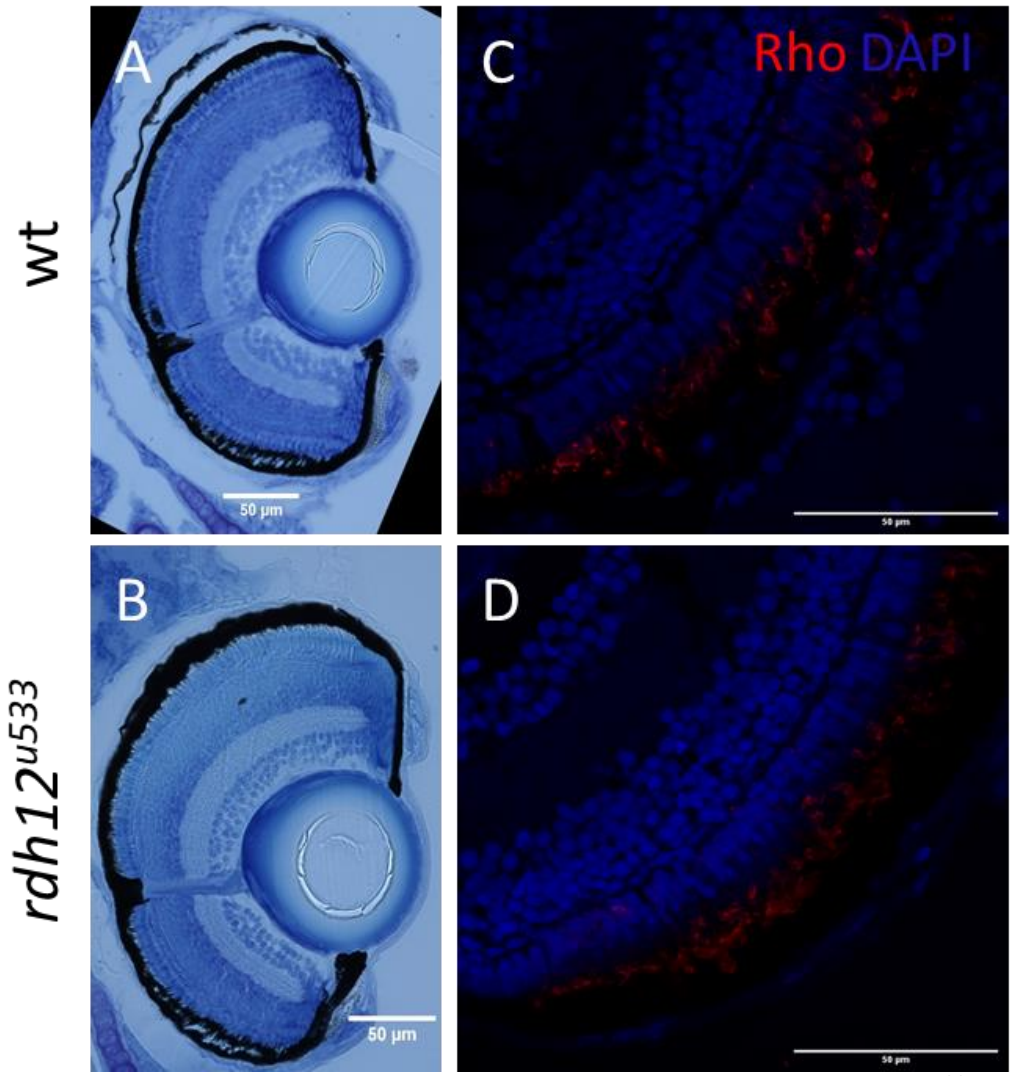

Figure 19: Retinal histology and rhodopsin localisation in *rdh12*^{u533} embryos.
(A, B) Retinal sections from fish at 5 dpf were stained with toluidine blue to assess retinal structure. **(C, D)** Immunohistochemistry staining was used to detect rhodopsin. No differences were found between the wt and *rdh12*^{u533} fish. Scale bar = 50 µm.

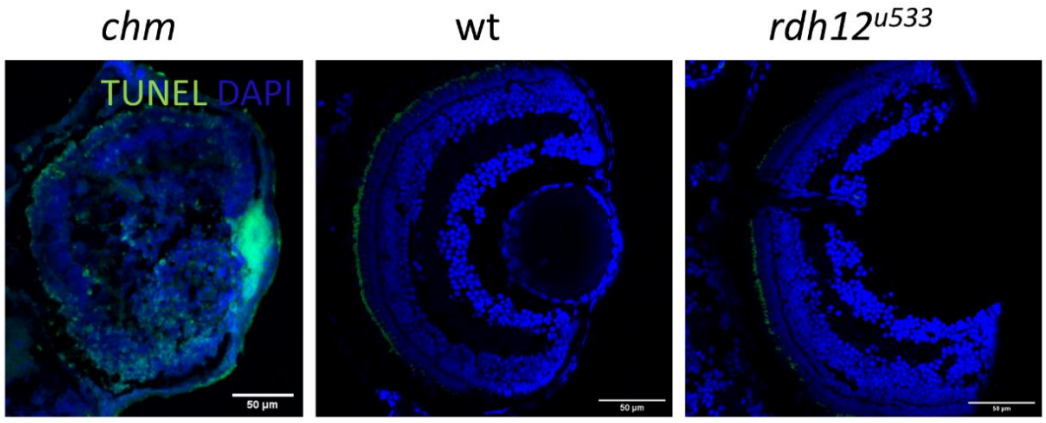

Figure 20: Analysis of apoptosis in *rdh12^{u533}* embryos.
TUNEL assay was used to detect cell death in the retinas of 5 dpf fish. Choroideremia (*chm*) fish show widespread retinal degeneration and were used as a positive control for cell death. No cell death was detected in the wt and *rdh12^{u533}* fish at 5 dpf. Scale bar = 50 µm.

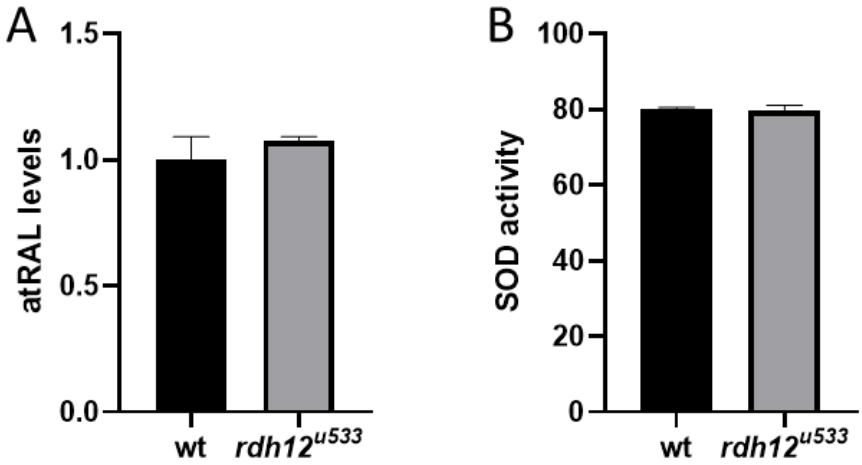

Figure 21: Analysis of oxidative stress in *rdh12^{u533}* embryos.
(A) atRAL levels in whole embryos were analysed by HPLC. Approximately 250 embryos were used per replicate. **(B)** SOD activity was quantified in fish at 5 dpf. Twenty embryos were used per replicate. No differences between wt and r*dh12^{u533}* fish were detected at 5 dpf. Three independent experiments were carried out. Data are displayed as mean ± SEM.

4.2.4. Characterisation of *rdh12^{u533}* adult zebrafish

Adult *rdh12^{u533}* fish were viable and fertile. Morphology and development was comparable to wt fish. At 12 months post fertilisation (12 mpf), retinal histology (**Figure 22A-B**) and TUNEL assay (**Figure 22C-D**) in the *rdh12^{u533}* fish were akin to wt controls. However, rhodopsin was mislocalised to the photoreceptor inner segments and outer nuclear layer in the *rdh12^{u533}* in some areas of the retina (**Figure 22E-F**). Using the 1D4 antibody, which detects red and green opsin in zebrafish, staining was detected in the outer segments and was similar in intensity and location between the wt and *rdh12^{u533}* fish (**Figure 22G-H**). There was also no difference in blue opsin staining between wt and *rdh12^{u533}* fish (**Figure 22I-J**).

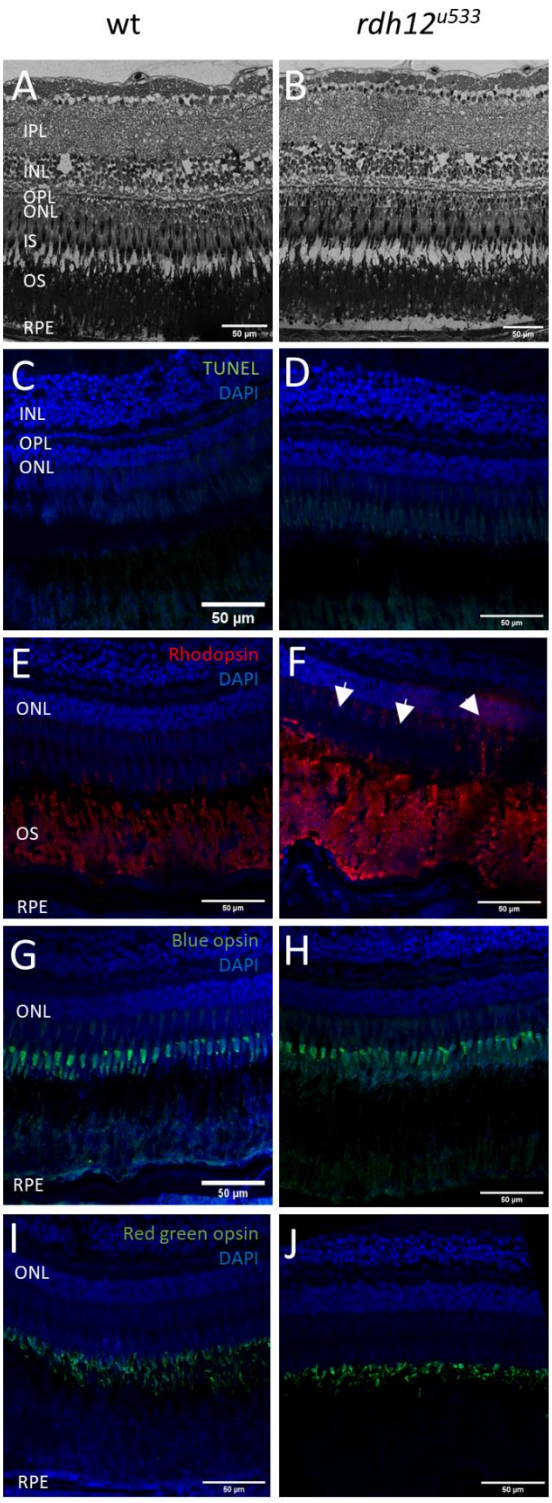

Figure 22: Characterisation of adult *rdh12*^{u533} zebrafish.
(A,B) Retinal sections from 12 mpf fish were stained with toluidine blue to assess retinal structure. **(C,D)**TUNEL assay revealed no cell death. Immunohistochemistry staining was used to detect **(E,F)** rhodopsin, **(G,H)** blue opsin and **(I,J)** red/green opsin. Rhodopsin mislocalisation was observed in *rdh12*^{u533} fish. IPL, inner plexiform layer; INL, inner nuclear layer; OPL, outer plexiform layer; ONL, outer nuclear layer; IS, inner segment; OS, outer segment; RPE, retinal pigment epithelium. Scale bar = 50 µm.

Retinal ultrastructure of fish at 12 mpf was examined using transmission electron microscopy (TEM). The organisation of retina and organelles appeared largely similar between the wt and *rdh12*^{u533} fish. The photoreceptors looked comparable to wt, with similar length and normal morphology of the outer segments and the inner segments contained similar numbers of mitochondria (**Figure 23**). Phagosomes, which are vesicles containing shed photoreceptor outer segments, were observed in the RPE (**Figure 23B and D**). The number of phagosomes per length of RPE was quantified, but there was no significant difference between wt and *rdh12*^{u533} (**Figure 23E**). The area of each phagosome was determined using ImageJ and a significant increase in the size of phagosomes in the mutant RPE was found (p=0.0001) (**Figure 23F**). The average size of wt phagosomes were 2.1 μm^2, whereas phagosomes in *rdh12*^{u533} RPE were almost double in size with an average size of 4.1 μm^2.

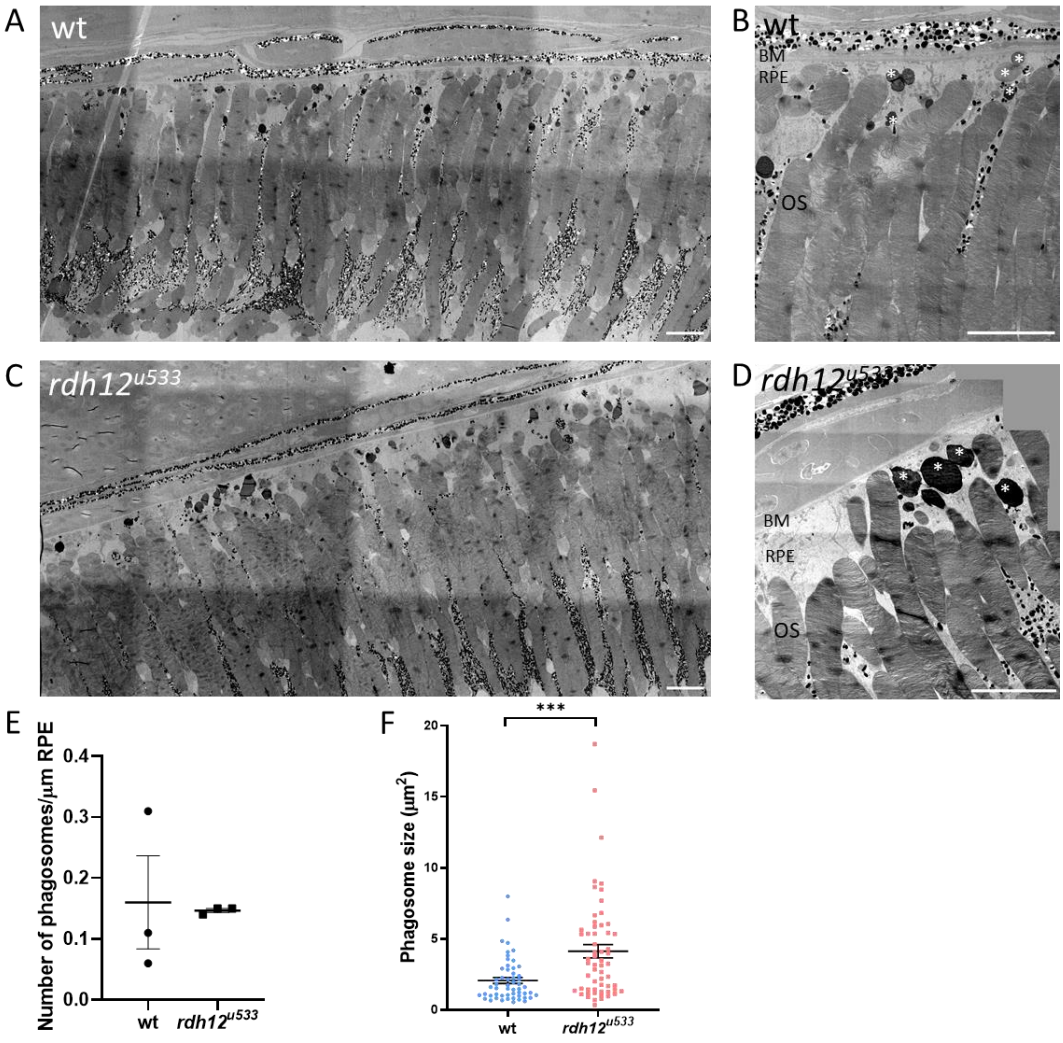

Figure 23: Retinal ultrastructure of adult wt and *rdh12*^{u533} fish. Transmission electron microscopy was used to assess retinal ultrastructure of **(A,B)** wt and **(C,D)** *rdh12*^{u533} fish at 12 mpf. Phagosomes are indicated with white asterisks. Scale bar = 50 µm. **(E)** No significant difference was noted in the number of phagosomes between wt and *rdh12*^{u533} fish. **(F)** Phagosomes were significantly larger in the *rdh12*^{u533} fish at 12 mpf. Data are displayed as mean ± SEM. Phagosome number and size was quantified using ImageJ from three wt and *rdh12*^{u533} fish. Statistical significance was analysed by Mann-Whitney, ***p ≤ 0.001. OS, outer segment; RPE, retinal pigment epithelium; BM, Bruch's membrane.

Autophagy is the process of degradation of cellular components, such as damaged organelles, proteins and lipids, via lysosomes. The autophagy pathway was examined through analysis of autophagy markers by RT-qPCR (**Figure 24**). Expression of autophagy markers *atg5*, *atg7*, *atg12* and *p62* was reduced in the *rdh12*^{u533} fish, with *atg12* significantly reduced by 1.9-fold compared to the wt fish (p=0.0038).

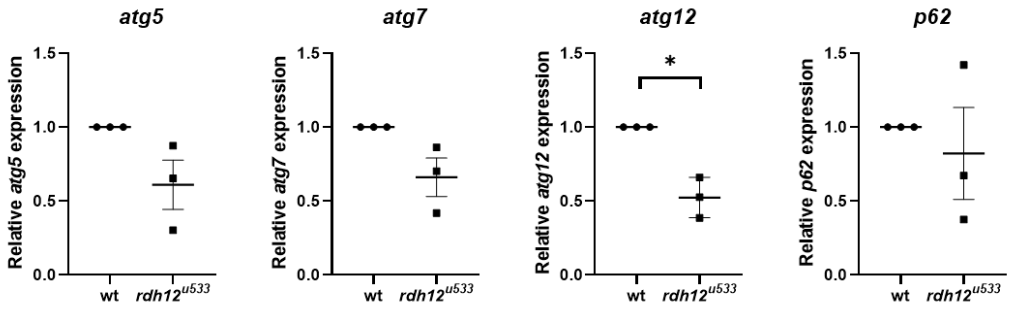

Figure 24: Expression of autophagy markers are reduced in *rdh12*^{u533} retina.
mRNA expression of autophagy genes in the retina of 12 mpf fish were analysed by RT-qPCR. Expression of *atg12* was significantly reduced in the *rdh12* ^{u533} mutant fish. *p < 0.05.

The oxidative stress and ER stress pathways were investigated in adult zebrafish. Oxidative stress is a result of an imbalance between reactive oxygen species (ROS) and antioxidant levels. Under mild stress, antioxidant enzymes scavenge ROS to maintain homeostasis in the cell. However, if ROS levels become too high, cellular homeostasis is disrupted and antioxidant enzymes become overwhelmed as they cannot cope with the high ROS load (Rahman, 2007). The mRNA expression of *nrf2*, a key transcription factor that regulates the cells response to oxidative stress, was analysed. No significant difference was found in the *rdh12*^{u533} fish, compared to wt (**Figure 25**). Overall, no significant differences were found in

expression of genes encoding antioxidant enzymes sod1, cat, gpx1 and hmox1. However, *sod2* was significantly reduced by 2.2-fold (p=0.0085) at 12 mpf in the *rdh12*^{u533} fish (**Figure 25**). ER stress occurs when homeostasis of the ER is disrupted, for example by an increase in ROS and calcium levels, mutant proteins or autophagy, leading to an accumulation of misfolded proteins in the ER (Adams et al., 2019). No significant difference in expression of ER stress markers at 12 mpf was observed between the wt and *rdh12*^{u533} fish (**Figure 26**). HPLC analysis of atRAL levels in the 16 mpf retinas revealed no significant difference between the wt and *rdh12*^{u533} fish (**Figure 27A**). The activity of antioxidant enzymes, SOD and CAT, were quantified in retinas from 16 mpf fish however no significant difference was found between wt and *rdh12*^{u533} (**Figure 27B-C**).

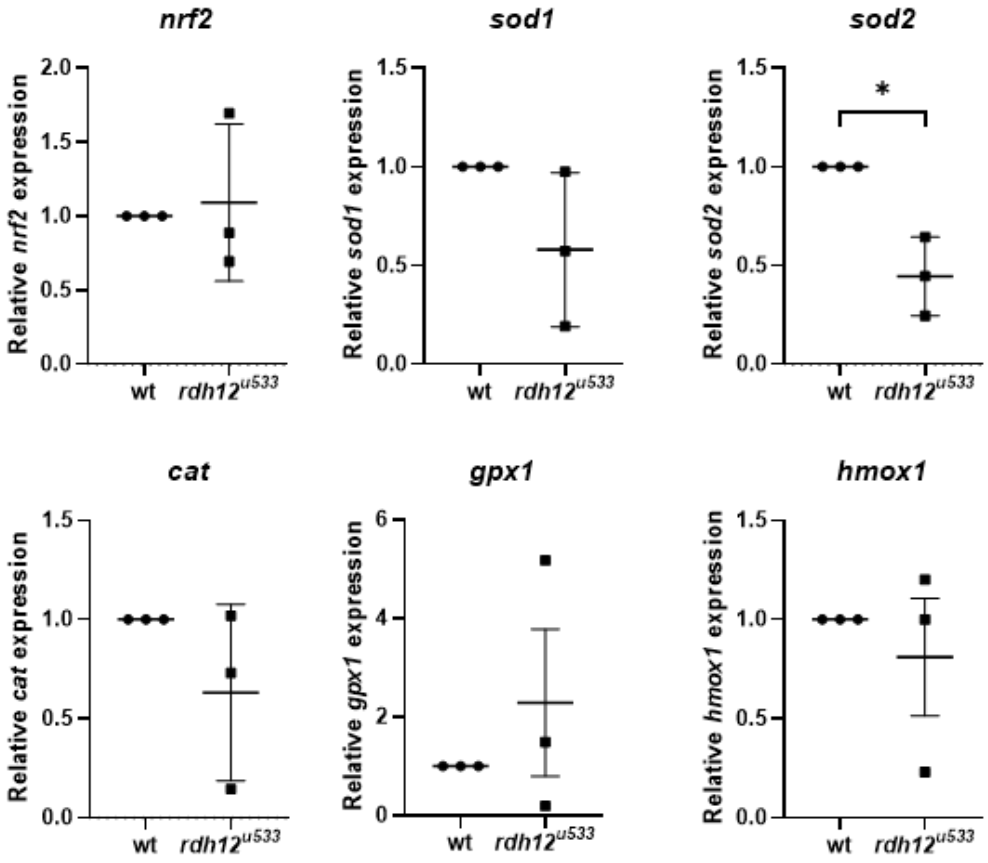

Figure 25: Analysis of oxidative stress in adult *rdh12*^{u533} retina.
Expression of oxidative stress markers were analysed by RT-qPCR in retinas from wt and *rdh12* fish at 12mpf. mRNA expression of *sod2* was significantly reduced in *rdh12* mutant fish retinas. Data are expressed as mean ± SEM. *p < 0.05.

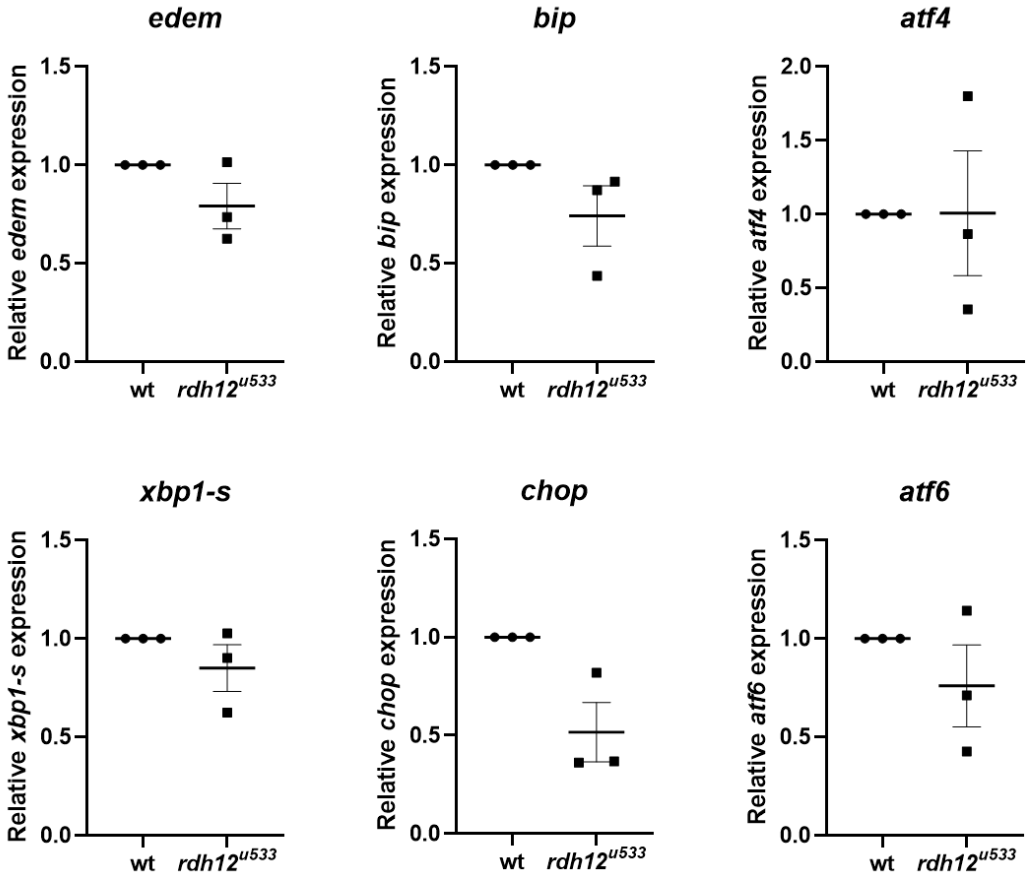

Figure 26: ER stress is not disrupted in *rdh12*^{u533} fish.
Expression of ER stress markers were analysed by RT-qPCR in 12 mpf retinas. No significant differences in expression between wt and *rdh12*^{u533} fish was seen. Data are expressed as mean ± SEM.

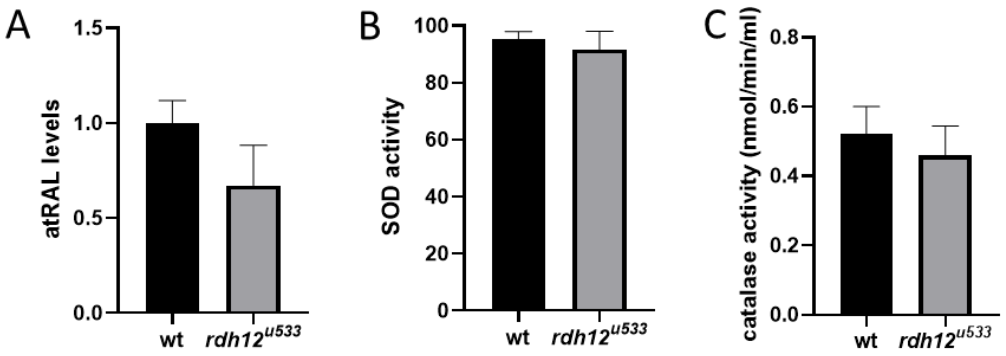

Figure 27: Analysis of atRAL levels and antioxidant enzyme activity in *rdh12*^{u533} retina.
(A) atRAL levels in 16 mpf retina was analysed by HPLC. Activity of antioxidant enzymes **(B)** SOD **(C)** and CAT were analysed in 16 mpf retina but no significant differences were found between wt and rdh12 mutant fish. Data are expressed as mean ± SEM.

4.3. Discussion

Autosomal recessive biallelic mutations in *RDH12* are primarily associated with severe early onset retinal degeneration. *Rdh12* knockout mouse models do not recapitulate the severe phenotype observed in patients, however mild signs of retinal degeneration are detected in mice exposed to intense light (Bian et al., 2021) and Maeda et al. (2006) reported an accumulation of atRAL and slower ERG recovery after bleaching with increased susceptibility to light induced damage. Retinal homogenates displayed decreased capacity to reduce atRAL and increased levels of the RPE lipofuscin A2E were found in *Rdh12*$^{-/-}$ eyes at 3-6 months (Kurth et al., 2007, Chrispell et al., 2009).

Comparison of the human and zebrafish RDH12 protein sequences revealed high homology, including conservation of the cofactor binding and active sites. In this chapter, a *rdh12* mutant zebrafish model was generated using CRISPR/Cas9 gene editing. Mutagenesis resulted in a 7 bp deletion (c.17_23del; p.(Val6AlafsTer5)), which is predicted to cause frameshift and premature termination in exon 1. Although knockout of rdh12 protein could not be confirmed due to lack of available antibody, *rdh12* mRNA expression was significantly reduced in the mutant fish, indicating nonsense mediated decay and the production of a null mutant. If translated, it is predicted to be severely truncated and lack any functionally conserved domains.

Characterisation of the *rdh12*^{u533} embryos at 5 dpf did not reveal a retinal phenotype and were comparable to wt fish in terms of retinal morphology and rhodopsin levels. Lack of functional RDH12 is thought to result in a build-

up of atRAL, which is toxic to cells. No differences in atRAL levels were noted in the *rdh12*^{u533} fish, and measurement of SOD activity did not reveal any signs of increased oxidative stress. This is in contrast to patients who develop an early onset phenotype, with symptoms typically presenting in infancy.

Fish were then raised to adulthood with further characterisation at 12 -16 mpf. At 12 mpf, *rdh12*^{u533} fish were largely comparable to wt fish, with normal development, morphology and retinal histology. However, rhodopsin was found to be mislocalised. This is consistent with RP being a rod-cone dystrophy, with the rods affected first. Deeper phenotyping was carried out with visualisation of retinal ultrastructure using TEM. This revealed significantly larger phagosomes in the RPE of the mutant fish. In addition, analysis of autophagy markers by RT-qPCR revealed a significant reduction in mRNA expression of *atg12*.

In phagocytosis, photoreceptor OSs are engulfed by the RPE into a phagosome, broken down and recycled back to the photoreceptors. Autophagy is the process of degradation of damaged organelles, aggregated proteins and lipids, under cellular stress. In autophagy, a double membraned vesicle, called an autophagosome, forms around the cellular content to be degraded, which then fuses with a lysosome, forming an autolysosome, and the engulfed contents are degraded. Phagocytosis and autophagy were thought to be two distinct processes, but recent studies suggest they are more closely linked (Sanjuan et al., 2007, Kim et al., 2013, Martinez et al.,

2015). The autophagy related protein Atg5 was found to co-localise with phagosomes containing OSs in control mouse RPE (Kim et al., 2013). *Atg5*-RPE knockout mice showed accumulation of phagosomes with undigested OSs and the OSs were not able to penetrate the RPE beyond the apical surface. These mice also had higher level of 11-cis, all-trans and 13-cis retinal. Kim et al. (2013) suggested that phagocytosis of the OSs by the RPE and the visual cycle converge via a non-canonical autophagy pathway, both of which are thought to be disrupted in *RDH12*-related retinopathies. In this pathway termed LC3-associated phagocytosis (LAP), following phagocytosis of the POS, the phagosome associates with the Atg12-Atg5-Atg16L complex, triggering lipidation of microtubule-associated protein 1 light chain 3 (LC3) to LC3-II and its recruitment to the phagosome. This signals for the lysosome to fuse with the phagosome, forming a phagolysosome resulting in degradation of ingested POS and it's recycling back to the photoreceptors. This pathway converges with the visual cycle, as OS phagocytosis aids in recycling of the visual pigments back to the photoreceptors. Enlarged phagosomes in the RPE of *rdh12*^{u533} fish indicate a disruption of RPE phagocytosis, with inefficient digestion of OSs. Disruption of phagocytosis along with a build-up of retinoids leads to formation of lysosomal bodies called lipofuscin. The retinoid pigments in lipofuscin are autofluorescent, and can often be seen at high levels on fundus images taken from patients with various retinal diseases (Nandakumar et al., 2012). *RDH12*-LCA patients have widespread RPE atrophy and fundus imaging typically shows central hypoautofluorescence corresponding to RPE cell death, surrounded by

hyperautofluorescent lesions, indicating regions of high toxicity and diseased RPE (Aleman et al., 2018).

Similar disruptions to retinal processes have been noted in other zebrafish models of retinal dystrophies. In a zebrafish model of *USH2A*-related RP, the *ush2a*^{rmc1} mutant, disruption in rhodopsin localisation and autophagy was also noted, with increased autophagosomes and increased gene expression of *atg5* and *atg12* and LC3 protein expression (Toms et al., 2020). Rhodopsin mislocalisation was also observed in the *rpgrip1*$^{-/-}$ zebrafish model, along with unformed rod outer segments, increased cell death and partially mislocalised cone opsins (Raghupathy et al., 2017).

In the *rdh12*^{u533} zebrafish retina at 12 mpf, *sod2* expression was significantly reduced by 2.2-fold compared to wt fish. Selective knockout of *Sod2* in the RPE of mice resulted in disorganised cristae and enlarged mitochondria in the RPE. Increased oxidative stress was seen in the photoreceptors and increased *Nrf2* expression in the RPE/choroid complex of *Sod2* mice (Brown et al., 2019). In another *Sod2* RPE knockdown mouse model, suppression of *Sod2* also resulted in increased oxidative stress, loss of ERG response, shortened inner and outer segments and thinner outer nuclear layer (Justilien et al., 2007). Overall SOD activity was not affected in the *rdh12*^{u533} fish up to 16 mpf, and expression of other antioxidant genes did not differ significantly between wt and *rdh12*^{u533} retinas, suggesting that sod1 and other antioxidant enzymes can compensate for the reduced *sod2* expression at this timepoint, thereby preventing oxidative stress and cellular damage.

Although no gross abnormalities were noted in retinal histology in the *rdh12*^{u533} fish and atRAL levels were comparable to wt fish, early indicators of disrupted pathways are observed in the adult fish including rhodopsin mislocalisation and increased phagosomal size with changes in autophagy-related expression, suggesting that stress in the retina is effectively controlled so as not to lead to apoptosis or severe disruption at least up till 12-16 months of age. This corresponds more with the autosomal dominant *RDH12*-associated RP phenotype, which is a later-onset and relatively mild phenotype in comparison to the severe early-onset LCA phenotype. A similar difference between the human and zebrafish phenotypes has been observed previously in the modelling of *KCNJ13*-LCA, where the homozygous zebrafish *kcnj13*^{td15} showed an adult-onset retinal degeneration contrasting with the early severe phenotype seen in patients (Toms et al., 2019). It is possible that compensatory mechanisms exist in the zebrafish, accounting for these differences. Although no other *rdh12* isoforms exist in the zebrafish, several RDHs are present in the retina that may compensate for lack of rdh12 in zebrafish. In addition, zebrafish are a cone-dominant species, and the cone specific visual cycle, which is independent of the RPE (Wang and Kefalov, 2011), may play a more prominent role in regeneration of the visual chromophore in zebrafish. As the mouse models of *RDH12* disease also do not show a severe phenotype, a species-specific role may exist for RDH12 in humans which is either redundant or compensated for in other species.

Further monitoring of the fish at later time points may reveal further disturbances as the disease progresses and provide more insight into the

rdh12 phenotype. For future work, retinal function can be assessed using optical coherence tomography and ERG. The visual cycle can also be investigated in the fish by quantification of 11-cis retinal levels to determine if the visual pigment is effectively being regenerated. In addition, expression of other retinol dehydrogenase isoforms can be analysed to determine if there are any compensatory mechanisms in place in the zebrafish. Finally, bright light can be used to exacerbate retinal degeneration in the fish and may reveal a more pronounced phenotype or lack of protection from light induced damage, similar to the mouse model which showed accumulation of atRAL after bleaching (Maeda et al., 2006), and the *ush2a*^{b1245} zebrafish model which did not show any signs of photoreceptor apoptosis under normal light conditions but when stressed with continuous light for 72 hours displayed significantly increased number of apoptotic cells compared to wildtype controls (Dona et al., 2018). If further disturbances are detected in the fish at later timepoints, they will be used for therapeutic studies.

5. Generation of HEK-293 stable cell line expressing wildtype and mutant *RDH12*

5.1. Aims

RDH12 is responsible for the reduction of atRAL to atROL, as part of the visual cycle. Lack of functional RDH12 is thought to result in a build-up of atRAL in the photoreceptors, causing toxicity and resulting in retinal degeneration. atRAL is a highly reactive molecule, and if not reduced, is toxic to cells inducing oxidative stress (Zhu et al., 2016, Li et al., 2015). There are currently no treatments available for *RDH12*-related retinopathies, and little is known about the disease mechanisms. The aim of this chapter was to generate a stable cell line expressing wildtype WT and mutant RDH12, in order to study the function of RDH12, through the development of a functional assay, investigate the disease mechanisms and screen for potential therapeutic candidates.

5.2. Results

5.2.1. Generation of HEK-293 stable cell lines

As there are currently no available cell lines natively expressing RDH12, a HEK-293 cell line expressing WT RDH12 was created. To create a stable cell line, HEK-293 cells were transfected with a vector encoding *RDH12* with a C-terminal GFP tag and grown under antibiotic selection pressure. The vector contains the gene encoding neomycin resistance, and therefore all untransfected cells die in the presence of G418. Cells were grown in media containing G418 until distinct colonies formed, which were isolated and

expanded. Western blot was used to evaluate expression of RDH12 (**Figure 28A**), with a band at approximately 65 kDa corresponding to RDH12-GFP. RDH12 localises to the ER (Keller and Adamski, 2007). Immunostaining of GFP and calnexin, an ER marker, confirmed the native localisation of RDH12 to the ER (**Figure 28C**). In order to determine if RDH12 is enzymatically active, an activity assay was carried out using HPLC. Protein was extracted from cells and incubated with atRAL and NADPH. Retinoids were extracted, separated, and analysed by HPLC. WT RDH12 protein exposed to atRAL resulted in production of atROL, compared to protein from untransfected cells, where no atROL was detected (**Figure 29**). This confirmed that the stable cell line expresses WT RDH12, which is correctly localised to the ER, and is active.

In order to study disease mechanisms and screen potential therapeutics for *RDH12*-retinopathies, three mutant *RDH12* stable HEK-293 cell lines were created; two expressing missense mutations (p.Y226C and p.A109P) and one nonsense mutation (p.S13*). Site directed mutagenesis was used to introduce mutations into the WT *RDH12* plasmid, and mutagenesis was confirmed by Sanger sequencing. Western blot probing for RDH12 was used to analyse levels of protein expression (**Figure 28A**). The p.Y226C mutant showed no protein expression, consistent with previous publications (Lee et al., 2007). Cells expressing the p.A109P mutant showed reduced expression of RDH12, whereas the p.S13* mutant showed no protein expression, consistent with it being a null mutant and therefore no full length protein is produced. Expression levels were also consistent with GFP fluorescence

observed (**Figure 28B**). The HPLC activity assay showed significantly reduced retinol production in the p.Y226C (3.5 ± 1.6%) and p.A109P lines (2.7 ± 0.3%) ($p<0.0001$) and no activity in the p.S13* line (**Figure 29**).

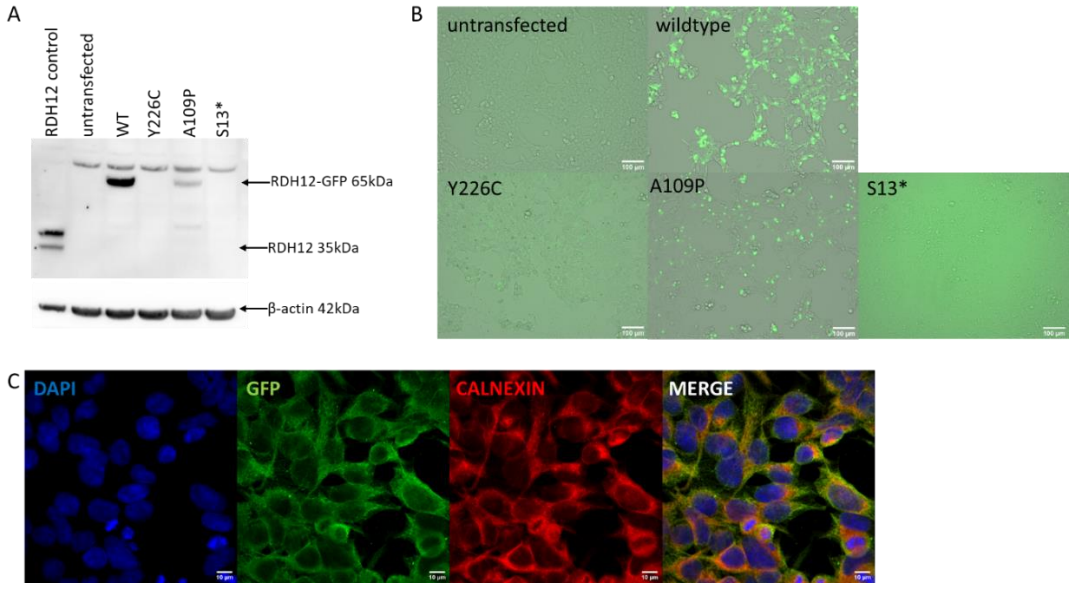

Figure 28: Generation of HEK-293 stable cell line expressing wildtype and mutant RDH12.
(A) Western blot analysis of HEK-293 cells transfected with GFP-tagged RDH12. RDH12 transfected HEK293T cell lysate was used as a positive control. Blot was probed with anti-RDH12. WT RDH12-GFP is detected at 65 kDa in stable cell line. p.Y226C and p.S13* cell lines show no RDH12 protein expression, while p.A109P shows reduced expression. Blot was stripped and re-probed with anti-β-actin. **(B)** GFP fluorescence of stable cell lines. Fluorescence levels confirm expression levels observed by western blot. **(C)** Calnexin staining confirmed localisation of RDH12 to the endoplasmic reticulum.

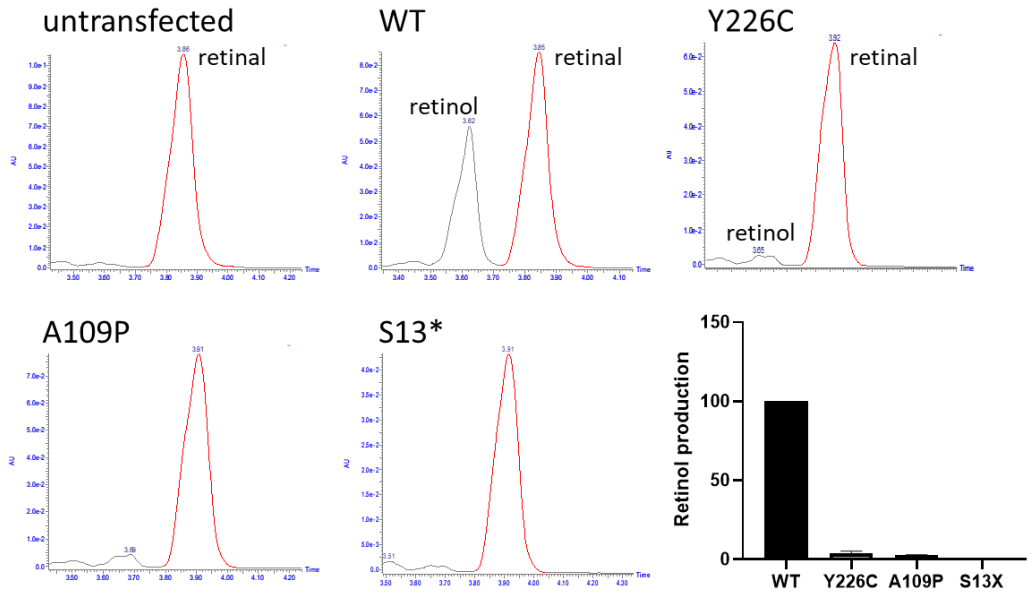

Figure 29: RDH12 activity assay using HPLC.
RDH12 activity assay using HPLC showed no atROL was detected in untransfected cells, but it was found in WT cells, confirming active functional RDH12. Enzyme activity in mutant cell lines were significantly reduced.

5.2.2. RDH12 protects cells from all-trans retinal induced toxicity.

High concentrations of atRAL are toxic to cells. Hence, in order to determine the ability of RDH12 to protect cells against atRAL toxicity and whether mutant cells retain this ability, increasing concentrations of atRAL were added to cells for 24 hours and cell viability was assessed by MTT assay. In untransfected cells, increasing concentrations of atRAL resulted in a dose dependent decrease in cell viability. However, in cells expressing WT RDH12, no significant decrease in cell viability was observed with atRAL up to 100 µM (**Figure 30**). At 100 µM atRAL, WT cells offered significant protection with 84% cell viability compared to untransfected cells which displayed only 26% viability ($p<0.001$). In all mutant lines, decreased cell viability was observed compared to WT at concentrations of 50 µM atRAL and above, consistent with the reduced expression and activity of mutant RDH12. In cells expressing the p.Y226C and p.S13* mutants, no increased

protection against atRAL toxicity was observed compared to the untransfected cells. However, the p.A109P mutant cells did offer increased protection (64% cell viability) against 100 µM atRAL toxicity compared to the untransfected cells (p=0.023), consistent with reduced expression of the p.A109P mutant protein, as opposed to no expression of the p.Y226C and p.S13* mutant proteins

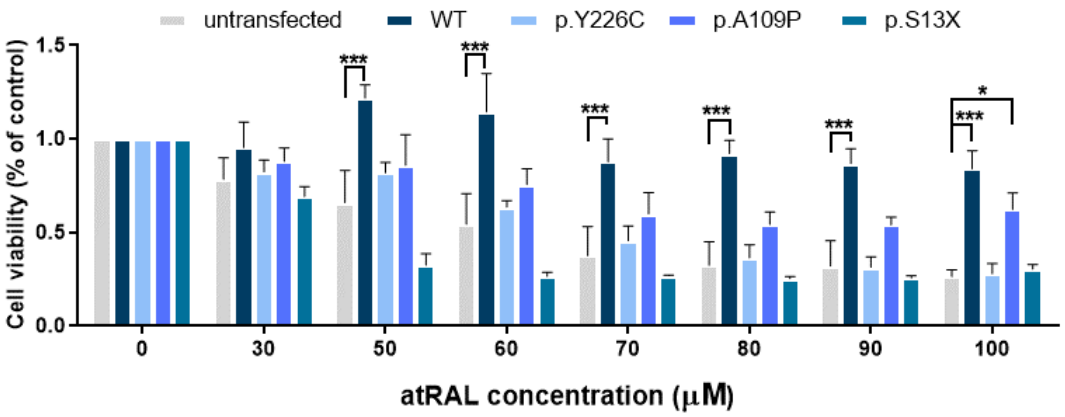

Figure 30: RDH12 protects cells against atRAL induced toxicity. Cells were dosed with increasing concentrations of atRAL for 24 hours and cell viability was assessed by MTT assay. atRAL is toxic to untransfected cells, whereas cells expressing WT RDH12 were protected from atRAL induced cell death. p.Y226C and p.S13* mutant RDH12 did not protect cells from atRAL toxicity, whereas p.A109P mutant protein offered significantly higher protection than untransfected cells at 100 µM atRAL concentration. Three independent experiments were performed. Data is expressed as mean ± SEM, and analysed using two-way ANOVA, followed by Dunnetts multiple comparison test. *p ≤0.05, **p ≤ 0.01, ***p ≤ 0.001.

5.2.3. atRAL induces oxidative stress in mutant cell lines.

Excess atRAL has been shown to induce oxidative stress in ARPE-19 cells, resulting in an increase in ROS (Li et al., 2015). SOD is the first line of defence antioxidant enzyme that dismutates superoxide anions to hydrogen peroxide. SOD activity was measured following dosing with 50 µM atRAL for 24 hours. In untransfected cells, this significantly reduced SOD activity to

28% ($p<0.0001$), indicating an increase in ROS beyond the capacity of SOD enzymes resulting in oxidative stress. In contrast, SOD activity was not affected by addition of atRAL in WT RDH12 cells, demonstrating that protection was conferred by the WT protein. SOD activity was reduced in all three mutant lines, indicating an increase in oxidative stress levels and impairment of the compensatory defence mechanisms (**Figure 31A**). However, SOD activity following atRAL dosing, was reduced to 31% in the p.Y226C and p.S13* lines, whereas in the p.A109P line, it was reduced only to 57%, indicating that the p.A109P cells still retain some protective ability against atRAL induced oxidative stress. RNA expression of oxidative stress markers were also analysed by RT-qPCR in mutant cell lines treated with atRAL, which resulted in a significant increase in *NRF2* in the p.Y226C line ($p=0.0132$) and in *HO-1* in p.Y226C and p.S13* mutant lines ($p=0.004$ and $p=0.0006$, respectively). *CAT* mRNA expression was significantly reduced in all 3 mutant cell lines (**Figure 31B**).

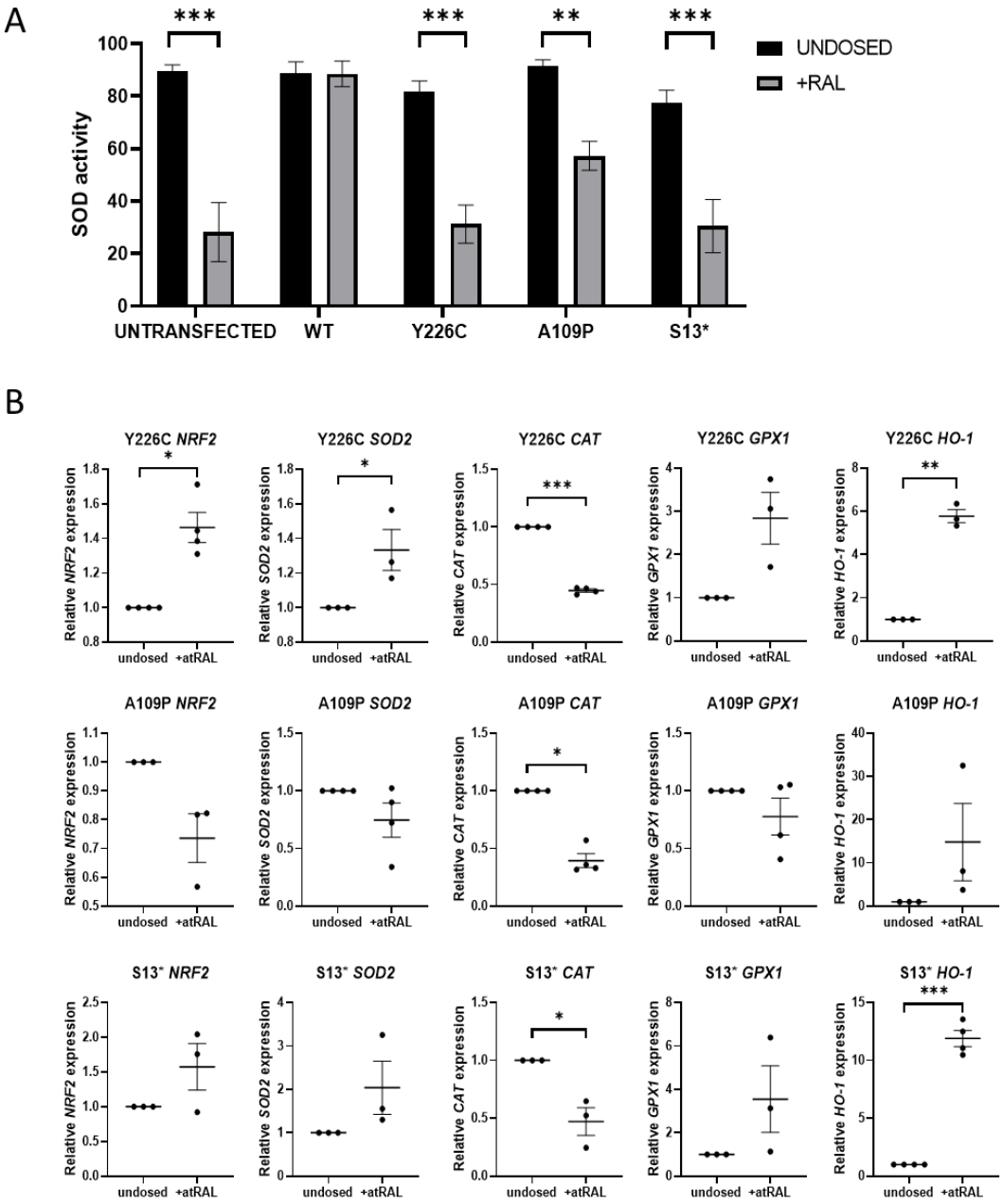

Figure 31: RDH12 protects cells from atRAL induced oxidative stress. **(A)** Dosing untransfected cells with 50 µM atRAL for 24 hours causes a significant reduction in SOD activity, indicating an increase in oxidative stress. Cell expressing WT RDH12 are protected from atRAL induced oxidative stress. Dosing with atRAL causes a significant reduction in SOD activity in mutant cells. Statistical significance was analysed using two-way ANOVA and Sidak's multiple comparison test. **p ≤ 0.01, ***p ≤ 0.001. **(B)** Expression of oxidative stress markers *NRF2*, *SOD2*, *CAT*, *GPX1* and *HO-1* were analysed by RT-qPCR following treatment with 50 µM atRAL for 24 hours. Statistical significance was analysed with paired t-test. *p ≤ 0.05, **p ≤ 0.01, ***p ≤ 0.001.

5.2.4. atRAL induces ER stress in *RDH12* mutant cell lines.

atRAL has previously been shown to induce ER stress in ARPE-19 cell (Li et al., 2015, Zhang et al., 2020). Expression of ER stress markers, *sXBP1*, *ATF4* and *CHOP*, were analysed by RT-qPCR. Expression of *sXBP1* was increased in all mutant lines compared to WT RDH12 cells, with a 2.3, 2 and 2.2-fold increase in p.Y226C, p.A109P and p.S13* cells, respectively. This could be a result of RDH12 misfolding caused by the mutations, triggering the unfolded protein response (UPR) pathway. Incubation with 50 µM atRAL for 24 hours resulted in a significant increase in expression of *sXBP1* by 14.6, 6.6 and 9.6-fold in the p.Y226C, p.A109P and p.S13* cells compared to undosed cells, respectively. Treatment with atRAL also significantly increased expression of *CHOP* by 6.3, 5.2 and 7.6-fold and *ATF4* by 3.4, 3.5 and 4-fold in p.Y226C, p.A109P and p.S13* lines, respectively (**Figure 33**).

5.3. Therapeutics targeting atRAL induced stress.

Mutations in *RDH12* result in an inability of the enzyme to reduce atRAL, leading to increased oxidative and ER stress, triggering cell death. A number of drugs were tested for their ability to reduce atRAL induced stress in the mutant *RDH12* cell lines.

5.3.1. Pregabalin

Pregabalin is a primary amine containing drug, commonly used to treat epilepsy, nerve pain and anxiety (Cross et al., 2021), and was shown to protect *Rdh12*$^{-/-}$ knockout mice from light induced retinal degeneration (Maeda et al., 2011). Pregabalin was tested for its ability to reduce ER

stress. To determine the optimal dose, cells were treated with pregabalin at various concentrations (0.1 – 2 mM) for 24 hours and cell viability was quantified (**Figure 32**). Pregabalin did not have a cytotoxic effect on cells at concentrations up to 2 mM, therefore a middle dose of 1 mM was chosen. As shown in **Figure 33**, co-treatment of 1 mM pregabalin with atRAL for 24 hours significantly reduced expression of *sXBP1* in the p.Y226C ($p<0.0001$) and p.S13* ($p=0.0178$) lines, and reduced expression of *ATF4* in all mutant cell lines. These data show that pregabalin can reduce ER stress.

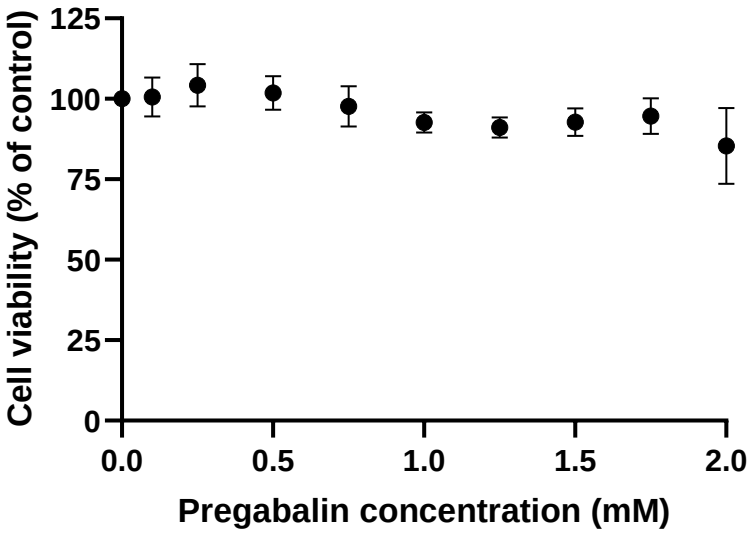

Figure 32: Pregabalin dose optimisation.
Cells were dosed with increasing concentrations of pregabalin for 24 hours and cell viability was analysed by MTT assay.

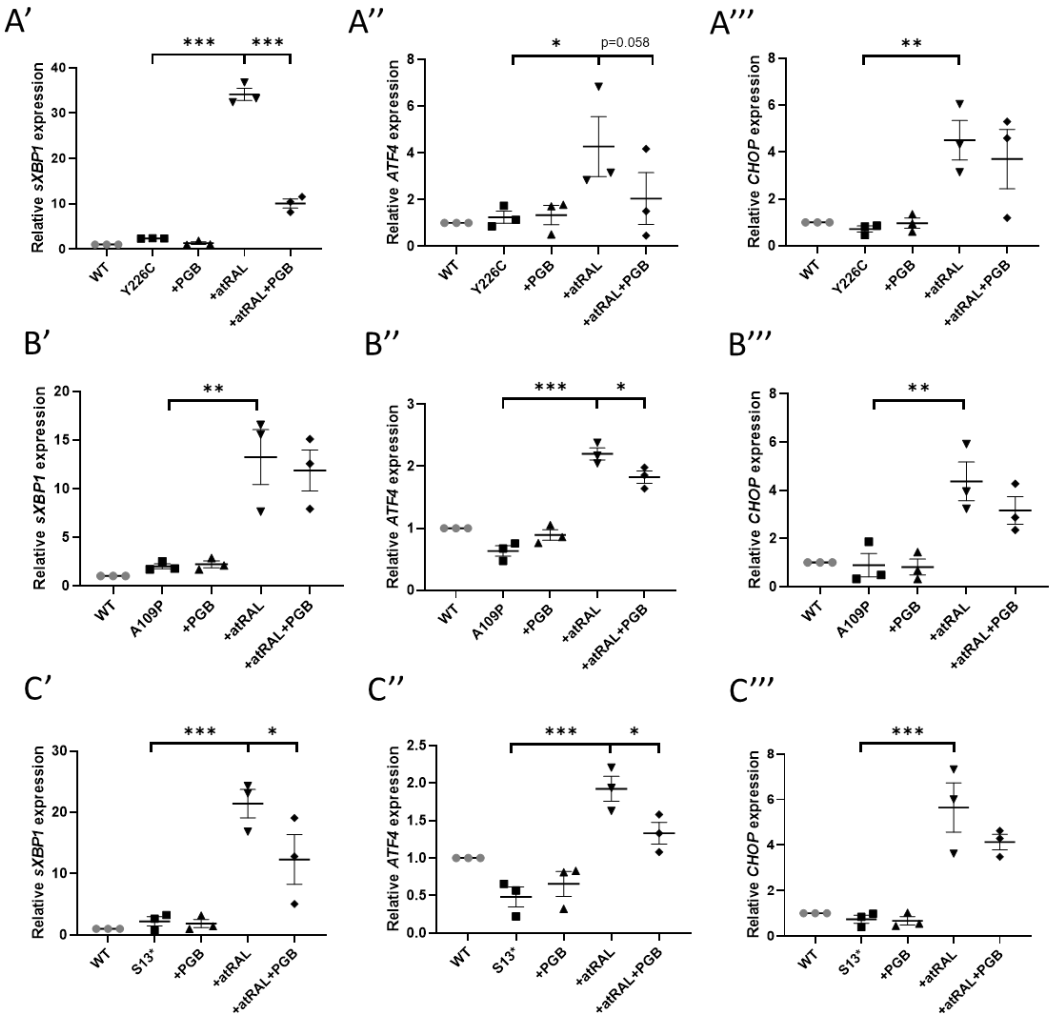

Figure 33: atRAL induced ER stress was attenuated by pregabalin. Cells were dosed with 50 µM atRAL, 1 mM pregabalin (PGB) or both for 24 hours. RT-qPCR was performed analysing the expression of ER stress markers. Dosing with atRAL significantly increased expression of sXBP1, ATF4 and CHOP in **(A)** p.Y226C, **(B)** p.A109P and **(C)** p.S13* cell lines. Dosing with pregabalin reduced expression of ER stress markers. Statistical significance was analysed using one-way ANOVA and Sidak's multiple comparison test. *p ≤0.05, **p ≤ 0.01, ***p ≤ 0.001.

5.3.2. N-acetylcysteine amide

N-acetylcysteine amide (NACA), an antioxidant, was tested for its ability to reduce atRAL induced oxidative stress. NACA was used at a concentration of 750 µM based on previous publications (Shi et al., 2009, Penugonda et al., 2005). Treatment with 750 µM NACA for 24 hours did not restore atRAL induced reduction in SOD activity, or significantly attenuate atRAL induced

changes in *NRF2* and *CAT* expression. However, NACA did show a general trend with reducing atRAL induced upregulation of *HO-1* expression in all mutant lines and significantly in the p.S13* line (p=0.0173) (**Figure 34**). NACA also significantly reduced expression of ER stress markers, *sXBP1*, *CHOP* and *ATF4*, in p.S13* line (**Figure 35**).

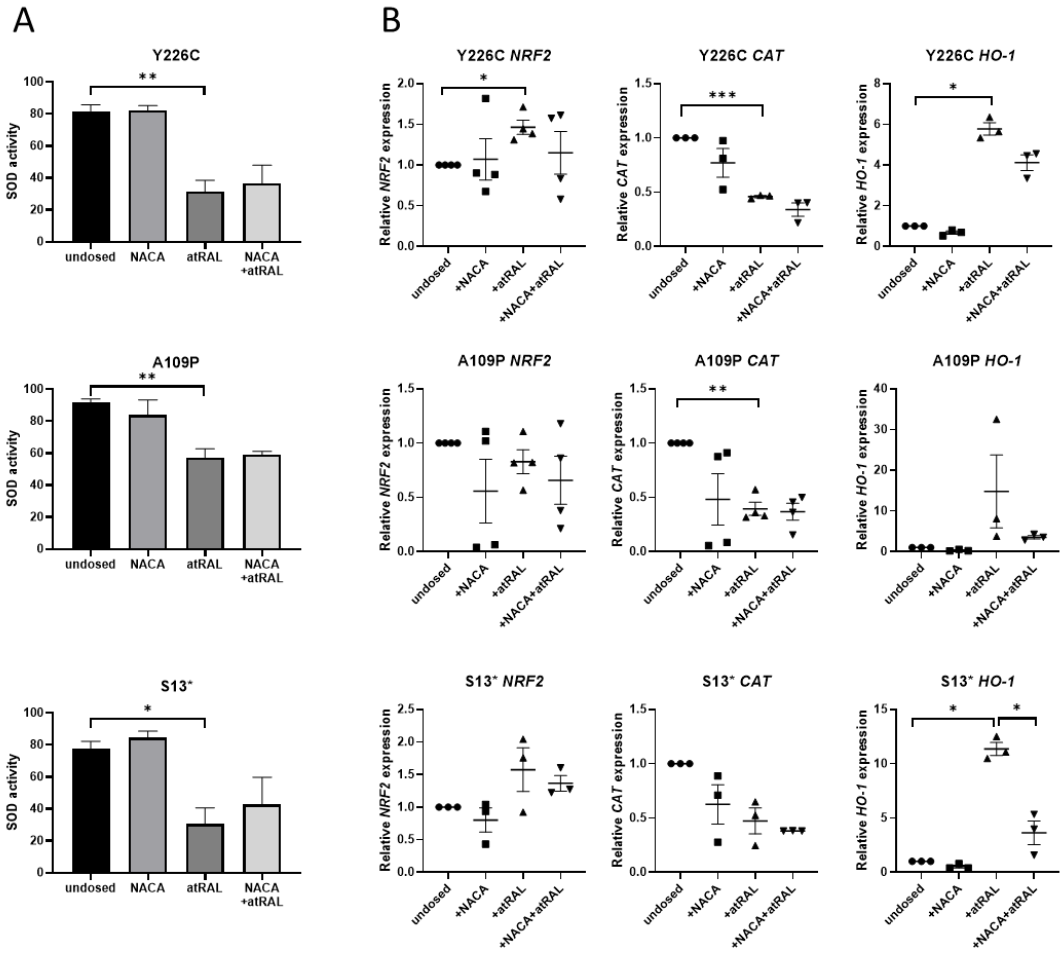

Figure 34: NACA does not attenuate atRAL induced oxidative stress. Cells were dosed with 50 µM atRAL, 750 µM NACA or both for 24 hours, then analysed by **(A)** SOD activity assay and **(B)** RT-qPCR of oxidative stress markers *NRF2*, *CAT* and *HO-1*. NACA reduced atRAL induced expression of *HO-1* in the p.S13* line. Statistical significance was analysed using one-way ANOVA and Sidak's multiple comparison test. *p ≤0.05, **p ≤ 0.01, ***p ≤ 0.001.

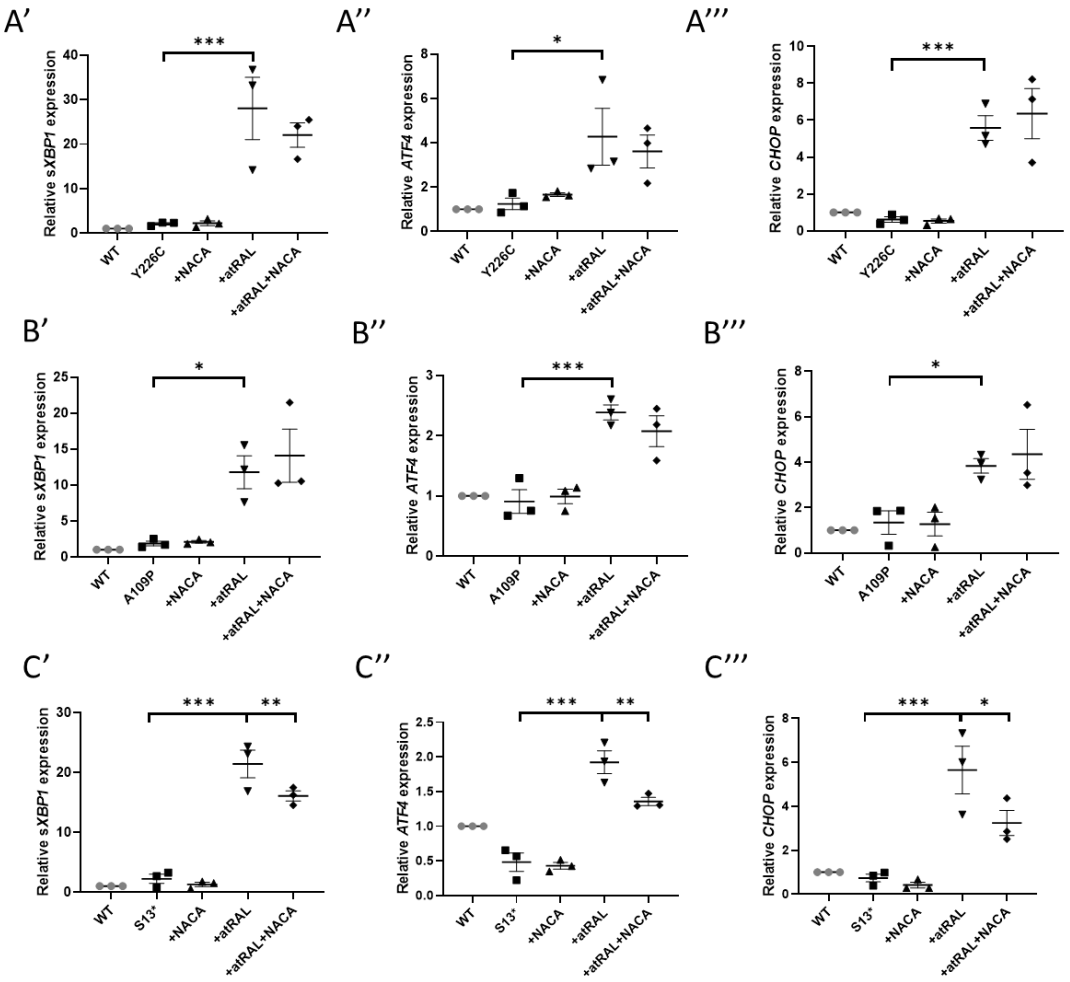

Figure 35: NACA reduces atRAL induced ER stress in the p.S13* cell line.
Cells were dosed with 50 µM atRAL, 750 µM NACA or both for 24 hours. RT-qPCR was performed analysing the expression of ER stress markers. NACA did not significantly reduce expression of ER stress markers in p.Y226C or p.A109P cell lines. NACA significantly reduces expression of *sXBP1*, *CHOP* and *ATF4* in p.S13* cell line. Statistical significance was analysed using one-way ANOVA and Sidak's multiple comparison test. *p ≤0.05, **p ≤ 0.01, ***p ≤ 0.001.

5.3.3. Tauroursodeoxycholic acid

Tauroursodeoxycholic acid (TUDCA), a drug that has ER stress inhibiting properties, was also tested. Cells were treated with TUDCA at various concentrations (25 – 300 µM) for 24 hours and cell viability was assessed to determine the optimal dose. A concentration of 100 µM TUDCA was chosen, as it was well tolerated by the cells (95% cell viability), with a minimal final

concentration of 0.5% DMSO (**Figure 36**). TUDCA did not reduce atRAL induced ER stress in any of the mutant cell lines (**Figure 37**).

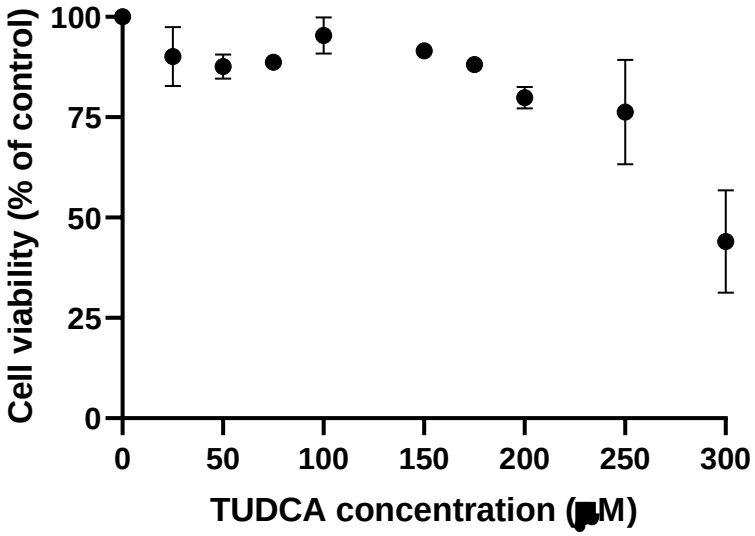

Figure 36: TUDCA dose optimisation.
Cells were dosed with increasing concentrations of TUDCA for 24 hours and cell viability was analysed by MTT assay.

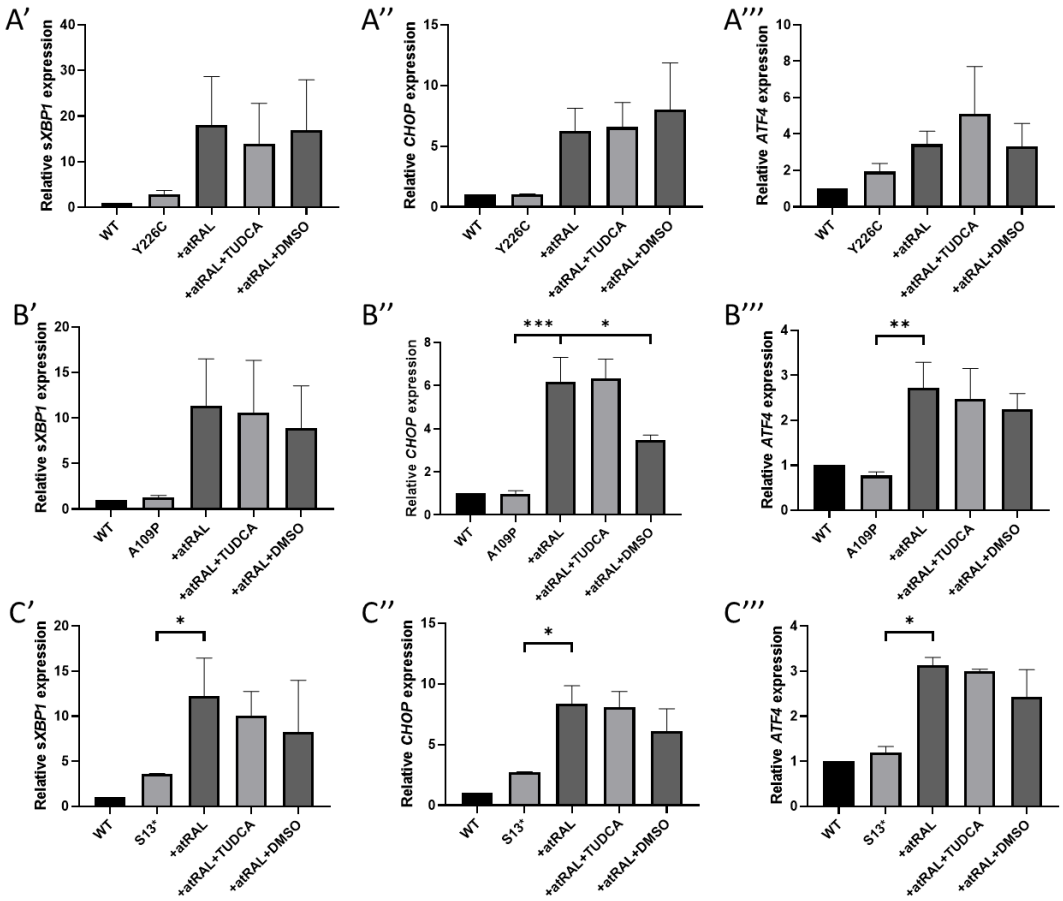

Figure 37: TUDCA does not reduce atRAL induced ER stress.
Cells were dosed with 50 µM atRAL alone or together with 100 µM TUDCA or 0.5% DMSO for 24 hours. Expression of ER stress markers was analysed by RT-qPCR. Data are expressed as mean ± SEM. Statistical significance was analysed using one-way ANOVA and Sidak's multiple comparison test. *p ≤0.05, **p ≤ 0.01, ***p ≤ 0.001.

5.4. Discussion

There are no cell lines available expressing RDH12 and the exact disease mechanism of *RDH12*-related retinopathies is not known. In this chapter, I created HEK-293 stable cell lines expressing WT and mutant *RDH12*. The WT line expressed RDH12, which was correctly localised to the ER and was functionally active, converting atRAL to atROL. Three cell lines, expressing mutations associated with *RDH12*-LCA, were created, the p.Y226C and p.S13* lines resulted in no protein expression and the p.A109P line had reduced RDH12 expression. All mutant lines had significantly reduced activity. This is consistent with a previous study, in which COS-7 cells were transiently transfected with various *RDH12* missense mutants and 11 out of 14 variants showed significantly reduced enzyme activity, 5-18% of wild type levels, and decreased expression levels (Thompson et al., 2005). This is most likely as a result of protein instability caused by misfolding of the protein.

Lack of functional RDH12 is thought to result in a build-up of atRAL, which is a highly reactive molecule, and if not reduced, is toxic to cells. RDH12 protected cells from atRAL induced cell death and mutant protein lost this protective ability. However, the p.A109P mutant, which is expressed at reduced levels, provided increased protection to the cells compared to untransfected cells. Whereas the p.Y226C and p.S13* cells, where there was no RDH12 expression, did not offer any increased protection. Therefore, drugs that can clear excess atRAL represent potential therapeutic benefit for *RDH12*-retinopathies. In the study by Maeda et al. (2011), drugs containing a

primary amine group were shown to protect *Abca4*$^{-/-}$*Rdh8*$^{-/-}$ mice from light induced retinal degeneration. A primary amine group can bind the aldehyde group of atRAL to form a reversible Schiff base, therefore reducing the levels of toxic atRAL in the retina. Schiff bases were detected in the retina of *Abca4*$^{-/-}$*Rdh8*$^{-/-}$ mice treated with primary amine containing drugs, which corresponded with a reduction in atRAL levels. Transient formation of the Schiff base prevents complete depletion of atRAL; instead, excess atRAL is released slowly allowing it to enter back into the visual cycle. This method of sequestration or scavenging of atRAL represents a potential therapeutic avenue for *RDH12*-related retinopathies.

Several studies have linked a build-up of atRAL to an accumulation of ROS in ARPE-19 cells leading to oxidative stress (Chen et al., 2012b, Li et al., 2015, Zhang et al., 2020, Zhu et al., 2016). Exposure of *Abca4*$^{-/-}$ *Rdh8*$^{-/-}$ mice to bright light induced atRAL build-up, which also lead to an increase in ROS in the photoreceptors (Chen et al., 2012b). Exposure of ARPE-19 cells to atRAL resulted in upregulation of *NRF2* and antioxidant genes heme oxygenase 1 (*HO-1*) and *y-GCSh* (Li et al., 2015). Nrf2 (nuclear factor E2-related factor 2) is a transcription factor that regulates the cells response to oxidative stress through the expression of antioxidant and detoxifying genes. Under normal conditions, *Nrf2* expression in the cytoplasm is controlled by Keap1. Cysteine residues on Keap1 detect ROS levels in the cells, and under high ROS levels, a confirmational change in Keap1 releases Nrf2, which translocates to the nucleus and binds to the antioxidant response element in the promoter region of antioxidant and phase II detoxifying

enzymes, like HO-1, NAD(P)H Quinone Dehydrogenase 1 (NQO-1), glutathione peroxidase (GPX), SOD and CAT (Buendia et al., 2016, Nakagami, 2016). Similarly in this study, atRAL treatment increased expression of *NRF2* in the p.Y226C cell line, and increased *HO-1* expression in all mutant lines. The redox state of the cell is controlled by a fine balance between the level of ROS and antioxidants. Oxidative stress is a result of an imbalance between ROS and antioxidant levels. Under mild stress, antioxidant enzymes scavenge ROS to maintain homeostasis in the cell. However, if ROS levels become too high, cellular homeostasis is disrupted and antioxidant enzymes become overwhelmed as they cannot cope with the high ROS load (Rahman, 2007). A significant reduction in *CAT* mRNA expression and SOD enzyme activity was observed in atRAL treated mutant cells, indicating that the antioxidant defence mechanisms of the cell are impaired and cannot protect the cells against the high free radical load.

atRAL has also been shown to induce ER stress (Li et al., 2015, Zhang et al., 2020), which leads to an accumulation of misfolded proteins in the ER, triggering the UPR pathway. The UPR is activated through three sensors: PKR-like ER kinase (PERK), inositol requiring enzyme 1 (IRE1) and activating transcription factor 6 (ATF6), which are associated with binding immunoglobulin protein (BiP/GRP78). Upon activation of these sensors by autophosphorylation, they dissociate from BiP, triggering a cascade of events resulting in inhibition of protein translation, chaperone expression and protein degradation (Shacham et al., 2019). Activation of IRE1 leads to splicing of *XBP1* resulting in *sXBPI*, which activates UPR genes responsible

for protein folding, trafficking and degradation. Activation of PERK results in activation of ATF4, leading to upregulation of UPR genes. Activation of ATF6 results in its translocation to the Golgi, where it is cleaved and then translocated back to the nucleus, where it induces expression of target genes, including chaperones. The role of these pathways is to alleviate ER stress and restore ER homeostasis, however when ER stress becomes overwhelmingly high, ATF4 activates C/EBP homologous protein (CHOP), which in turn triggers apoptosis (Lin et al., 2008, Adams et al., 2019). ROS have been shown to co-localise with the ER in atRAL treated ARPE-19 cells and induce ER stress via activation of the PERK-eIF2α-ATF4 pathway with increased expression of ER stress markers *BiP, ATF4* and *CHOP* (Li et al., 2015). Similarly in this study, incubation with atRAL resulted in an increase in mRNA expression of *sXBP1, ATF4* and *CHOP* in all mutant lines, indicating that atRAL activated ER stress induced apoptosis.

This study has revealed that atRAL build up, caused by non-functional RDH12, induces oxidative and ER stress, two pathways that are closely linked. If cellular homeostasis is disrupted in any way, for example by a build-up of ROS, the ER becomes stressed, leading to an accumulation of unfolded or misfolded proteins. In order to restore homeostasis, the UPR pathway is activated, however refolding of proteins by the UPR leads to production of more ROS, causing redox imbalance, which in turn triggers further ER stress (Chong et al., 2017). If cellular homeostasis is disrupted to a level where it cannot be restored, apoptosis is triggered. Therefore, drugs

acting on these pathways would be beneficial for the treatment of *RDH12*-retinopathies.

A number of drugs were tested for their ability to reduce atRAL induced ER and oxidative stress. Pregabalin is commonly used to treat epilepsy, nerve pain and anxiety (Cross et al., 2021). Pregabalin contains a primary amine group and was shown to reduce atRAL levels in *Rdh12*$^{-/-}$ mice (Maeda et al., 2011), and reduce ROS production in light exposed *Abca4*$^{-/-}$ *Rdh8*$^{-/-}$ mice (Chen et al., 2012b). Pregabalin also had a neuroprotective effect in a rat model of diabetic retinopathy, by reducing retinal glutamate, nitric oxide and malondialdehyde and increasing GSH levels and restored retinal histology, by increasing retinal thickness and ganglion cell layer count (Ali et al., 2019). In the current study, pregabalin lowered expression of atRAL induced ER stress markers in HEK-293 cells expressing mutant RDH12, indicating that sequestration of atRAL by pregabalin alleviates ER stress in the cells, highlighting a new mechanism of action for pregabalin and could be used as a possible treatment for *RDH12*-retinopathies. Further work is required to validate these results in animal models of *RDH12*-retinopathies and determine its ability to slow down retinal degeneration, by assessing retinal histology and visual function, which was not done in the Maeda et al. (2011) paper. In addition, it would be interesting to look at ER stress markers in the mouse model to determine if there is increased stress compared to wildtype mice, and whether treatment with pregabalin has the same effect, of lowering ER stress, on the mice as in cells. In order to translate this to patients, the drug would require reformulation either as an eye drop or intravitreal

injection. Following animal work, clinical trials would be required to determine the effectiveness in patients.

TUDCA is a bile acid commonly used to treat liver conditions. Many studies have shown that TUDCA can act as a chemical chaperone and reduce ER stress (Ozcan et al., 2006, Kusaczuk, 2019, Lee et al., 2019, Paridaens et al., 2017). TUDCA reduced ER stress and apoptosis and slowed down cone degeneration in a *Lrat*$^{-/-}$ mouse model of LCA (Zhang et al., 2012). TUDCA also attenuated H_2O_2 induced cell death and thapsigargin induced expression of ER stress markers CHOP and sXBP1 in ARPE-19 cells (Alhasani et al., 2020). However, TUDCA did not reduce atRAL induced ER stress in the RDH12 mutant cell lines.

The antioxidant drug N-acetylcysteine (NAC) was shown to inhibit cone death by reducing oxidative damage in RP mouse models (Lee et al., 2011) and a clinical trial is currently underway in RP patients (NCT03063021). The antioxidant mechanism of NAC is due to the ability of NAC to act as a precursor to glutathione (GSH). GSH is an important non-enzymatic antioxidant, but also acts as a substrate to many antioxidant enzymes, and oxidative stress causes a reduction in GSH levels. NAC has been shown to replenish GSH levels and can also break disulphide bonds, thereby releasing free thiols, which have better antioxidant capacity than NAC (Aldini et al., 2018). NACA is an amide derivative of NAC, which has improved lipophilicity, antioxidant properties and ability to cross the blood brain barrier (Sunitha et al., 2013). NACA was more effective at increasing GSH levels in red blood

cells from β-thalassemia patients, compared to NAC (Amer et al., 2008). NACA was shown to reduce ROS and lipid peroxidation in tert-butyl hydroperoxide treated ARPE-19 cells, by reducing malondialdehyde and increasing GSH levels, and protected mice from light induced photoreceptor damage (Schimel et al., 2011). NACA did not reduce atRAL induced oxidative stress in HEK-293 cells expressing p.Y226C and p.A109P mutant RDH12. However, atRAL induced expression of the oxidative stress marker *HO-1* and ER stress markers *sXBP1*, *ATF4* and *CHOP* were significantly reduced with NACA treatment, indicating that inhibition of oxidative stress reduces ER stress. This is consistent with previous studies which showed that inhibition of light induced oxidative stress with NAC also reduced ER stress in 661W photoreceptor cells and ARPE-19 cells (Song et al., 2020).

An important consideration for future studies is the role of RDH12 in the detoxification of lipid peroxidation products. The HEK stable cell lines created here can be used to study the role of RDH12 in protecting cells from toxic lipid peroxidation products, which could provide further information on RDH12 disease mechanisms.

In conclusion, HEK-293 cell lines expressing WT and mutant RDH12 were generated to study the effects of RDH12 dysfunction. WT RDH12 protected cells against atRAL induced cell death and oxidative stress, and mutant RDH12 lost this protective ability, resulting in a decrease in cell viability and an increase in atRAL induced oxidative and ER stress. Oxidative stress and ER stress have been identified as key pathways that are disrupted in

RDH12-related retinopathies and can be targeted for therapeutics. In addition, pregabalin was shown to reduce atRAL induced ER stress. Drugs with ER stress lowering properties, in addition to antioxidants and retinal scavengers, represent a new class of potential drugs that can be targeted for *RDH12*-related retinopathies.

6. Identification of a novel heterozygous variant, associated with autosomal dominant retinitis pigmentosa and generation of induced pluripotent stem cells (iPSCs)

6.1. Aims

One heterozygous variant in *RDH12* has been reported in a family with autosomal dominant RP. Patients displayed a late onset, relatively mild phenotype (Fingert et al., 2008). In contrast, autosomal recessive biallelic *RDH12* variants are associated with an early onset severe LCA phenotype (Fahim et al., 2019). The aim of this chapter was to generate and characterise iPSC lines from two patients, one with a dominant heterozygous and one with a recessive biallelic *RDH12* variant.

6.2. Results

6.2.1. Identification of a novel heterozygous *RDH12* variant

Patient 1 is a 32-year-old man of mixed ethnicity, mother from Kurdistan and affected father from Tunisia, who presented with nyctalopia and visual field loss, but preserved central vision. His best corrected visual acuity with LogMAR was 0.04 in both eyes, fundus examination showed mild waxy disc pallor with retinal vessel attenuation and mid-peripheral bone-spicules. He had a strong positive family history exhibiting autosomal dominant inheritance, with an affected father, paternal grandfather and siblings (**Figure 38A**). He underwent whole exome sequencing and was found to have a

heterozygous deletion in *RDH12* (NM_152443.2) (c.759delC; p.(Phe254Leufs*24)), which was confirmed by Sanger sequencing (**Figure 38C**). The pathogenicity of the variant was scored with SIFT_Indel (Hu and Ng, 2013), Variant Effect Predictor (McLaren et al., 2016) and MutationTaster (Schwarz et al., 2014), and all classified the variant as damaging or disease causing. No disease-causing mutations were found in any other known retinal disease genes. Patient 2 is an unrelated 37-year-old Caucasian English man with a maternal family history of RP, with an affected mother and maternal grandfather (**Figure 38B**). He has nyctalopia and progressive visual field loss but maintains good central and colour vision. His best corrected visual acuity is 0.18 LogMAR in both eyes and 17/17 colour vision using Ishihara. Fundus examination showed mild waxy disc pallor with retinal vessel attenuation and mid-peripheral bone-spicules similar to patient 1. Whole exome sequencing revealed the same heterozygous variant as patient 1, which segregated with his affected mother.

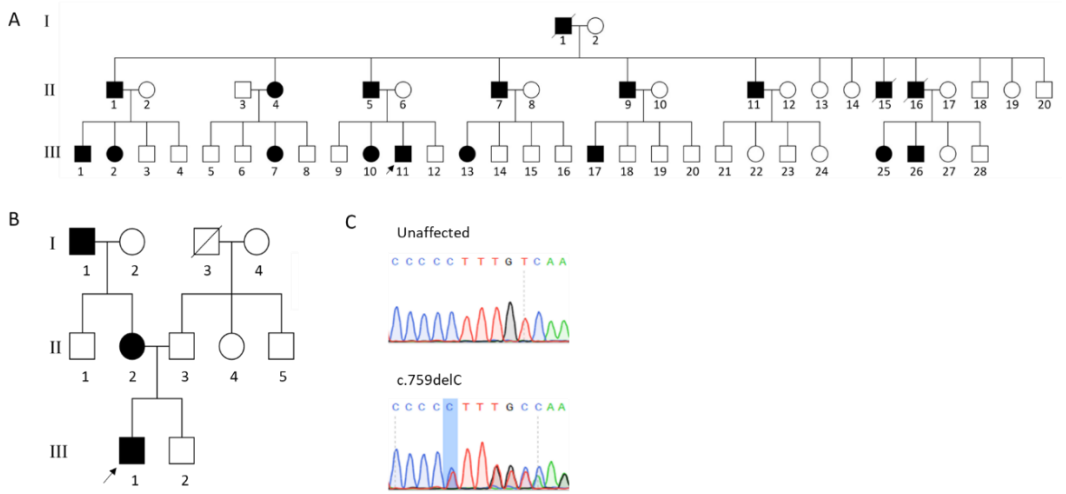

Figure 38: Novel heterozygous *RDH12* variant identified in two unrelated families.
Pedigree of family of **(A)** patient 1 and **(B)** patient 2 affected with autosomal dominant *RDH12*-retinitis pigmentosa. Males are represented by squares, and females by circles. Affected individuals are coloured in black. Deceased individuals are indicated with a slash and proband is indicated by an arrow. Children of unaffected parents did not have RP and are not shown. **(C)** Sanger sequencing traces confirming heterozygous c.759delC variant.

6.2.2. iPSC reprogramming and characterisation

A skin biopsy was taken from patient 1 described above (RDH12 AD) and a second patient (RDH12 AR); a 40 year old female with LCA, carrying a homozygous missense variant c.619A>G p.(Asn207Asp). Fibroblasts were derived and reprogrammed to iPSCs, via electroporation of non-integrating episomal plasmids (**Figure 39**). A slight modification was made to the protocol for reprogramming of RDH12 AR fibroblasts, with the addition of the small molecule sodium butyrate to increase reprogramming efficiency.

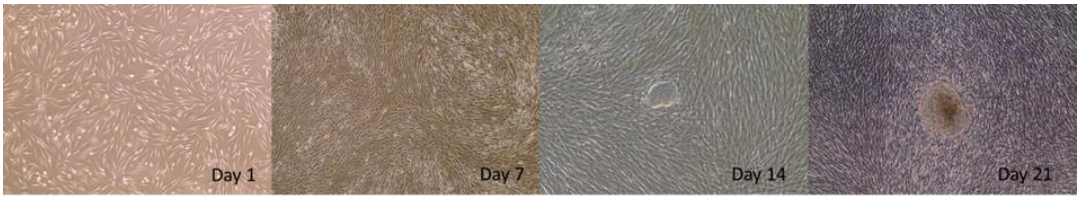

Figure 39: Reprogramming of fibroblasts to iPSCs.
Fibroblasts were reprogrammed using non integrating episomal plasmids. iPSC colonies begin to appear at day 14 and are ready to be picked at day 21. Individual colonies are manually dissected and expanded.

Variants were confirmed by Sanger sequencing (**Figure 40A**). The morphology of colonies was examined for characteristics of iPSCs, including flat, compact colonies with a cobblestone appearance and large nuclei to cytoplasmic ratio (**Figure 40B**). Colonies stained red for alkaline phosphatase, indicating cells are undifferentiated (**Figure 40C**). All colonies stained positive for pluripotency markers, OCT4 (nuclear marker), and SSEA3 (cell surface marker) (**Figure 40D**). mRNA expression of all pluripotency markers was increased compared to fibroblasts (**Figure 41**), and expression of plasmids were absent in iPSC colonies, confirming that plasmids had not integrated. Random differentiation of EBs stained positive for markers of endoderm (AFP), mesoderm (Vimentin) and ectoderm (PAX6), confirming differentiation potential to the three germ layers (**Figure 42**). G-banding karyotyping revealed a normal male 46,XY karyotype for RDH12 AD and low-pass whole genome sequencing analysis revealed normal female 46,XX karyotype for RDH12 AR (**Figure 43**). iPSC identity was confirmed by STR analysis, which revealed 100% match between the iPSC lines and parental fibroblast lines at 16 loci (**Table 8**).

STR site	RDH12 AD Fibroblast	RDH12 AD iPSC	RDH12 AR Fibroblast	RDH12 AR iPSC
FGA	19,23	19,23	21,27	21,27
TPOX	9,10	9,10	8,11	8,11
D8S1179	10,12	10,12	12,15	12,15
vWA	16,18	16,18	14,16	14,16
AMEL	X,Y	X,Y	X,X	X,X
Penta D	12,14	12,14	9,11	9,11
CSF1PO	11,12	11,12	10,12	10,12
D16S539	8,9	8,9	11,13	11,13
D7S820	12,12	12,12	10,11	10,11
D13S317	11,12	11,12	12,12	12,12
D5S818	12,13	12,13	12,12	12,12
Penta E	13,18	13,18	7,11	7,11
D18S51	13,13	13,13	13,16	13,16
D21S11	28,30.2	28,30.2	28,31.2	28,31.2
TH01	6,7	6,7	7,7	7,7
D3S1358	16,16	16,16	16,16	16,16

Table 8: STR analysis.
STR analysis revealed 100% match between the iPSC lines and parental fibroblast lines at 16 loci

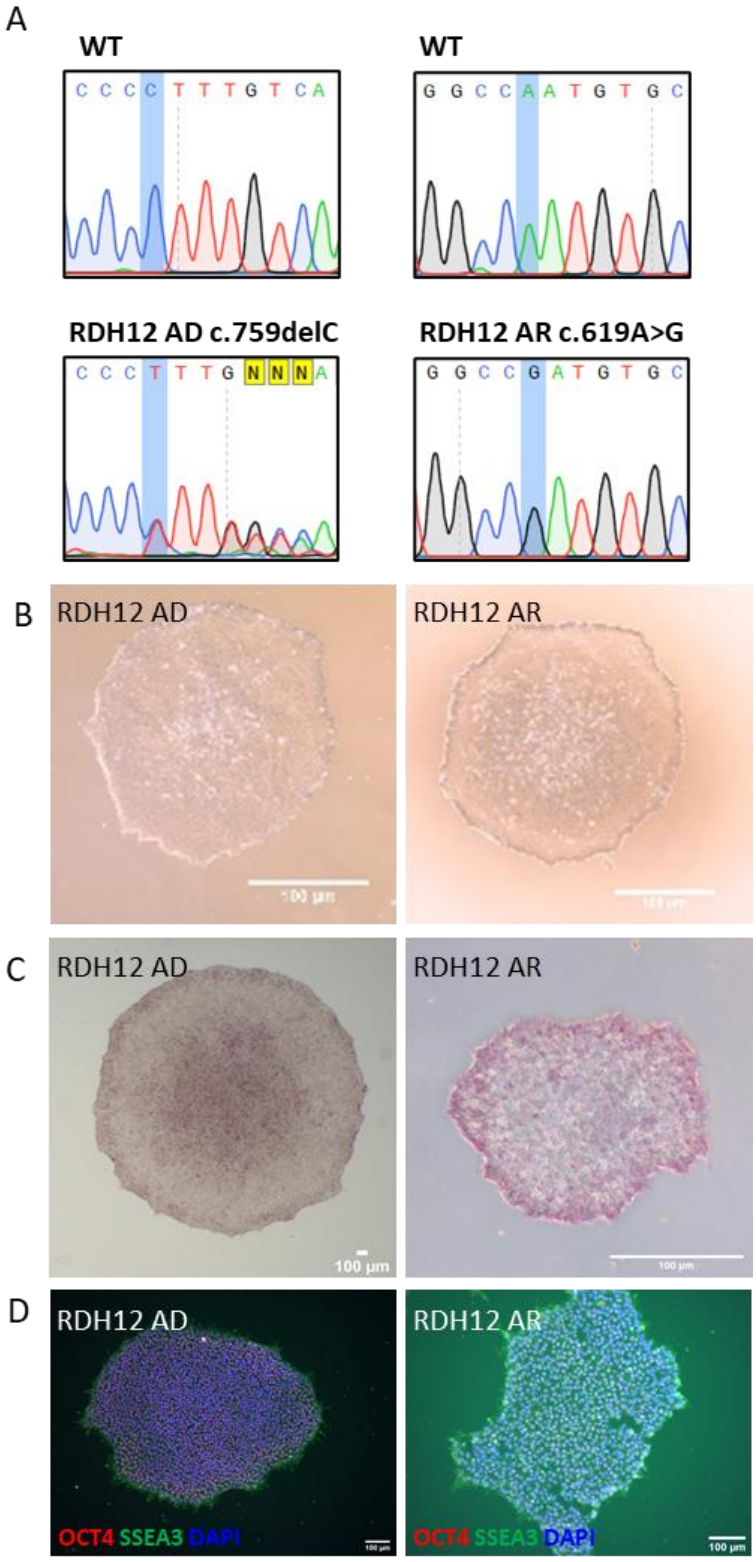

Figure 40: Characterisation of RDH12 iPSC lines
(A) Variants were confirmed by Sanger sequencing. **(B)** iPSC colony. **(C)** iPSC colony stained with alkaline phosphatase staining kit. Undifferentiated cells express high levels of alkaline phosphatase and appear red when stained. **(D)** Immunocytochemistry staining of iPSC colonies for pluripotency markers OCT4 and SSEA3. Nuclei were counterstained with DAPI.

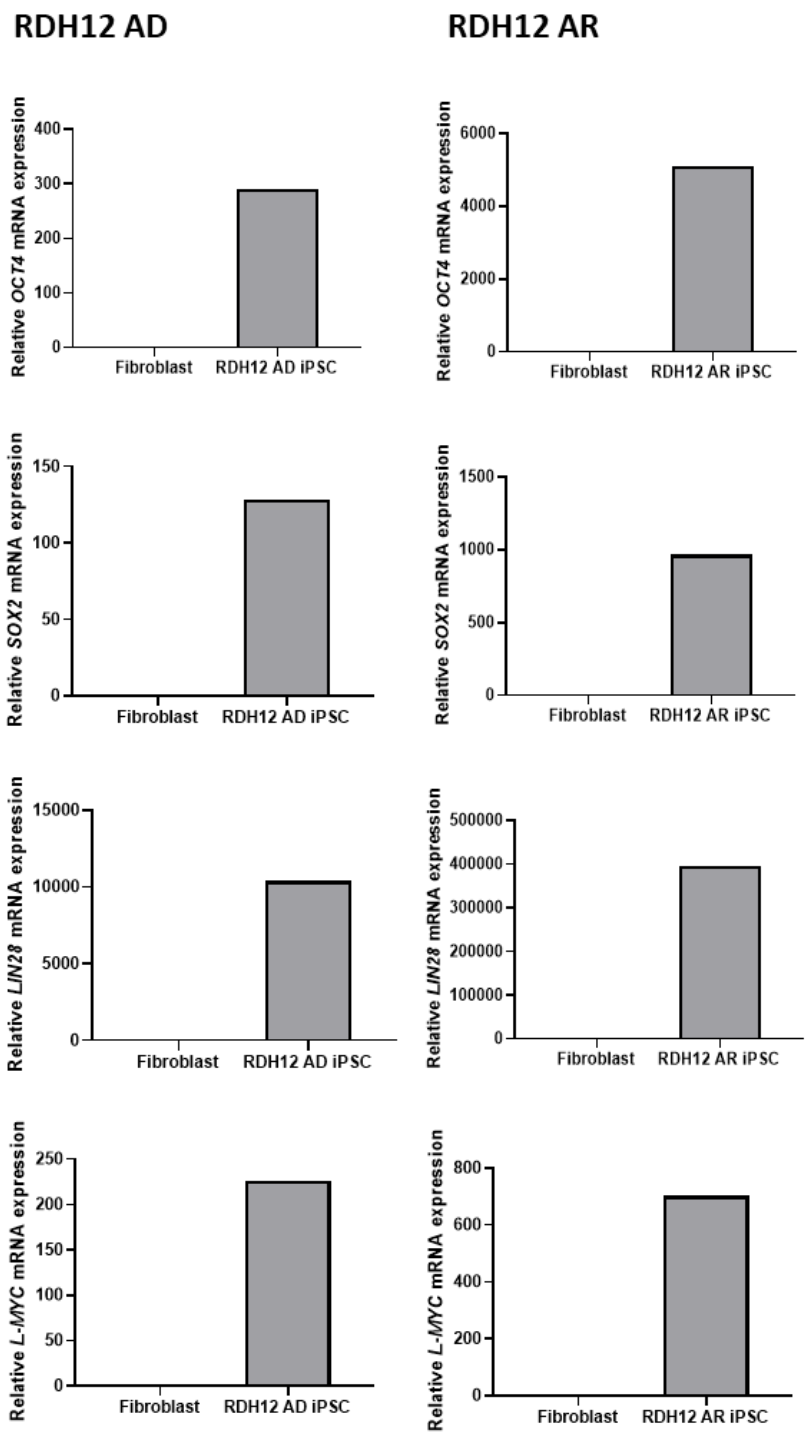

Figure 41: RT-qPCR of pluripotency markers.
mRNA expression of pluripotency markers was analysed by RT-qPCR. Expression of pluripotency markers *OCT4*, *SOX2*, *L-MYC* and *LIN28* was increased in iPSCs compared to fibroblasts.

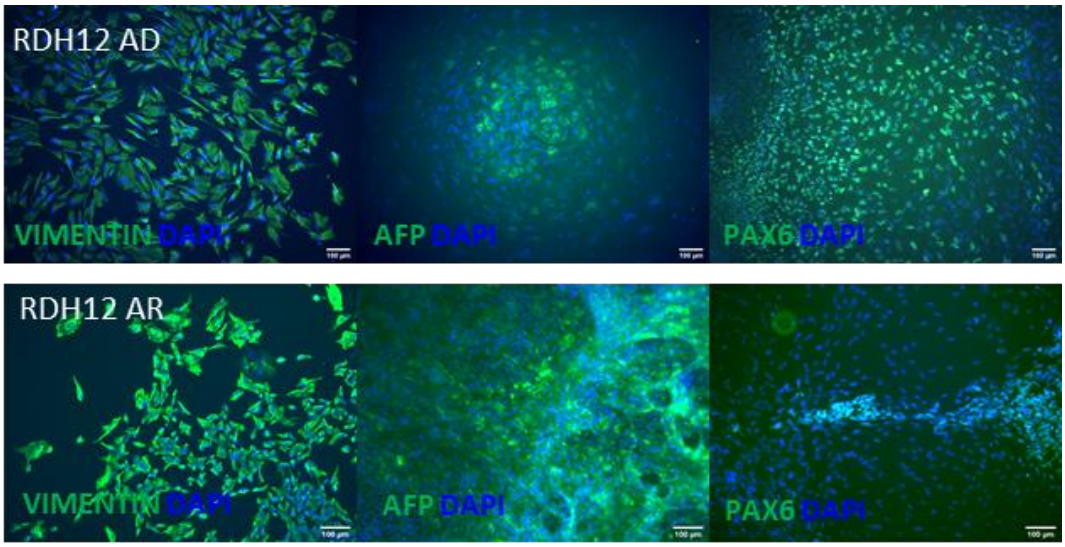

Figure 42: Differentiation of iPSCs into the three germ layers.
Random differentiation of embryoid bodies confirmed differentiation potential to the three germ layers. Immunocytochemistry staining of cells for germ layer markers Vimentin (mesoderm), AFP (endoderm) and PAX6 (ectoderm).

RDH12 AD

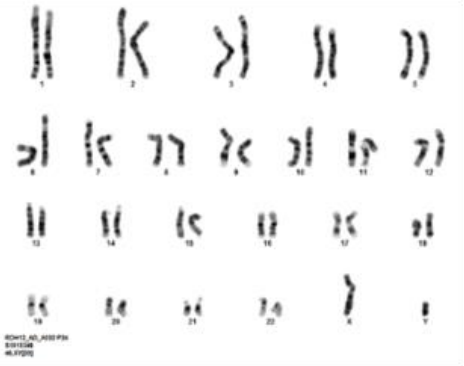

RDH12 AR

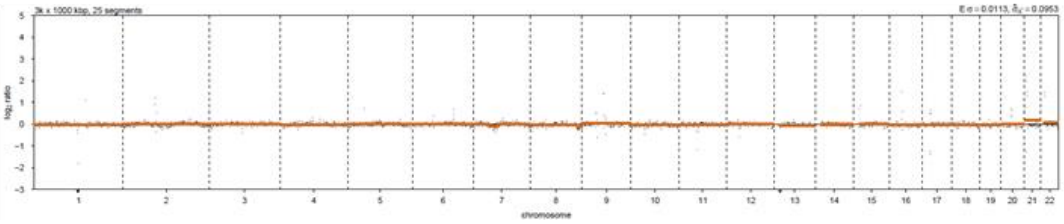

Figure 43: Karyotype analysis of RDH12 iPSC lines.
G-banding karyotyping revealed normal chromosomal structure for RDH12 AD and low pass whole genome sequencing revealed normal chromosomal structure for RDH12 AR.

6.3. Discussion

Mutations in *RDH12* are primarily associated with LCA and accounts for 3.4-10.5% of all cases (Kumaran et al., 2017). One case of an autosomal dominant variant, a single base pair deletion resulting in a frameshift and premature termination (c.776delG; p.(Glu260Argfs*18)), has been previously reported in a six-generation family with 19 affected members. Affected individuals displayed a milder late onset (average age of diagnosis was 28.5 years) RP phenotype, with intraretinal bone spicule pigmentation and attenuation of retinal arterioles (Fingert et al., 2008). Here, a novel heterozygous variant (c.759del; p.(Phe254Leufs*24)) in *RDH12* is reported in two unrelated families. Both patients similarly displayed a milder late onset phenotype, with mild waxy disc pallor with retinal vessel attenuation and mid-peripheral bone-spicules.

The mutation is located towards the end of the reading frame, with 80% of the sequence unchanged, including the two highly conserved catalytic domains: the cofactor binding site at positions 46-52, and the active site at 200-204. This mutation results in loss of the terminal 63 amino acids, which are highly conserved across species, causing premature termination at codon 277. Due to the proximity of the mutation to the final exon-exon junction, this transcript is likely to escape nonsense mediated decay and result in the expression of a truncated protein (Brogna and Wen, 2009). This variant is only 17 bp upstream from the previously reported heterozygous variant, and both give rise to a 277 amino acid protein, with a common 17 amino acid C-terminal sequence (**Figure 44**). More recently, following the

publication of our variant, a third novel variant has been identified in a four-generation family with autosomal dominant RP. Similarly, it is a single base pair deletion (c.763delG; p.(Val255Serfs*23)) resulting in frameshift and premature termination and generation of a 277 amino acid protein with an identical C-terminal peptide (Muthiah et al., 2021) (**Figure 44**).

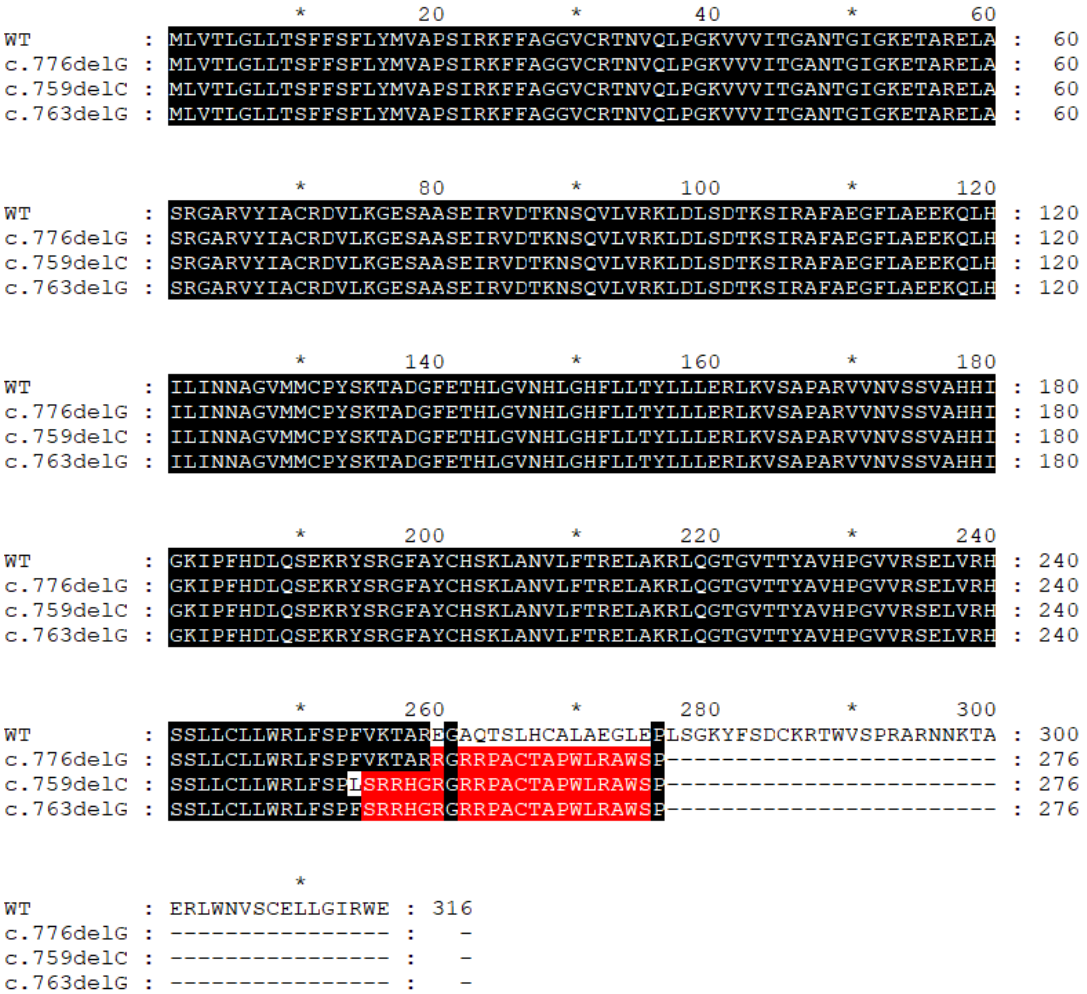

Figure 44: Alignment of RDH12 protein sequences, associated with autosomal dominant RP.
Alignment of the RDH12 (UniProt Q96NR8) sequence with the previously reported c.776delG variant, the current c.759delC variant and the new c.763delG variant. Identical residues to the WT sequence are highlighted in black, and identical residues between the mutant sequences are highlighted in red.

Ninety-nine *RDH12* variants have been reported to date, 61% of which are missense, 14% are nonsense and 14% are small insertions or deletions, including 8 autosomal recessive deletions associated with the severe early-onset LCA phenotype (HGMD accessed July 2021). A 5 bp deletion in the terminal exon, c.806_810del p.(Ala269Glyfs∗2), has been reported in patients with autosomal recessive LCA, which results in a truncated protein with only two out-of-frame amino acids and was shown to result in loss of function, with less than 5% enzyme activity seen *in vitro* (Sun et al., 2007), with heterozygous carriers not displaying a phenotype. The C-terminal peptide sequence produced by the heterozygous RP associated variants may be responsible for a protein interaction resulting in gain of function or a dominant negative effect, which may account for the mild RP phenotype. However, further functional studies into the differences in disease mechanisms between autosomal recessive and autosomal dominant variants are required, for example proteomic studies to identify RDH12 protein interactions sites.

A similar segregation has been observed in the *RPE65* gene, with autosomal recessive biallelic mutations linked to severe early onset LCA and the autosomal dominant p.D477G mutation associated with late-onset RP with choroidal involvement. The molecular pathology of this variant is also not fully understood. A number of mouse models have been generated with the p.D477G *RPE65* variant; however, all give rise to a very mild phenotype. It has been suggested that the dominant mutation has a possible dominant negative effect, with the variant responsible for an alternatively spliced

transcript, or a change in the protein structure resulting in loss of interaction at a binding site (Kiang et al., 2020).

In this chapter, iPSC lines from two *RDH12* patients, one with an autosomal dominant heterozygous mutation and one with an autosomal recessive biallelic mutation, have been generated. Dermal fibroblasts were reprogrammed using non integrating episomal plasmids. Reprogramming efficiency can be variable between cell lines and difficulties were initially encountered with reprogramming of the RDH12 AR line. Sodium butyrate, a small molecule inhibitor of histone deacetylases, has been shown to increase efficiency of reprogramming (Zhang et al., 2014). Addition of sodium butyrate for the first seven days of reprogramming greatly increased reprogramming efficiency of RDH12 AR fibroblasts. Characterisation of both iPSC lines revealed they expressed markers of pluripotency and displayed potential to differentiate into the three germ layers.

iPSCs can be differentiated to any cell type. Differentiation to retinal cell types was first developed in 2009 (Buchholz et al., 2009, Hirami et al., 2009), with the differentiation of iPSCs to a monolayer of RPE cells and in 2013, the first clinical trial for iPSC-RPE transplantation in a patient with AMD was carried out (Mandai et al., 2017). Studies by the Sasai lab paved the way for the generation of three-dimensional retinal organoids (Nakano et al., 2012). Although human ESCs were used, this study was pivotal in leading the way for the generation of iPSC derived retinal organoids, and a number of protocols have since been developed (Meyer et al., 2009, Zhong et al., 2014,

Reichman et al., 2014, Gonzalez-Cordero et al., 2017). Retinal organoids have been shown to recapitulate human development and display stratification of neural layer, including photoreceptor outer segments (Gonzalez-Cordero et al., 2017, Zhong et al., 2014, Nakano et al., 2012). A number of studies have utilised iPSCs from patients with RP and LCA to generate retinal organoids (Lane et al., 2020, Gao et al., 2020, Deng et al., 2018, Guo et al., 2019, Sharma et al., 2017, Dulla et al., 2018, Kruczek et al., 2021, Li et al., 2019, Lukovic et al., 2020). In a model of *RP2* X-linked RP, patient retinal organoids showed reduced rhodopsin expression and thinner ONL compared to control organoids at day 150 (Lane et al., 2020) and in organoids derived from a RP patient with *PDE6B* mutation, rhodopsin mislocalisation and an accumulation of cGMP was observed at day 230 (Gao et al., 2020). Disrupted autophagy with an accumulation of LC3-II protein expression at day 90 was observed in *TRNT1*-RP organoids (Sharma et al., 2017).

RDH12 iPSC patient lines will be used for differentiation to retinal organoids, providing a useful tool to study disease mechanisms and test drugs. According to the study by Cowan et al. (2020), expression of *RDH12* is first detected in retinal organoids at week 24, with increased expression from week 30 onwards. Treating organoids with atRAL will enable us to determine if RDH12 is functional in the wildtype organoids, and whether there is any disruption to RDH12 activity in the patient derived organoids. TUNEL staining will be used to assess cell death in the organoids, following atRAL treatment, and immunostaining for ER stress and oxidative stress markers can be used

to determine whether there is a similar disruption to the patient organoids as seen in the mutant HEK-293 cells. Transcriptomic analysis will be used to determine the underlying disease mechanisms, allowing comparison between the two disease phenotypes, in particular focussing on the disrupted pathways identified in earlier chapters, namely oxidative stress, ER stress and autophagy. Drugs identified in the HEK-293 RDH12 drug screens will be tested in the organoids.

A current limitation of retinal organoids is the inability to study the visual cycle due to the lack of RPE cells. Co-culture of retinal organoids and RPE may therefore be beneficial to study the visual cycle. The long culture times, combined with variable differentiation efficiencies between clones also present limitations in regard to generating large numbers of organoids sufficient for drug screening studies. Retinal organoid modelling is a relatively new and innovative area of research and has great potential for disease modelling and therapeutic study, however further optimisation and refinement of protocols is required to fulfil the true potential and bring us closer to personalised medicine.

7. Final Discussion

Mutations in *RDH12* are associated with severe early onset autosomal recessive LCA, and autosomal dominant RP. However, little is known about the disease mechanisms involved in retinal pathogenesis and there are currently no treatments available for *RDH12*-related retinopathies. In this thesis, I first attempted expression and purification of recombinant RDH12, however difficulties were encountered in purification and following several optimisation steps, all attempts resulted in aggregation or low yields, therefore this aim was halted. I next generated three *RDH12* disease models (1) CRISPR/Cas9 *rdh12* zebrafish mutant (2) HEK-293 cells expressing wildtype and mutant *RDH12* and (3) patient derived iPSC cell lines. These models were used for investigating disease mechanisms, identifying potential therapeutic targets, and screening of drugs.

rdh12^{u533} fish displayed a late onset rod-predominant degeneration, with defects observed in rhodopsin trafficking. In addition, early indicators of stress were detected in the adult retina, with reduced expression of autophagy and oxidative stress markers and increased phagosome size. These data indicate that the *rdh12*^{u533} fish have a reduced capacity to protect the retina from stress. HEK-293 stable cell line expressing WT RDH12 protected cells from atRAL induced toxicity and mutations in *RDH12* severely disrupted expression and activity levels of the enzyme. Lack of functional RDH12 resulted in increased levels of oxidative and ER stress.

Together, zebrafish and cell studies have indicated that oxidative stress, ER stress and autophagy pathways are disrupted in *RDH12*-retinopathies. A number of recent studies have shown that these three pathways are interlinked and disrupted in stressed RPE cells (Zhang et al., 2020, Song et al., 2020, Feng et al., 2019, Zhang et al., 2019). Under normal conditions, the UPR pathway and autophagy are activated in response to cellular stresses, such as an increase in ROS levels, as a protective mechanism. However, prolonged activation of these pathways leads to apoptosis. It was recently shown that light exposure caused oxidative stress, ER stress and autophagy in photoreceptor 661W and ARPE-19 cells. Treatment with the antioxidant NAC inhibited ER stress, indicating that ROS production triggers ER stress. In addition, inhibition of ER stress reduced autophagy and autophagy inhibition reduced light induced cell death, suggesting that the three pathways are closely linked (Song et al., 2020).

A recent study has shown the interplay between atRAL induced oxidative stress, ER stress and autophagy (Zhang et al., 2020). In ARPE-19 cells, atRAL treatment induced ROS production and increased expression of autophagy markers LC3BII, Beclin and p62 and ER stress marker CHOP. Treatment with NAC reduced expression of autophagy markers, suggesting that ROS production triggers autophagy. However, inhibition of autophagy also reduced atRAL induced ROS levels, expression of oxidative stress markers HO-1 and y-GCSh and cell death, suggesting that autophagy further enhances oxidative stress. Inhibition of ER stress with salubrinal also reduced ROS production, expression of autophagy markers, and cell death.

Inhibition of autophagy through siRNA knockdown of Beclin inhibited CHOP expression, thereby attenuating ER stress. It is clear that these pathways are closely interlinked with atRAL severely disrupting cellular homeostasis, and the effects of *RDH12* mutations on one pathway inevitably impacts other linked pathways. atRAL induces ROS generation, which triggers both ER stress and autophagy. These two processes in turn generate more ROS, eventually leading to apoptosis (**Figure 45**).

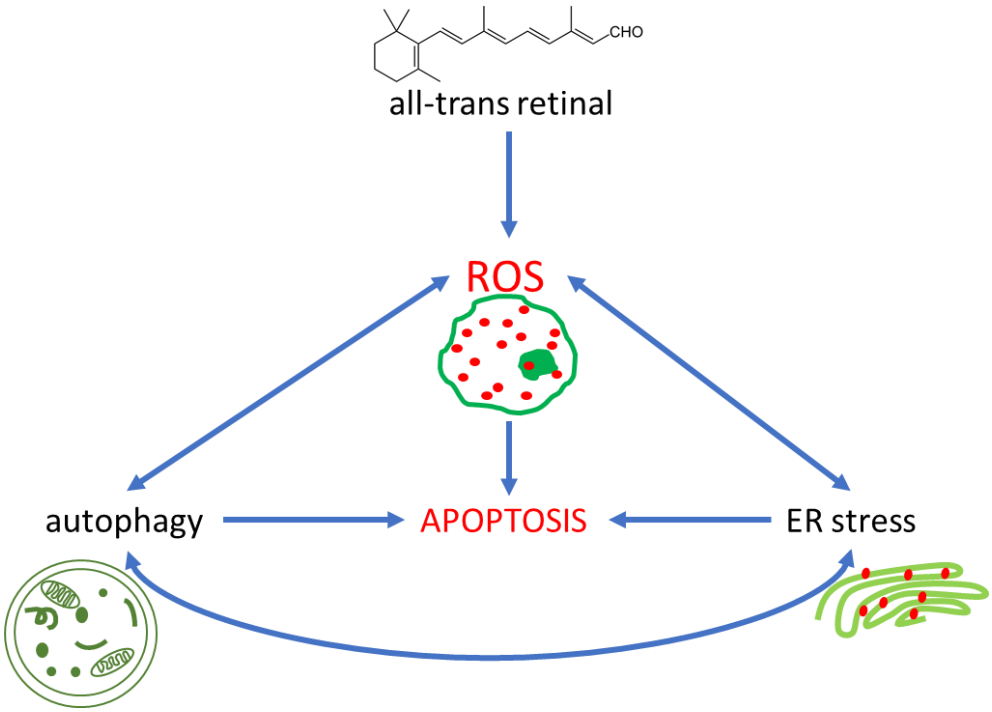

Figure 45: RDH12 disease mechanism.
Lack of functional RDH12 results in a build up of all-trans retinal, which leads to an increase in ROS, which triggers autophagy and ER stress. These two processes in turn generate more ROS, eventually leading to apoptosis. ROS; reactive oxygen species.

Therefore, it would be beneficial to investigate autophagy pathways in the *RDH12* mutant cells, by measuring autophagy flux and expression of autophagy associated genes to determine whether autophagy is disrupted. In

addition, inhibition of ER stress and autophagy would elucidate the connection between the ER stress and autophagy pathways in the *RDH12* cells. As atRAL induced ROS was found to colocalise with mitochondria (Li et al., 2015), investigation of mitochondria associated ROS production using MitoSOX staining will determine whether a similar disruption is present in the zebrafish and cell lines. In addition, mitochondrial function can be assessed using Seahorse XF analyser.

Oxidative, ER stress and autophagy pathways represent key therapeutic targets. A number of drugs were tested, and promising data was obtained with pregabalin, which reduced atRAL induced ER stress, representing a potential drug for the treatment of *RDH12*-retinopathies. atRAL build up is also implicated in the pathogenesis of Stargardt disease, which is caused by mutations in *ABCA4*, resulting in delayed clearance of atRAL. A number of drugs have been tested in Stargardt disease models, which could be repurposed for *RDH12*-retinopathies. A promising drug is emixustat, which is an RPE65 inhibitor that has been shown to reduce lipofuscin autofluorescence and A2E levels in an *Abca4*$^{-/-}$ mouse model, and protected photoreceptors from light induced damage (Bavik et al., 2015). Emixustat also contains a primary amine group, similar to pregabalin, which can combine with atRAL, reducing the amount of free atRAL in the retina (Zhang et al., 2015). Phase 2 clinical trials in patients with macular atrophy secondary to Stargardt showed near complete suppression of rod b-wave recovery rate after photobleaching (Kubota et al., 2020). Emixustat is currently in phase 3 clinical trials (NCT03772665) and would be a good drug

to test in RDH12 models, as it targets excess atRAL. HEK293 cell lines can be dosed with atRAL and emixustat, and its protective effects can be determined by measuring cell viability, ER stress, oxidative stress, levels of atRAL and autophagy. A number of other drugs have been described in models of Stargardt disease, including Remofuscin, which was shown to reduce lipofuscin from human and *Abca4*$^{-/-}$ mouse RPE cells (Julien et al., 2010, Fang et al., 2017) and Raloxifene, which protected *Abca4*$^{-/-}$*Rdh8*$^{-/-}$ mice from light induced damage (Getter et al., 2019). Antioxidants are also an important class of drugs that can be exploited for *RDH12*-reitnopathies, as oxidative stress appears to be the initial stressor, which triggers ER stress and autophagy induced cell death. The disease mechanism observed in the *RDH12* models, namely oxidative and ER stress, are common to a number of IRDs (Domènech and Marfany, 2020, Griciuc et al., 2011), therefore any drugs identified in these models may be applicable to similar conditions caused by defects in other visual cycle genes.

Finally, I generated patient derived iPSC lines from two patients. Patient derived iPSC lines are an extremely valuable resource for the study of retinal dystrophies, as diseased retinal tissue is difficult to obtain. These iPSC lines will be used for differentiation to retinal organoids. As previous mouse and the current zebrafish study has revealed, animal models do not always recapitulate the phenotype observed in patients, therefore retinal organoids represent a useful model to study disease mechanisms in a human system. Patient derived retinal organoids have been shown to recapitulate disease phenotypes, providing a useful tool to study disease mechanisms and test

drugs. However, one of the current limitations of retinal organoids is the inability to study the visual cycle due to the lack of RPE cells. Co-culture of retinal organoids and RPE may therefore be useful for the study of the visual cycle. Disrupted pathways identified in this thesis will be investigated in the retinal organoids and any promising drugs will also be tested in the organoids.

In addition, I reported a novel variant associated with late onset mild autosomal dominant RP. To date, only three *RDH12* heterozygous variants associated with autosomal dominant RP have been identified. Next generation sequencing technologies have accelerated the identification of novel variants and genes responsible for IRDs. Techniques like whole genome sequencing are being used more routinely, enabling better identification of patients. Further natural history and deep phenotyping studies are needed to identify genotype-phenotype correlations.

It would be of great interest to study the differences in disease mechanisms caused by autosomal recessive and autosomal dominant variants, considering the stark difference in age of onset and phenotype severity. The generation of iPSC lines from two patients with differing *RDH12*-retinopathies will facilitate this study in retinal organoids through the use of transcriptomic and proteomic analyses.

Gene therapy is one of the most promising therapies for IRDs. In gene therapy, a wildtype copy of the mutated gene is delivered to the retina in a

viral vector, via intravitreal or subretinal injection, where it is then translated to produce a functional protein. With the success of Luxturna, a gene therapy for LCA caused by mutations in *RPE65*, also a visual cycle gene, there is promise for other IRDs. *RDH12* is a good candidate for gene therapy and zebrafish and patient derived retinal organoids are useful models to aid in the development of *RDH12* gene therapy.

In conclusion, I have generated a number of *RDH12* models, which has revealed a deeper understanding of *RDH12* disease mechanisms and identified potential therapeutic targets. These models provide a valuable resource for further study into *RDH12*-related retinopathies and the development of novel therapies.

References

RetNet: The Retinal Information Network [Online]. Available: https://sph.uth.edu/retnet/home.htm [Accessed 8/9/21].

ABARGHOOI KAHAKI, F., MONZAVI, S., BAMEHR, H., BANDANI, E., PAYANDEH, Z., JAHANGIRI, A. & KHALILI, S. 2020. Expression and Purification of Membrane Proteins in Different Hosts. *International Journal of Peptide Research and Therapeutics,* 26**,** 2077-2087.

ADAMS, C. J., KOPP, M. C., LARBURU, N., NOWAK, P. R. & ALI, M. M. U. 2019. Structure and Molecular Mechanism of ER Stress Signaling by the Unfolded Protein Response Signal Activator IRE1. *Front Mol Biosci,* 6**,** 11.

ALDINI, G., ALTOMARE, A., BARON, G., VISTOLI, G., CARINI, M., BORSANI, L. & SERGIO, F. 2018. N-Acetylcysteine as an antioxidant and disulphide breaking agent: the reasons why. *Free Radical Research,* 52**,** 751-762.

ALEMAN, T. S., UYHAZI, K. E., SERRANO, L. W., VASIREDDY, V., BOWMAN, S. J., AMMAR, M. J., PEARSON, D. J., MAGUIRE, A. M. & BENNETT, J. 2018. RDH12 Mutations Cause a Severe Retinal Degeneration With Relatively Spared Rod Function. *Invest Ophthalmol Vis Sci,* 59**,** 5225-5236.

ALHASANI, R. H., ALMARHOUN, M., ZHOU, X., REILLY, J., PATTERSON, S., ZENG, Z. & SHU, X. 2020. Tauroursodeoxycholic Acid Protects Retinal Pigment Epithelial Cells from Oxidative Injury and Endoplasmic Reticulum Stress In Vitro. *Biomedicines,* 8.

ALI, S. A., ZAITONE, S. A., DESSOUKI, A. A. & ALI, A. A. 2019. Pregabalin affords retinal neuroprotection in diabetic rats: Suppression of retinal glutamate, microglia cell expression and apoptotic cell death. *Exp Eye Res,* 184**,** 78-90.

AMER, J., ATLAS, D. & FIBACH, E. 2008. N-acetylcysteine amide (AD4) attenuates oxidative stress in beta-thalassemia blood cells. *Biochimica et Biophysica Acta (BBA) - General Subjects,* 1780**,** 249-255.

AVILA-FERNANDEZ, A., CANTALAPIEDRA, D., ALLER, E., VALLESPIN, E., AGUIRRE-LAMBAN, J., BLANCO-KELLY, F., CORTON, M., RIVEIRO-ALVAREZ, R., ALLIKMETS, R., TRUJILLO-TIEBAS, M. J., MILLAN, J. M., CREMERS, F. P. & AYUSO, C. 2010. Mutation analysis of 272 Spanish families affected by autosomal recessive retinitis pigmentosa using a genotyping microarray. *Mol Vis,* 16**,** 2550-8.

BAKER, S. A. & KEROV, V. 2013. Photoreceptor Inner and Outer Segments. Elsevier.

BAVIK, C., HENRY, S. H., ZHANG, Y., MITTS, K., MCGINN, T., BUDZYNSKI, E., PASHKO, A., LIEU, K. L., ZHONG, S., BLUMBERG, B., KUKSA, V., ORME, M., SCOTT, I., FAWZI, A. & KUBOTA, R. 2015. Visual Cycle Modulation as an Approach toward Preservation of Retinal Integrity. *PloS one,* 10**,** e0124940-e0124940.

BELYAEVA, O. V., KORKINA, O. V., STETSENKO, A. V., KIM, T., NELSON, P. S. & KEDISHVILI, N. Y. 2005. Biochemical properties of purified human retinol dehydrogenase 12 (RDH12): catalytic efficiency toward retinoids and C9 aldehydes and effects of cellular retinol-binding protein type I (CRBPI) and cellular retinaldehyde-binding protein (CRALBP) on the oxidation and reduction of retinoids. *Biochemistry,* 44**,** 7035-47.

BENAYOUN, L., SPIEGEL, R., AUSLENDER, N., ABBASI, A. H., RIZEL, L., HUJEIRAT, Y., SALAMA, I., GARZOZI, H. J., ALLON-SHALEV, S. & BEN-YOSEF, T. 2009. Genetic heterogeneity in two consanguineous families segregating early onset retinal degeneration: the pitfalls of homozygosity mapping. *Am J Med Genet A,* 149a**,** 650-6.

BERROW, N. S., ALDERTON, D., SAINSBURY, S., NETTLESHIP, J., ASSENBERG, R., RAHMAN, N., STUART, D. I. & OWENS, R. J. 2007. A versatile ligation-independent cloning

method suitable for high-throughput expression screening applications. *Nucleic Acids Res,* 35**,** e45.

BIAN, J., CHEN, H., SUN, J., CAO, Y., AN, J., PAN, Q. & QI, M. 2021. Gene Therapy for Rdh12-Associated Retinal Diseases Helps to Delay Retinal Degeneration and Vision Loss. *Drug Des Devel Ther,* 15**,** 3581-3591.

BROGNA, S. & WEN, J. 2009. Nonsense-mediated mRNA decay (NMD) mechanisms. *Nature Structural & Molecular Biology,* 16**,** 107-113.

BROWN, E. E., DEWEERD, A. J., ILDEFONSO, C. J., LEWIN, A. S. & ASH, J. D. 2019. Mitochondrial oxidative stress in the retinal pigment epithelium (RPE) led to metabolic dysfunction in both the RPE and retinal photoreceptors. *Redox Biology,* 24**,** 101201.

BUCHHOLZ, D. E., HIKITA, S. T., ROWLAND, T. J., FRIEDRICH, A. M., HINMAN, C. R., JOHNSON, L. V. & CLEGG, D. O. 2009. Derivation of functional retinal pigmented epithelium from induced pluripotent stem cells. *Stem Cells,* 27**,** 2427-34.

BUENDIA, I., MICHALSKA, P., NAVARRO, E., GAMEIRO, I., EGEA, J. & LEÓN, R. 2016. Nrf2-ARE pathway: An emerging target against oxidative stress and neuroinflammation in neurodegenerative diseases. *Pharmacol Ther,* 157**,** 84-104.

CHEN, C., THOMPSON, D. A. & KOUTALOS, Y. 2012a. Reduction of all-trans-retinal in vertebrate rod photoreceptors requires the combined action of RDH8 and RDH12. *J Biol Chem,* 287**,** 24662-70.

CHEN, Y., OKANO, K., MAEDA, T., CHAUHAN, V., GOLCZAK, M., MAEDA, A. & PALCZEWSKI, K. 2012b. Mechanism of All-trans-retinal Toxicity with Implications for Stargardt Disease and Age-related Macular Degeneration. *Journal of Biological Chemistry,* 287**,** 5059-5069.

CHETYRKIN, S. V., HU, J., GOUGH, W. H., DUMAUAL, N. & KEDISHVILI, N. Y. 2001. Further characterization of human microsomal 3alpha-hydroxysteroid dehydrogenase. *Arch Biochem Biophys,* 386**,** 1-10.

CHONG, W. C., SHASTRI, M. D. & ERI, R. 2017. Endoplasmic Reticulum Stress and Oxidative Stress: A Vicious Nexus Implicated in Bowel Disease Pathophysiology. *International journal of molecular sciences,* 18**,** 771.

CHRISPELL, J. D., FEATHERS, K. L., KANE, M. A., KIM, C. Y., BROOKS, M., KHANNA, R., KURTH, I., HUBNER, C. A., GAL, A., MEARS, A. J., SWAROOP, A., NAPOLI, J. L., SPARROW, J. R. & THOMPSON, D. A. 2009. Rdh12 activity and effects on retinoid processing in the murine retina. *J Biol Chem,* 284**,** 21468-77.

COLLERY, R., MCLOUGHLIN, S., VENDRELL, V., FINNEGAN, J., CRABB, J. W., SAARI, J. C. & KENNEDY, B. N. 2008. Duplication and divergence of zebrafish CRALBP genes uncovers novel role for RPE- and Muller-CRALBP in cone vision. *Invest Ophthalmol Vis Sci,* 49**,** 3812-20.

COPPIETERS, F., VAN SCHIL, K., BAUWENS, M., VERDIN, H., DE JAEGHER, A., SYX, D., SANTE, T., LEFEVER, S., ABDELMOULA, N. B., DEPASSE, F., CASTEELS, I., DE RAVEL, T., MEIRE, F., LEROY, B. P. & DE BAERE, E. 2014. Identity-by-descent-guided mutation analysis and exome sequencing in consanguineous families reveals unusual clinical and molecular findings in retinal dystrophy. *Genet Med,* 16**,** 671-80.

COSTARIDIS, P., HORTON, C., ZEITLINGER, J., HOLDER, N. & MADEN, M. 1996. Endogenous retinoids in the zebrafish embryo and adult. *Dev Dyn,* 205**,** 41-51.

COWAN, C. S., RENNER, M., DE GENNARO, M., GROSS-SCHERF, B., GOLDBLUM, D., HOU, Y., MUNZ, M., RODRIGUES, T. M., KROL, J., SZIKRA, T., CUTTAT, R., WALDT, A., PAPASAIKAS, P., DIGGELMANN, R., PATINO-ALVAREZ, C. P., GALLIKER, P., SPIRIG, S. E., PAVLINIC, D., GERBER-HOLLBACH, N., SCHUIERER, S., SRDANOVIC, A., BALOGH, M., PANERO, R., KUSNYERIK, A., SZABO, A., STADLER, M. B., ORGÜL, S., PICELLI, S., HASLER, P. W., HIERLEMANN, A., SCHOLL, H. P. N., ROMA, G., NIGSCH, F. & ROSKA,

B. 2020. Cell Types of the Human Retina and Its Organoids at Single-Cell Resolution. *Cell,* 182**,** 1623-1640.e34.
CREMERS, F. P. M., BOON, C. J. F., BUJAKOWSKA, K. & ZEITZ, C. 2018. Special Issue Introduction: Inherited Retinal Disease: Novel Candidate Genes, Genotype-Phenotype Correlations, and Inheritance Models. *Genes,* 9**,** 215.
CROSS, A. L., VISWANATH, O. & SHERMAN, A. L. 2021. Pregabalin. *StatPearls.* Treasure Island (FL): StatPearls Publishing

Copyright © 2021, StatPearls Publishing LLC.

DENG, W. L., GAO, M. L., LEI, X. L., LV, J. N., ZHAO, H., HE, K. W., XIA, X. X., LI, L. Y., CHEN, Y. C., LI, Y. P., PAN, D., XUE, T. & JIN, Z. B. 2018. Gene Correction Reverses Ciliopathy and Photoreceptor Loss in iPSC-Derived Retinal Organoids from Retinitis Pigmentosa Patients. *Stem Cell Reports,* 10**,** 2005.
DOMÈNECH, E. B. & MARFANY, G. 2020. The Relevance of Oxidative Stress in the Pathogenesis and Therapy of Retinal Dystrophies. *Antioxidants (Basel),* 9.
DONA, M., SLIJKERMAN, R., LERNER, K., BROEKMAN, S., WEGNER, J., HOWAT, T., PETERS, T., HETTERSCHIJT, L., BOON, N., DE VRIEZE, E., SORUSCH, N., WOLFRUM, U., KREMER, H., NEUHAUSS, S., ZANG, J., KAMERMANS, M., WESTERFIELD, M., PHILLIPS, J. & VAN WIJK, E. 2018. Usherin defects lead to early-onset retinal dysfunction in zebrafish. *Experimental eye research,* 173**,** 148-159.
DONDAPATI, S. K., STECH, M., ZEMELLA, A. & KUBICK, S. 2020. Cell-Free Protein Synthesis: A Promising Option for Future Drug Development. *BioDrugs,* 34**,** 327-348.
DULLA, K., AGUILA, M., LANE, A., JOVANOVIC, K., PARFITT, D. A., SCHULKENS, I., CHAN, H. L., SCHMIDT, I., BEUMER, W., VORTHOREN, L., COLLIN, R. W. J., GARANTO, A., DUIJKERS, L., BRUGULAT-PANES, A., SEMO, M. A., VUGLER, A. A., BIASUTTO, P., ADAMSON, P. & CHEETHAM, M. E. 2018. Splice-Modulating Oligonucleotide QR-110 Restores CEP290 mRNA and Function in Human c.2991+1655A>G LCA10 Models. *Molecular Therapy - Nucleic Acids,* 12**,** 730-740.
FAHIM, A. T., BOUZIA, Z., BRANHAM, K. H., KUMARAN, N., VARGAS, M. E., FEATHERS, K. L., PERERA, N. D., YOUNG, K., KHAN, N. W., HECKENLIVELY, J. R., WEBSTER, A. R., PENNESI, M. E., ALI, R. R., THOMPSON, D. A. & MICHAELIDES, M. 2019. Detailed clinical characterisation, unique features and natural history of autosomal recessive RDH12-associated retinal degeneration. *Br J Ophthalmol*.
FANG, Y., TSCHULAKOW, A., TIKHONOVICH, M., TAUBITZ, T., ILLING, B., SCHULTHEISS, S., SCHRAERMEYER, U. & JULIEN-SCHRAERMEYER, S. 2017. Preclinical results of a new pharmacological therapy approach for Stargardt disease and dry age-related macular degeneration. *Investigative Ophthalmology & Visual Science,* 58**,** 256-256.
FENG, J., CHEN, Y., LU, B., SUN, X., ZHU, H. & SUN, X. 2019. Autophagy activated via GRP78 to alleviate endoplasmic reticulum stress for cell survival in blue light-mediated damage of A2E-laden RPEs. *BMC Ophthalmology,* 19**,** 249.
FINGERT, J. H., OH, K., CHUNG, M., SCHEETZ, T. E., ANDORF, J. L., JOHNSON, R. M., SHEFFIELD, V. C. & STONE, E. M. 2008. Association of a novel mutation in the retinol dehydrogenase 12 (RDH12) gene with autosomal dominant retinitis pigmentosa. *Arch Ophthalmol,* 126**,** 1301-7.
FLEISCH, V. C., SCHONTHALER, H. B., VON LINTIG, J. & NEUHAUSS, S. C. 2008. Subfunctionalization of a retinoid-binding protein provides evidence for two parallel visual cycles in the cone-dominant zebrafish retina. *J Neurosci,* 28**,** 8208-16.
FRANCIS, D. M. & PAGE, R. 2010. Strategies to optimize protein expression in E. coli. *Current protocols in protein science,* Chapter 5**,** 5241-5.24.29.
GAGNON, J. A., VALEN, E., THYME, S. B., HUANG, P., AKHMETOVA, L., PAULI, A., MONTAGUE, T. G., ZIMMERMAN, S., RICHTER, C. & SCHIER, A. F. 2014. Efficient

mutagenesis by Cas9 protein-mediated oligonucleotide insertion and large-scale assessment of single-guide RNAs. *PLoS One,* 9**,** e98186.

GAO, M. L., LEI, X. L., HAN, F., HE, K. W., JIN, S. Q., ZHANG, Y. Y. & JIN, Z. B. 2020. Patient-Specific Retinal Organoids Recapitulate Disease Features of Late-Onset Retinitis Pigmentosa. *Front Cell Dev Biol,* 8**,** 128.

GARG, A., LEE, W., SENGILLO, J. D., ALLIKMETS, R., GARG, K. & TSANG, S. H. 2017. Peripapillary sparing in RDH12-associated Leber congenital amaurosis. *Ophthalmic Genet,* 38**,** 575-579.

GETTER, T., SUH, S., HOANG, T., HANDA, J. T., DONG, Z., MA, X., CHEN, Y., BLACKSHAW, S. & PALCZEWSKI, K. 2019. The selective estrogen receptor modulator raloxifene mitigates the effect of all-trans-retinal toxicity in photoreceptor degeneration. *J Biol Chem,* 294**,** 9461-9475.

GLASS, A. S. & DAHM, R. 2004. The zebrafish as a model organism for eye development. *Ophthalmic Res,* 36**,** 4-24.

GONZALEZ-CORDERO, A., KRUCZEK, K., NAEEM, A., FERNANDO, M., KLOC, M., RIBEIRO, J., GOH, D., DURAN, Y., BLACKFORD, S. J. I., ABELLEIRA-HERVAS, L., SAMPSON, R. D., SHUM, I. O., BRANCH, M. J., GARDNER, P. J., SOWDEN, J. C., BAINBRIDGE, J. W. B., SMITH, A. J., WEST, E. L., PEARSON, R. A. & ALI, R. R. 2017. Recapitulation of Human Retinal Development from Human Pluripotent Stem Cells Generates Transplantable Populations of Cone Photoreceptors. *Stem Cell Reports,* 9**,** 820-837.

GRICIUC, A., ARON, L. & UEFFING, M. 2011. ER stress in retinal degeneration: a target for rational therapy? *Trends Mol Med,* 17**,** 442-51.

GULANI, A. & WEILER, T. 2021. Genetics, Autosomal Recessive. *StatPearls.* Treasure Island (FL): StatPearls Publishing

Copyright © 2021, StatPearls Publishing LLC.

GUO, Y., WANG, P., MA, J. H., CUI, Z., YU, Q., LIU, S., XUE, Y., ZHU, D., CAO, J., LI, Z., TANG, S. & CHEN, J. 2019. Modeling Retinitis Pigmentosa: Retinal Organoids Generated From the iPSCs of a Patient With the USH2A Mutation Show Early Developmental Abnormalities. *Front Cell Neurosci,* 13**,** 361.

HAESELEER, F., JANG, G. F., IMANISHI, Y., DRIESSEN, C., MATSUMURA, M., NELSON, P. S. & PALCZEWSKI, K. 2002. Dual-substrate specificity short chain retinol dehydrogenases from the vertebrate retina. *J Biol Chem,* 277**,** 45537-45546.

HIRAMI, Y., OSAKADA, F., TAKAHASHI, K., OKITA, K., YAMANAKA, S., IKEDA, H., YOSHIMURA, N. & TAKAHASHI, M. 2009. Generation of retinal cells from mouse and human induced pluripotent stem cells. *Neurosci Lett,* 458**,** 126-31.

HOFMANN, L., TSYBOVSKY, Y., ALEXANDER, N. S., BABINO, D., LEUNG, N. Y., MONTELL, C., BANERJEE, S., VON LINTIG, J. & PALCZEWSKI, K. 2016. Structural Insights into the Drosophila melanogaster Retinol Dehydrogenase, a Member of the Short-Chain Dehydrogenase/Reductase Family. *Biochemistry,* 55**,** 6545-6557.

HOON, M., OKAWA, H., DELLA SANTINA, L. & WONG, R. O. L. 2014. Functional architecture of the retina: Development and disease. *Progress in Retinal and Eye Research,* 42**,** 44-84.

HOWE, K., CLARK, M. D., TORROJA, C. F., TORRANCE, J., BERTHELOT, C., MUFFATO, M., COLLINS, J. E., HUMPHRAY, S., MCLAREN, K., MATTHEWS, L., MCLAREN, S., SEALY, I., CACCAMO, M., CHURCHER, C., SCOTT, C., BARRETT, J. C., KOCH, R., RAUCH, G. J., WHITE, S., CHOW, W., KILIAN, B., QUINTAIS, L. T., GUERRA-ASSUNCAO, J. A., ZHOU, Y., GU, Y., YEN, J., VOGEL, J. H., EYRE, T., REDMOND, S., BANERJEE, R., CHI, J., FU, B., LANGLEY, E., MAGUIRE, S. F., LAIRD, G. K., LLOYD, D., KENYON, E., DONALDSON, S., SEHRA, H., ALMEIDA-KING, J., LOVELAND, J., TREVANION, S., JONES, M., QUAIL, M., WILLEY, D., HUNT, A., BURTON, J., SIMS, S., MCLAY, K., PLUMB, B., DAVIS, J., CLEE, C., OLIVER, K., CLARK, R., RIDDLE, C., ELLIOT, D., THREADGOLD, G., HARDEN, G.,

WARE, D., BEGUM, S., MORTIMORE, B., KERRY, G., HEATH, P., PHILLIMORE, B., TRACEY, A., CORBY, N., DUNN, M., JOHNSON, C., WOOD, J., CLARK, S., PELAN, S., GRIFFITHS, G., SMITH, M., GLITHERO, R., HOWDEN, P., BARKER, N., LLOYD, C., STEVENS, C., HARLEY, J., HOLT, K., PANAGIOTIDIS, G., LOVELL, J., BEASLEY, H., HENDERSON, C., GORDON, D., AUGER, K., WRIGHT, D., COLLINS, J., RAISEN, C., DYER, L., LEUNG, K., ROBERTSON, L., AMBRIDGE, K., LEONGAMORNLERT, D., MCGUIRE, S., GILDERTHORP, R., GRIFFITHS, C., MANTHRAVADI, D., NICHOL, S., BARKER, G., et al. 2013. The zebrafish reference genome sequence and its relationship to the human genome. *Nature,* 496**,** 498-503.

HU, J. & NG, P. C. 2013. SIFT Indel: predictions for the functional effects of amino acid insertions/deletions in proteins. *PLoS One,* 8**,** e77940.

JANECKE, A. R., THOMPSON, D. A., UTERMANN, G., BECKER, C., HUBNER, C. A., SCHMID, E., MCHENRY, C. L., NAIR, A. R., RUSCHENDORF, F., HECKENLIVELY, J., WISSINGER, B., NURNBERG, P. & GAL, A. 2004. Mutations in RDH12 encoding a photoreceptor cell retinol dehydrogenase cause childhood-onset severe retinal dystrophy. *Nat Genet,* 36**,** 850-4.

JULIEN, S., BIESEMEIER, A., HEIDUSCHKA, P., RITTGARN, M., SCHULTHEISS, S., WINKLER, E., HOFMEISTER, S. & SCHRAERMEYER, U. 2010. Lipofuscin Can Be Eliminated From Retinal Pigment Epithelium After Drug Treatment. *Investigative Ophthalmology & Visual Science,* 51**,** 481-481.

JUSTILIEN, V., PANG, J. J., RENGANATHAN, K., ZHAN, X., CRABB, J. W., KIM, S. R., SPARROW, J. R., HAUSWIRTH, W. W. & LEWIN, A. S. 2007. SOD2 knockdown mouse model of early AMD. *Invest Ophthalmol Vis Sci,* 48**,** 4407-20.

KELLER, B. & ADAMSKI, J. 2007. RDH12, a retinol dehydrogenase causing Leber's congenital amaurosis, is also involved in steroid metabolism. *J Steroid Biochem Mol Biol,* 104**,** 190-4.

KELLEY, L. A., MEZULIS, S., YATES, C. M., WASS, M. N. & STERNBERG, M. J. 2015. The Phyre2 web portal for protein modeling, prediction and analysis. *Nat Protoc,* 10**,** 845-58.

KEVANY, B. M. & PALCZEWSKI, K. 2010. Phagocytosis of Retinal Rod and Cone Photoreceptors. *Physiology,* 25**,** 8-15.

KIANG, A.-S., KENNA, P. F., HUMPHRIES, M. M., OZAKI, E., KOENEKOOP, R. K., CAMPBELL, M., FARRAR, G. J. & HUMPHRIES, P. 2020. Properties and Therapeutic Implications of an Enigmatic D477G RPE65 Variant Associated with Autosomal Dominant Retinitis Pigmentosa. *Genes,* 11**,** 1420.

KIM, J.-Y., ZHAO, H., MARTINEZ, J., DOGGETT, T. A., KOLESNIKOV, A. V., TANG, P. H., ABLONCZY, Z., CHAN, C.-C., ZHOU, Z., GREEN, D. R. & FERGUSON, T. A. 2013. Noncanonical autophagy promotes the visual cycle. *Cell,* 154**,** 365-376.

KRUCZEK, K., QU, Z., GENTRY, J., FADL, B. R., GIESER, L., HIRIYANNA, S., BATZ, Z., SAMANT, M., SAMANTA, A., CHU, C. J., CAMPELLO, L., BROOKS, B. P., WU, Z. & SWAROOP, A. 2021. Gene Therapy of Dominant CRX-Leber Congenital Amaurosis using Patient Stem Cell-Derived Retinal Organoids. *Stem Cell Reports,* 16**,** 252-263.

KUBOTA, R., BIRCH, D. G., GREGORY, J. K. & KOESTER, J. M. 2020. Randomised study evaluating the pharmacodynamics of emixustat hydrochloride in subjects with macular atrophy secondary to Stargardt disease. *British Journal of Ophthalmology***,** bjophthalmol-2020-317712.

KUMARAN, N., MOORE, A. T., WELEBER, R. G. & MICHAELIDES, M. 2017. Leber congenital amaurosis/early-onset severe retinal dystrophy: clinical features, molecular genetics and therapeutic interventions. *Br J Ophthalmol,* 101**,** 1147-1154.

KURTH, I., THOMPSON, D. A., RUTHER, K., FEATHERS, K. L., CHRISPELL, J. D., SCHROTH, J., MCHENRY, C. L., SCHWEIZER, M., SKOSYRSKI, S., GAL, A. & HUBNER, C. A. 2007.

Targeted disruption of the murine retinal dehydrogenase gene Rdh12 does not limit visual cycle function. *Mol Cell Biol,* 27**,** 1370-9.
KUSACZUK, M. 2019. Tauroursodeoxycholate-Bile Acid with Chaperoning Activity: Molecular and Cellular Effects and Therapeutic Perspectives. *Cells,* 8.
LANE, A., JOVANOVIC, K., SHORTALL, C., OTTAVIANI, D., PANES, A. B., SCHWARZ, N., GUARASCIO, R., HAYES, M. J., PALFI, A., CHADDERTON, N., FARRAR, G. J., HARDCASTLE, A. J. & CHEETHAM, M. E. 2020. Modeling and Rescue of RP2 Retinitis Pigmentosa Using iPSC-Derived Retinal Organoids. *Stem Cell Reports,* 15**,** 67-79.
LEE, J. H., YOON, Y. M. & LEE, S. H. 2019. TUDCA-Treated Mesenchymal Stem Cells Protect against ER Stress in the Hippocampus of a Murine Chronic Kidney Disease Model. *Int J Mol Sci,* 20.
LEE, S. A., BELYAEVA, O. V. & KEDISHVILI, N. Y. 2008. Effect of lipid peroxidation products on the activity of human retinol dehydrogenase 12 (RDH12) and retinoid metabolism. *Biochim Biophys Acta,* 1782**,** 421-5.
LEE, S. A., BELYAEVA, O. V. & KEDISHVILI, N. Y. 2010. Disease-associated variants of microsomal retinol dehydrogenase 12 (RDH12) are degraded at mutant-specific rates. *FEBS Lett,* 584**,** 507-10.
LEE, S. A., BELYAEVA, O. V., POPOV, I. K. & KEDISHVILI, N. Y. 2007. Overproduction of bioactive retinoic acid in cells expressing disease-associated mutants of retinol dehydrogenase 12. *J Biol Chem,* 282**,** 35621-8.
LEE, S. Y., USUI, S., ZAFAR, A. B., OVESON, B. C., JO, Y. J., LU, L., MASOUDI, S. & CAMPOCHIARO, P. A. 2011. N-Acetylcysteine promotes long-term survival of cones in a model of retinitis pigmentosa. *J Cell Physiol,* 226**,** 1843-9.
LEWIS, R. G. & SIMPSON, B. 2021. Genetics, Autosomal Dominant. *StatPearls.* Treasure Island (FL): StatPearls Publishing

Copyright © 2021, StatPearls Publishing LLC.

LI, G., GAO, G., WANG, P., SONG, X., XU, P., XIE, B., ZHOU, T., PAN, G., PENG, F., ZHANG, Q., GE, J. & ZHONG, X. 2019. Generation and Characterization of Induced Pluripotent Stem Cells and Retinal Organoids From a Leber's Congenital Amaurosis Patient With Novel RPE65 Mutations. *Front Mol Neurosci,* 12**,** 212.
LI, J., CAI, X., XIA, Q., YAO, K., CHEN, J., ZHANG, Y., NARANMANDURA, H., LIU, X. & WU, Y. 2015. Involvement of Endoplasmic Reticulum Stress in All-Trans-Retinal-Induced Retinal Pigment Epithelium Degeneration. *Toxicological Sciences,* 143**,** 196-208.
LI, Y., PAN, Q. & GU, Y. S. 2017. Phenotype-genotype correlation with Sanger sequencing identified retinol dehydrogenase 12 (RDH12) compound heterozygous variants in a Chinese family with Leber congenital amaurosis. *J Zhejiang Univ Sci B,* 18**,** 421-429.
LIDEN, M., TRYGGVASON, K. & ERIKSSON, U. 2003. Structure and function of retinol dehydrogenases of the short chain dehydrogenase/reductase family. *Mol Aspects Med,* 24**,** 403-9.
LIN, J. H., WALTER, P. & YEN, T. S. 2008. Endoplasmic reticulum stress in disease pathogenesis. *Annu Rev Pathol,* 3**,** 399-425.
LUKOVIC, D., ARTERO CASTRO, A., KAYA, K. D., MUNEZERO, D., GIESER, L., DAVÓ-MARTÍNEZ, C., CORTON, M., CUENCA, N., SWAROOP, A., RAMAMURTHY, V., AYUSO, C. & ERCEG, S. 2020. Retinal Organoids derived from hiPSCs of an AIPL1-LCA Patient Maintain Cytoarchitecture despite Reduced levels of Mutant AIPL1. *Sci Rep,* 10**,** 5426.
MACKAY, D. S., DEV BORMAN, A., MORADI, P., HENDERSON, R. H., LI, Z., WRIGHT, G. A., WASEEM, N., GANDRA, M., THOMPSON, D. A., BHATTACHARYA, S. S., HOLDER, G. E., WEBSTER, A. R. & MOORE, A. T. 2011. RDH12 retinopathy: novel mutations and phenotypic description. *Mol Vis,* 17**,** 2706-16.

MAEDA, A., GOLCZAK, M., CHEN, Y., OKANO, K., KOHNO, H., SHIOSE, S., ISHIKAWA, K., HARTE, W., PALCZEWSKA, G., MAEDA, T. & PALCZEWSKI, K. 2011. Primary amines protect against retinal degeneration in mouse models of retinopathies. *Nat Chem Biol,* 8**,** 170-8.

MAEDA, A., MAEDA, T., IMANISHI, Y., SUN, W., JASTRZEBSKA, B., HATALA, D. A., WINKENS, H. J., HOFMANN, K. P., JANSSEN, J. J., BAEHR, W., DRIESSEN, C. A. & PALCZEWSKI, K. 2006. Retinol dehydrogenase (RDH12) protects photoreceptors from light-induced degeneration in mice. *J Biol Chem,* 281**,** 37697-704.

MAEDA, A., MAEDA, T., SUN, W., ZHANG, H., BAEHR, W. & PALCZEWSKI, K. 2007. Redundant and unique roles of retinol dehydrogenases in the mouse retina. *Proc Natl Acad Sci U S A,* 104**,** 19565-70.

MALIK, N. & RAO, M. S. 2013. A review of the methods for human iPSC derivation. *Methods Mol Biol,* 997**,** 23-33.

MANDAI, M., WATANABE, A., KURIMOTO, Y., HIRAMI, Y., MORINAGA, C., DAIMON, T., FUJIHARA, M., AKIMARU, H., SAKAI, N., SHIBATA, Y., TERADA, M., NOMIYA, Y., TANISHIMA, S., NAKAMURA, M., KAMAO, H., SUGITA, S., ONISHI, A., ITO, T., FUJITA, K., KAWAMATA, S., GO, M. J., SHINOHARA, C., HATA, K. I., SAWADA, M., YAMAMOTO, M., OHTA, S., OHARA, Y., YOSHIDA, K., KUWAHARA, J., KITANO, Y., AMANO, N., UMEKAGE, M., KITAOKA, F., TANAKA, A., OKADA, C., TAKASU, N., OGAWA, S., YAMANAKA, S. & TAKAHASHI, M. 2017. Autologous Induced Stem-Cell-Derived Retinal Cells for Macular Degeneration. *N Engl J Med,* 376**,** 1038-1046.

MARCHETTE, L. D., THOMPSON, D. A., KRAVTSOVA, M., NGANSOP, T. N., MANDAL, M. N. & KASUS-JACOBI, A. 2010. Retinol dehydrogenase 12 detoxifies 4-hydroxynonenal in photoreceptor cells. *Free Radic Biol Med,* 48**,** 16-25.

MARCHETTI, P. M. & BARTH, J. H. 2013. Clinical biochemistry of dihydrotestosterone. *Ann Clin Biochem,* 50**,** 95-107.

MARTINEZ, J., MALIREDDI, R. K., LU, Q., CUNHA, L. D., PELLETIER, S., GINGRAS, S., ORCHARD, R., GUAN, J. L., TAN, H., PENG, J., KANNEGANTI, T. D., VIRGIN, H. W. & GREEN, D. R. 2015. Molecular characterization of LC3-associated phagocytosis reveals distinct roles for Rubicon, NOX2 and autophagy proteins. *Nat Cell Biol,* 17**,** 893-906.

MASTRONARDE, D. N. 2003. SerialEM: A program for automated tilt series acquisition on Tecnai microscopes using prediction of specimen position. *Microscopy and Microanalysis,* 9**,** 1182-1183.

MCLAREN, W., GIL, L., HUNT, S. E., RIAT, H. S., RITCHIE, G. R., THORMANN, A., FLICEK, P. & CUNNINGHAM, F. 2016. The Ensembl Variant Effect Predictor. *Genome Biol,* 17**,** 122.

MEYER, J. S., SHEARER, R. L., CAPOWSKI, E. E., WRIGHT, L. S., WALLACE, K. A., MCMILLAN, E. L., ZHANG, S. C. & GAMM, D. M. 2009. Modeling early retinal development with human embryonic and induced pluripotent stem cells. *Proc Natl Acad Sci U S A,* 106**,** 16698-703.

MOLDAY, R. S. & MORITZ, O. L. 2015. Photoreceptors at a glance. *Journal of Cell Science,* 128**,** 4039-4045.

MOOSAJEE, M., TULLOCH, M., BARON, R. A., GREGORY-EVANS, C. Y., PEREIRA-LEAL, J. B. & SEABRA, M. C. 2009. Single choroideremia gene in nonmammalian vertebrates explains early embryonic lethality of the zebrafish model of choroideremia. *Invest Ophthalmol Vis Sci,* 50**,** 3009-16.

MUTHIAH, M. N., KALITZEOS, A., OPRYCH, K., SINGH, N., GEORGIOU, M., WRIGHT, G. A., ROBSON, A. G., ARNO, G., KHAN, K. & MICHAELIDES, M. 2021. Novel disease-causing variant in RDH12 presenting with autosomal dominant retinitis pigmentosa. *Br J Ophthalmol*.

NAKAGAMI, Y. 2016. Nrf2 Is an Attractive Therapeutic Target for Retinal Diseases. *Oxid Med Cell Longev,* 2016**,** 7469326.

NAKANO, T., ANDO, S., TAKATA, N., KAWADA, M., MUGURUMA, K., SEKIGUCHI, K., SAITO, K., YONEMURA, S., EIRAKU, M. & SASAI, Y. 2012. Self-formation of optic cups and storable stratified neural retina from human ESCs. *Cell Stem Cell,* 10**,** 771-785.

NANDAKUMAR, N., BUZNEY, S. & WEITER, J. J. 2012. Lipofuscin and the Principles of Fundus Autofluorescence: A Review. *Seminars in Ophthalmology,* 27**,** 197-201.

NGUYEN, V. T., FUSE, Y., TAMAOKI, J., AKIYAMA, S.-I., MURATANI, M., TAMARU, Y. & KOBAYASHI, M. 2016. Conservation of the Nrf2-Mediated Gene Regulation of Proteasome Subunits and Glucose Metabolism in Zebrafish. *Oxidative Medicine and Cellular Longevity,* 2016**,** 5720574.

OZCAN, U., YILMAZ, E., OZCAN, L., FURUHASHI, M., VAILLANCOURT, E., SMITH, R. O., GÖRGÜN, C. Z. & HOTAMISLIGIL, G. S. 2006. Chemical chaperones reduce ER stress and restore glucose homeostasis in a mouse model of type 2 diabetes. *Science,* 313**,** 1137-40.

PARFITT, D. A., LANE, A., RAMSDEN, C. M., CARR, A. J., MUNRO, P. M., JOVANOVIC, K., SCHWARZ, N., KANUGA, N., MUTHIAH, M. N., HULL, S., GALLO, J. M., DA CRUZ, L., MOORE, A. T., HARDCASTLE, A. J., COFFEY, P. J. & CHEETHAM, M. E. 2016. Identification and Correction of Mechanisms Underlying Inherited Blindness in Human iPSC-Derived Optic Cups. *Cell Stem Cell,* 18**,** 769-81.

PARIDAENS, A., RAEVENS, S., DEVISSCHER, L., BOGAERTS, E., VERHELST, X., HOORENS, A., VAN VLIERBERGHE, H., VAN GRUNSVEN, L. A., GEERTS, A. & COLLE, I. 2017. Modulation of the Unfolded Protein Response by Tauroursodeoxycholic Acid Counteracts Apoptotic Cell Death and Fibrosis in a Mouse Model for Secondary Biliary Liver Fibrosis. *Int J Mol Sci,* 18.

PARK, J.-S., SONG, J., PARK, J.-S., LEE, S., LEE, J., PARK, H.-J., KIM, W.-K., YOON, S. & CHUN, H.-S. 2020. 3,4-Dichloroaniline promotes fatty liver in zebrafish larvae. *Molecular & Cellular Toxicology,* 16**,** 159-165.

PARKER, R. O. & CROUCH, R. K. 2010. Retinol dehydrogenases (RDHs) in the visual cycle. *Exp Eye Res,* 91**,** 788-92.

PENUGONDA, S., MARE, S., GOLDSTEIN, G., BANKS, W. A. & ERCAL, N. 2005. Effects of N-acetylcysteine amide (NACA), a novel thiol antioxidant against glutamate-induced cytotoxicity in neuronal cell line PC12. *Brain research,* 1056**,** 132-138.

PERRAULT, I., HANEIN, S., GERBER, S., BARBET, F., DUCROQ, D., DOLLFUS, H., HAMEL, C., DUFIER, J. L., MUNNICH, A., KAPLAN, J. & ROZET, J. M. 2004. Retinal dehydrogenase 12 (RDH12) mutations in leber congenital amaurosis. *Am J Hum Genet,* 75**,** 639-46.

PONTIKOS, N., ARNO, G., JURKUTE, N., SCHIFF, E., BA-ABBAD, R., MALKA, S., GIMENEZ, A., GEORGIOU, M., WRIGHT, G., ARMENGOL, M., KNIGHT, H., KATZ, M., MOOSAJEE, M., YU-WAI-MAN, P., MOORE, A. T., MICHAELIDES, M., WEBSTER, A. R. & MAHROO, O. A. 2020. Genetic Basis of Inherited Retinal Disease in a Molecularly Characterized Cohort of More Than 3000 Families from the United Kingdom. *Ophthalmology*.

PRASAD, S. & GALETTA, S. L. 2011. Anatomy and physiology of the afferent visual system. Elsevier.

RAAB, S., KLINGENSTEIN, M., LIEBAU, S. & LINTA, L. 2014. A Comparative View on Human Somatic Cell Sources for iPSC Generation. *Stem Cells Int,* 2014**,** 768391.

RAGHUPATHY, R. K., ZHANG, X., LIU, F., ALHASANI, R. H., BISWAS, L., AKHTAR, S., PAN, L., MOENS, C. B., LI, W., LIU, M., KENNEDY, B. N. & SHU, X. 2017. Rpgrip1 is required for rod outer segment development and ciliary protein trafficking in zebrafish. *Sci Rep,* 7**,** 16881.

RAHMAN, K. 2007. Studies on free radicals, antioxidants, and co-factors. *Clin Interv Aging,* 2**,** 219-36.
RAO, M. S. & MALIK, N. 2012. Assessing iPSC reprogramming methods for their suitability in translational medicine. *J Cell Biochem,* 113**,** 3061-8.
REICHMAN, S., TERRAY, A., SLEMBROUCK, A., NANTEAU, C., ORIEUX, G., HABELER, W., NANDROT, E. F., SAHEL, J. A., MONVILLE, C. & GOUREAU, O. 2014. From confluent human iPS cells to self-forming neural retina and retinal pigmented epithelium. *Proc Natl Acad Sci U S A,* 111**,** 8518-23.
RICHARDSON, R., TRACEY-WHITE, D., WEBSTER, A. & MOOSAJEE, M. 2017. The zebrafish eye-a paradigm for investigating human ocular genetics. *Eye (Lond),* 31**,** 68-86.
SAHU, B. & MAEDA, A. 2016. Retinol Dehydrogenases Regulate Vitamin A Metabolism for Visual Function. *Nutrients,* 8.
SANJUAN, M. A., DILLON, C. P., TAIT, S. W., MOSHIACH, S., DORSEY, F., CONNELL, S., KOMATSU, M., TANAKA, K., CLEVELAND, J. L., WITHOFF, S. & GREEN, D. R. 2007. Toll-like receptor signalling in macrophages links the autophagy pathway to phagocytosis. *Nature,* 450**,** 1253-7.
SCHEININ, I., SIE, D., BENGTSSON, H., VAN DE WIEL, M. A., OLSHEN, A. B., VAN THUIJL, H. F., VAN ESSEN, H. F., EIJK, P. P., RUSTENBURG, F., MEIJER, G. A., REIJNEVELD, J. C., WESSELING, P., PINKEL, D., ALBERTSON, D. G. & YLSTRA, B. 2014. DNA copy number analysis of fresh and formalin-fixed specimens by shallow whole-genome sequencing with identification and exclusion of problematic regions in the genome assembly. *Genome Res,* 24**,** 2022-32.
SCHIMEL, A. M., ABRAHAM, L., COX, D., SENE, A., KRAUS, C., DACE, D. S., ERCAL, N. & APTE, R. S. 2011. N-Acetylcysteine Amide (NACA) Prevents Retinal Degeneration by Up-Regulating Reduced Glutathione Production and Reversing Lipid Peroxidation. 178**,** 2032-2043.
SCHWARZ, J. M., COOPER, D. N., SCHUELKE, M. & SEELOW, D. 2014. MutationTaster2: mutation prediction for the deep-sequencing age. *Nat Methods,* 11**,** 361-2.
SERTORI, R., TRENGOVE, M., BASHEER, F., WARD, A. C. & LIONGUE, C. 2016. Genome editing in zebrafish: a practical overview. *Brief Funct Genomics,* 15**,** 322-30.
SHACHAM, T., SHARMA, N. & LEDERKREMER, G. Z. 2019. Protein Misfolding and ER Stress in Huntington's Disease. *Frontiers in Molecular Biosciences,* 6.
SHARMA, T. P., WILEY, L. A., WHITMORE, S. S., ANFINSON, K. R., CRANSTON, C. M., OPPEDAL, D. J., DAGGETT, H. T., MULLINS, R. F., TUCKER, B. A. & STONE, E. M. 2017. Patient-specific induced pluripotent stem cells to evaluate the pathophysiology of TRNT1-associated Retinitis pigmentosa. *Stem Cell Research,* 21**,** 58-70.
SHI, R., HUANG, C. C., ARONSTAM, R. S., ERCAL, N., MARTIN, A. & HUANG, Y. W. 2009. N-acetylcysteine amide decreases oxidative stress but not cell death induced by doxorubicin in H9c2 cardiomyocytes. *BMC Pharmacol,* 9**,** 7.
SODI, A., CAPUTO, R., PASSERINI, I., BACCI, G. M. & MENCHINI, U. 2010. Novel RDH12 sequence variations in Leber congenital amaurosis. *J aapos,* 14**,** 349-51.
SONG, J.-Y., FAN, B., CHE, L., PAN, Y.-R., ZHANG, S.-M., WANG, Y., BUNIK, V. & LI, G.-Y. 2020. Suppressing endoplasmic reticulum stress-related autophagy attenuates retinal light injury. *Aging,* 12**,** 16579-16596.
SPARROW, J. R., GREGORY-ROBERTS, E., YAMAMOTO, K., BLONSKA, A., GHOSH, S. K., UEDA, K. & ZHOU, J. 2012. The bisretinoids of retinal pigment epithelium. *Prog Retin Eye Res,* 31**,** 121-35.
SPARROW, J. R., HICKS, D. & HAMEL, C. P. 2010. The retinal pigment epithelium in health and disease. *Curr Mol Med,* 10**,** 802-23.
STRAUSS, O. 2005. The Retinal Pigment Epithelium in Visual Function. *Physiological Reviews,* 85**,** 845-881.

SUN, W., GERTH, C., MAEDA, A., LODOWSKI, D. T., VAN DER KRAAK, L., SAPERSTEIN, D. A., HEON, E. & PALCZEWSKI, K. 2007. Novel RDH12 mutations associated with Leber congenital amaurosis and cone-rod dystrophy: biochemical and clinical evaluations. *Vision Res,* 47**,** 2055-66.

SUNITHA, K., HEMSHEKHAR, M., THUSHARA, R. M., SANTHOSH, M. S., YARISWAMY, M., KEMPARAJU, K. & GIRISH, K. S. 2013. N-Acetylcysteine amide: a derivative to fulfill the promises of N-Acetylcysteine. *Free Radical Research,* 47**,** 357-367.

TAKAHASHI, K., TANABE, K., OHNUKI, M., NARITA, M., ICHISAKA, T., TOMODA, K. & YAMANAKA, S. 2007. Induction of pluripotent stem cells from adult human fibroblasts by defined factors. *Cell,* 131**,** 861-72.

TAKAHASHI, K. & YAMANAKA, S. 2006. Induction of pluripotent stem cells from mouse embryonic and adult fibroblast cultures by defined factors. *Cell,* 126**,** 663-76.

TAVEAU, N., CUBIZOLLE, A., GUILLOU, L., PINQUIER, N., MOINE, E., CIA, D., KALATZIS, V., VERCAUTEREN, J., DURAND, T., CRAUSTE, C. & BRABET, P. 2020. Preclinical pharmacology of a lipophenol in a mouse model of light-induced retinopathy. *Exp Mol Med,* 52**,** 1090-1101.

THOMPSON, D. A., JANECKE, A. R., LANGE, J., FEATHERS, K. L., HUBNER, C. A., MCHENRY, C. L., STOCKTON, D. W., RAMMESMAYER, G., LUPSKI, J. R., ANTINOLO, G., AYUSO, C., BAIGET, M., GOURAS, P., HECKENLIVELY, J. R., DEN HOLLANDER, A., JACOBSON, S. G., LEWIS, R. A., SIEVING, P. A., WISSINGER, B., YZER, S., ZRENNER, E., UTERMANN, G. & GAL, A. 2005. Retinal degeneration associated with RDH12 mutations results from decreased 11-cis retinal synthesis due to disruption of the visual cycle. *Hum Mol Genet,* 14**,** 3865-75.

TOMS, M., BURGOYNE, T., TRACEY-WHITE, D., RICHARDSON, R., DUBIS, A. M., WEBSTER, A. R., FUTTER, C. & MOOSAJEE, M. 2019. Phagosomal and mitochondrial alterations in RPE may contribute to KCNJ13 retinopathy. *Sci Rep,* 9**,** 3793.

TOMS, M., DUBIS, A. M., DE VRIEZE, E., TRACEY-WHITE, D., MITSIOS, A., HAYES, M., BROEKMAN, S., BAXENDALE, S., UTOOMPRURKPORN, N., BAMIOU, D., BITNER-GLINDZICZ, M., WEBSTER, A. R., VAN WIJK, E. & MOOSAJEE, M. 2020. Clinical and preclinical therapeutic outcome metrics for USH2A-related disease. *Human molecular genetics,* 29**,** 1882-1899.

TUNYASUVUNAKOOL, K., ADLER, J., WU, Z., GREEN, T., ZIELINSKI, M., ŽÍDEK, A., BRIDGLAND, A., COWIE, A., MEYER, C., LAYDON, A., VELANKAR, S., KLEYWEGT, G. J., BATEMAN, A., EVANS, R., PRITZEL, A., FIGURNOV, M., RONNEBERGER, O., BATES, R., KOHL, S. A. A., POTAPENKO, A., BALLARD, A. J., ROMERA-PAREDES, B., NIKOLOV, S., JAIN, R., CLANCY, E., REIMAN, D., PETERSEN, S., SENIOR, A. W., KAVUKCUOGLU, K., BIRNEY, E., KOHLI, P., JUMPER, J. & HASSABIS, D. 2021. Highly accurate protein structure prediction for the human proteome. *Nature*.

VACARU, A. M., DI NARZO, A. F., HOWARTH, D. L., TSEDENSODNOM, O., IMRIE, D., CINAROGLU, A., AMIN, S., HAO, K. & SADLER, K. C. 2014. Molecularly defined unfolded protein response subclasses have distinct correlations with fatty liver disease in zebrafish. *Disease models & mechanisms,* 7**,** 823-835.

VALVERDE, D., PEREIRO, I., VALLESPIN, E., AYUSO, C., BORREGO, S. & BAIGET, M. 2009. Complexity of phenotype-genotype correlations in Spanish patients with RDH12 mutations. *Invest Ophthalmol Vis Sci,* 50**,** 1065-8.

VERBAKEL, S. K., VAN HUET, R. A. C., BOON, C. J. F., DEN HOLLANDER, A. I., COLLIN, R. W. J., KLAVER, C. C. W., HOYNG, C. B., ROEPMAN, R. & KLEVERING, B. J. 2018. Non-syndromic retinitis pigmentosa. *Prog Retin Eye Res,* 66**,** 157-186.

VERTREES, R. A., JORDAN, J. M., SOLLEY, T. & GOODWIN, T. J. 2009. Tissue Culture Models. *Basic Concepts of Molecular Pathology,* 2**,** 159-182.

WANG, A. Y. L. & LOH, C. Y. Y. 2019. Episomal Induced Pluripotent Stem Cells: Functional and Potential Therapeutic Applications. *Cell Transplant,* 28**,** 112s-131s.

WANG, J. S. & KEFALOV, V. J. 2011. The cone-specific visual cycle. *Prog Retin Eye Res,* 30**,** 115-28.

WANG, X., WEI, L., WANG, Y., HE, B., KONG, B., ZHU, J., JIN, Y. & FU, Z. 2019. Evaluation of development, locomotor behavior, oxidative stress, immune responses and apoptosis in developing zebrafish (Danio rerio) exposed to TBECH (tetrabromoethylcyclohexane). *Comparative Biochemistry and Physiology Part C: Toxicology & Pharmacology,* 217**,** 106-113.

YU, J., VODYANIK, M. A., SMUGA-OTTO, K., ANTOSIEWICZ-BOURGET, J., FRANE, J. L., TIAN, S., NIE, J., JONSDOTTIR, G. A., RUOTTI, V., STEWART, R., SLUKVIN, II & THOMSON, J. A. 2007. Induced pluripotent stem cell lines derived from human somatic cells. *Science,* 318**,** 1917-20.

ZHANG, J., KISER, P. D., BADIEE, M., PALCZEWSKA, G., DONG, Z., GOLCZAK, M., TOCHTROP, G. P. & PALCZEWSKI, K. 2015. Molecular pharmacodynamics of emixustat in protection against retinal degeneration. *The Journal of clinical investigation,* 125**,** 2781-2794.

ZHANG, L., XIA, Q., ZHOU, Y. & LI, J. 2019. Endoplasmic reticulum stress and autophagy contribute to cadmium-induced cytotoxicity in retinal pigment epithelial cells. *Toxicology Letters,* 311**,** 105-113.

ZHANG, L., ZHOU, Y., XIA, Q., CHEN, Y. & LI, J. 2020. All-trans-retinal induces autophagic cell death via oxidative stress and the endoplasmic reticulum stress pathway in human retinal pigment epithelial cells. *Toxicology Letters,* 322**,** 77-86.

ZHANG, T., BAEHR, W. & FU, Y. 2012. Chemical chaperone TUDCA preserves cone photoreceptors in a mouse model of Leber congenital amaurosis. *Investigative ophthalmology & visual science,* 53**,** 3349-3356.

ZHANG, Z., XIANG, D. & WU, W.-S. 2014. Sodium butyrate facilitates reprogramming by derepressing OCT4 transactivity at the promoter of embryonic stem cell-specific miR-302/367 cluster. *Cellular reprogramming,* 16**,** 130-139.

ZHONG, X., GUTIERREZ, C., XUE, T., HAMPTON, C., VERGARA, M. N., CAO, L. H., PETERS, A., PARK, T. S., ZAMBIDIS, E. T., MEYER, J. S., GAMM, D. M., YAU, K. W. & CANTO-SOLER, M. V. 2014. Generation of three-dimensional retinal tissue with functional photoreceptors from human iPSCs. *Nat Commun,* 5**,** 4047.

ZHU, X., WANG, K., ZHANG, K., ZHOU, F. & ZHU, L. 2016. Induction of oxidative and nitrosative stresses in human retinal pigment epithelial cells by all-trans-retinal. *Exp Cell Res,* 348**,** 87-94.

ZICCARDI, L., CORDEDDU, V., GADDINI, L., MATTEUCCI, A., PARRAVANO, M., MALCHIODI-ALBEDI, F. & VARANO, M. 2019. Gene Therapy in Retinal Dystrophies. *International journal of molecular sciences,* 20**,** 5722.

ZOU, X., FU, Q., FANG, S., LI, H., GE, Z., YANG, L., XU, M., SUN, Z., LI, H., LI, Y., DONG, F., CHEN, R. & SUI, R. 2018. PHENOTYPIC VARIABILITY OF RECESSIVE RDH12-ASSOCIATED RETINAL DYSTROPHY. *Retina*.